Investigation of Graphene's Properties Engineered from Proximity Effects to Twist Engineering

Chun-Chih Tseng

A dissertation
submitted in partial fulfillment of the
requirements for the degree of

Doctor of Philosophy

University of Washington

2024

Reading Committee:

Matthew Yankowitz, Chair

David Cobden

Jiun-Haw Chu

Program Authorized to Offer Degree:
Physics

University of Washington

Abstract

Investigation of Graphene's Properties Engineered
from Proximity Effects to Twist Engineering

Chun-Chih Tseng

Chair of the Supervisory Committee:
Matthew Yankowitz
Physics

Two-dimensional materials exhibit unique electronic properties that differ significantly from their bulk counterparts due to their reduced dimensionality. By assembling heterostructures of van der Waals (vdW) crystals, it is possible to engineer new properties and device functionalities that are absent in the individual materials. Graphene has been extensively studied and serves as a model system for exploring band structure modifications through various couplings. In graphene-based heterostructures, spin-orbit and exchange couplings can be induced via proximity effects, which can stabilize superconductivity and potentially host a variety of topological states. Beyond proximity-induced couplings, twist engineering—which controls interlayer couplings—has emerged as another promising approach to create novel properties without relying on different materials. For example, two monolayer graphene sheets rotated by a certain angle form a flat band characterized by strong correlations, leading to the emergence of states not observed in pristine graphene, such as unconventional superconductivity, correlated insulators, and orbital magnetism.

This dissertation presents transport studies on three distinct graphene-based structures: graphene-vdW magnets CrX_3 (X=I/Br/Cl), graphene-WTe_2, and non-magic-angle twisted bilayer graphene. These studies examines the effects of various couplings on the electronic properties of graphene and additionally probe the exotic gap nature of WTe_2. In the first part about the graphene-CrX_3 structure, we identify several atypical transport features

resulting from charge transfer due to work function mismatch. Although modulation doping of graphene is observed under a magnetic field due to magnetic order switching, the exchange coupling strength is found to be weak, as evidenced by the non-split Landau levels and the absence of an anomalous Hall effect. In the second part, we investigate the transport properties of graphene-WTe_2 heterostructures and probe the correlated gap behavior of WTe_2 with the influence of an adjacent graphene. Finally, in the study of non-magic-angle twisted bilayer graphene, we report an unexpected anomalous Hall effect at half-filling on both the electron and hole sides in two different devices. The anomalous Hall signal and the possible ground state candidates are carefully examined.

Contents

List of Figures

Acknowledgements

First and foremost, I wish to extend my deepest gratitude to my advisor, Prof. Matthew Yankowitz, whose unwavering inspiration and guidance have shaped my journey over the past five years. I still remember our first meeting on Zoom; your great passion ignited my interest and led me to pivot towards 2D materials research in your lab, a path I had not originally planned when I accepted the offer from UW! Working with Matt has been a truly enjoyable experience. His steadfast support in all facets of my research has been invaluable, particularly as his first graduate student. I am continually amazed by his innovative research ideas and his rigorous approach to our results, which have profoundly influenced my development as an independent researcher. Moreover, Matt is always willing to share his thoughts and explain concepts from the simplest level, an essential skill that I greatly admire and aspire to emulate. I deeply appreciate Matt's enthusiasm, diligence, and kindness. It has been an honor and a privilege to be part of his lab, and I am deeply grateful for the opportunity to learn from and work alongside him.

I would like to thank Prof. David Cobden, Prof. Xiaodong Xu and Prof. Jiun-Haw Chu. It has been truly enjoyable to collaborate closely with these distinguished professors. Each brings a unique perspective to science, yet they all share a keen intuition in physics, which has allowed me to learn immensely during the discussions and presentations with them. I am deeply appreciative of the essential and insightful contributions they have provided throughout our collaboration, as well as their tremendous support

for students' research careers. Additionally, I have greatly benefited from the invaluable discussions with other committee members, including Xiao Di, Daniel Gamelin, and Stephen Sharpe. I am profoundly grateful for their guidance and encouragement.

I thank all people in the Yankowitz lab. It has been a wonderful experience working with all of you, as the Yankowitz lab wouldn't be what it is without your contributions! I was delighted to join the lab with Xuetao Ma and Jaehyun Suh at the beginning of our exploration of vdW materials. Soon after, we have Dacen Waters and Zhiming Zhang join our team, bringing their remarkable expertise. Ellis Thompson, Manish Kumar, Anna Okounkova, Toby Chu, Derek Waleffe, Florie Mesple, and Mitchell Kaiser have all contributed to creating a lively and dynamic environment in the lab. Each of you brings a unique personality and warmth that makes the lab a delightful place to work. I also had the pleasure of working with Dylan Jeff, and Alexander Sanchez on various projects. It is great experience to work with you in the same group.

I would like to thank all the collaborators who have contributed to the work in this dissertation. Without their incredible efforts, this dissertation would not have been possible. I am deeply grateful to Jiun-Haw Chu, Qianni Jiang, Zhong Lin, Chaowei Hu, Jonathan DeStefano for providing the excellent crystals essential to our study. I also thank Xiao Di, Zhong Wang, and Yahui Zhang for their invaluable contributions in providing calculations and theoretical models that helped explain the observed features in our results. Additionally, I appreciate the great experience of working closely with Tiancheng Song, Xuetao Ma, Manish Kumar, and Eric Lester in the separate projects. Their collaboration and help are important in the completion of this dissertation.

I would like to extend my gratitude to everyone I haven't mentioned above. I am delighted to have met Jiayi Zhu, Yinong Zhang, Jiaqi Cai, Dmitry Ovchinnikov, Xi Wang, Yingqi Wang, Zaiyao Fei, Minhao He, Kyle Hwangbo, John Cenker, Yuzhou Zhao, Weijie Li, Heonjoon Park, Jack Barlow from Xu's lab; Paul Nguyen, Elliott Runburg, and Luca Delgado from Cobden's lab; and Zhaoyu Liu, Yue Shi from Chu's lab. Conducting

research with all of you in the basement and on the 3rd floor of the physics building has been far from boring. It has been wonderful to have the opportunity to engage in discussions with each of you, and I have always learned a great from your diverse and unique perspectives.

I would like to thank all my friends outside the realm of research. I have cherished our times together, whether being attracted to photography, enjoying festivals, embarking on trips, or savoring delicious food. My life in Seattle would not have been as joyful without the great moments we shared.

Lastly, I want to express my deepest gratitude my parents. They always shows the constant and strong support to me. Their encouragement has been essential in allowing me to pursue my goals and persevere through this journey.

DEDICATION

To my loving parent

Chapter 1

Introduction

1.1 Two-dimensional materials

Two-dimensional (2D) materials, known for their atomic-scale thickness, have emerged as a new class of materials with unique and remarkable properties. Why 2D materials are so intriguing? The main reason is likely related its reduced dimensionality, which usually leads to distinct electronic properties compared to their bulk counterparts. Moreover, due to the extremely thin atomic feature, the materials properties are easily manipulated by various tuning knobs. However, realization of single layer of materials has been proven extremely difficult until the discovery of van der Waals (vdW) materials, which are formed by layers of covalently bonded atoms that are weakly held together by vdW forces. The groundbreaking experiments by Andre Geim and Konstantin Novoselov in 2004 [1] led to the first isolation of graphene. Graphene is the simplest 2D materials - single layer of carbon atoms connected in a honeycomb lattice. Despite the simple crystal structure, it exhibits unprecedented materials properties like the remarkable mechanical [2], thermal [3] and electrical properties [4]. Especially, the unique Dirac cone of graphene, which is most intriguing to researchers in the condensed matter physics field, is able to host exotic phenomena [5, 6, 7].

The success with graphene motivated researchers to explore more 2D material candidates, where new physics or exceptional performance could be discovered. Boron nitride (BN) [8] is a well known 2D insulator and its chemically inert nature makes it an ideal substrate or protection layer to facilitate the material properties for arbitrary 2D materials. Transition metal dichalcogenides (TMDs) are semiconducting [9, 10] with the strong spin-orbit coupling (SOC), providing a great platform to study the excitonic physics and spin- and valley-dependent properties [11]. Moreover, newly discovered 2D materials are able to host exotic electronic phenomena, including the superconductivity [12], the quantum spin Hall effect [13, 14, 15] and ferroelectricity [16]. 2D magnetes as the last missing piece of vdW materials were also discovered in 2017 [17, 18] and they exhibits the versatile tunability of the magnetic order and giant magnetoresistance [19, 20, 21]. The exploration of more 2D materials enable more possibilities of emergent phenomena and device functionality for the future application.

1.2 Van der Waals heterostructures

Creating an arbitrary structure is a long-standing goal to explore various physics and potential device functionality. The weak out-of-plane bonds in vdW materials make this artificial heteterostructure possible by isolating and moving the vdW materials onto another one. People started to develop the a variety of transfer techniques and attempt to vertically assemble different vdW materials to investigate these heterostructures properties. Dry transfer is one of commonly used transfer techniques [22], where a polymer film is employed to pick and assemble 2D material flakes one by one. This technique have several advantages compared to previous film growth methods. First, in principle all vdW materials can flexibly be brought into one heterostructures without considering the lattice mismatch. Second, the whole transfer process is usually kept under relatively low temperature compared to common film growth temperature, which reduce

the possibility of the interaction between each layer. Third, transfer transfer can obtain the atomically sharp interface, which is viewed as a one critical component for a ideal heterostructure. However, people have been questioned the vdW heterostructure for long time, including adsorbates like water and hydrocarbons on the 2D material flake surface to cause the contamination inside the structure. Fortunately, it turns out that contamination can clean itself off the interface.

1.3 Engineering 2D material properties

vdW heterostructures are the promising platform to engineer and manipulate 2D material properties, potentially creating the novel device functionalities and numerous exotic phases.

Field effects

When the target material is surrounded by a insulator, its conductivity can be modulated by applying the electric field through the insulator. This phenomena is called field effect and is one widely applied method to engineer material properties. For this purpose, BN is a remarkably important insulator in the vdW material field. It serves as not only the excellent substrate for the target material [8] but also the great dielectrics for field effects [23]. BN flakes from a few layers to tens of nanometers are typically selected and are capable of providing the carrier density up to 10^{13} $1/\mathrm{cm}^2$. Changing the carrier concentration without introducing chemical impurities could allow for tunable electronic properties and the ability to switch between different electronic phases in one device instead of investigating different samples . Controlling carrier density of monolayer WTe_2 can display not only the different conductivities but also the various phases such as quantum spin Hall insulator [24, 13, 15, 14], superconductor [12, 25] and excitonic insulator [26, 27]. Similarly, tuning the carrier density in tBLG also switch phases from conventional band insulator to correlated insulator and even unconventional

superconductivity [28, 29, 30, 31, 32, 33, 34, 35].

Electric field is another important component induced by field effects. While changing carrier density affects the chemical potential level in the band structure, applying the electric field usually modifies the bands by shifting the whole band or even breaking the system symmetry. A gap can be induced in bilayer graphene by applying the electric field to break the inversion symmetry. A larger density of states (DOS) at the van hove singularities (vHS) in rhombohedral multilayer graphene modulated by the electric field was reported to host various isospin broken states and superconducting states due to the strong correlation [36, 37, 38]. Moreover, electric-driven polarization of carriers is able to tune the magnetic ordering in 2D magnets and switch the topological phases in TMDs as well [39, 40, 41].

Proximity effects

vdW heterostructures not only combines the respective material functionalities but also imprints properties across interfaces where the hybridization of electronic orbitals of adjacent atomically thin layers occurs. This process is called proximity effects and enables the design of artificial structures with unique characteristic. Proximity effects bring unprecedented opportunities for spintronics, particularly for imprinting a SOC or magnetic exchange through the modification of band dispersion and spin texture. Monolayer and multilayer graphene are the model system for proximity effects study due to their non-magnetic nature with the small intrinsic SOC. Therefore, the characteristics of Dirac cone or the original band nature can drastically change by combining graphene with TMDs or magnets if their couplings are sufficient. SOC have distinct types including Ising, Rashba, valley Zeeman, pseudospin inversion asymmetry and so on. Each SOC has its own nature and mechanism to change the graphene's band. On experiment, weak (anti-)localization and charge-spin interconversion (CSI) measurements are commonly employed to investigate graphene–TMD heterostructures, where the proximity-induced SOC reaches millielectronvolts. The induced valley Zeeman SOC in WSe_2/BLG/WSe_2

was demonstrated to create a inverted band structure, potentially related to emerging topological phenomena [42]. Remarkably, Ising or other SOCs were reported to stabilize the superconductivity in bilayer graphene [43, 44], tBLG [45], twisted double bilayer graphene [46].

Similarly, magnetic exchange coupling have two distinct types - FM and AFM couplings, which lead to different energy splitting of the graphene bands at K/K' valley and further induce the magnetism due to the spin imbalance. In the beginning, the devices consisting of graphene and bulk magnets were characterized for the signature of magnetic proximity effects. The anomalous Hall effect (AHE) signal in graphene on insulating ferrimagnet $Y_3Fe_5O_{12}$ (YIG) was observed [47, 48], suggesting the existence of the induced magnetic order. The non-local spin transport measurements were applied to study the band splitting in graphene on other bulk magnets such EuS [49], $BiFeO_3$ [50], where the exchange splitting varies from sub-millielectronvolt to a few millielectronvolts. After the discovery of 2D magnets, people start to make vdW graphene-magnet heterostructure. Similarly, the transport and non-local measurements are investigate the magnetic proximity effects in graphene-$CrBr_3$ [51], graphene-$CrCl_3$ [52], graphene-CrSBr [53], graphene-CrSe [54], graphene-CrOCl [55], where signatures of exchange coupling were detected as well. Beyond graphene, vdW TMD-magnet heterostructures can be probed by optical measurements due to the spin-valley locking and strong light-matter interaction nature of TMDs [11, 56]. The energy splittings were identified and mostly affected by the adjacent 2D magnet layer [57, 58].

Twist

Twist has been proven an unprecedented and effective tuning knob for vdW materials. When two sheets with their own periodic patterns are brought together, the interference pattern is created and it is called moiré pattern. Moire pattern can be realized in vdW materials and induce the superlattice potential in the real space to create a variety of exotic phenomena. In the beginning, people study the moire pattern formed by

graphene and BN. Due to similar lattice constant, the new periodicity is up to 10 nm, which corresponds to the accessible carrier density by electrical doping to fully fill a moire band to study its property. STM [59] and transport measurement [60, 23] show the secondary Dirac point in monolayer graphene aligned with BN, suggesting band structure modification induced by the moire pattern. In addition, Hofstadter butterfly spectrum is observed in this system since the accessible magnetic flux is able to fully fill the moire superlattice with the larger periodicity compared to the periodicity with angstrom scale in original graphene or BN lattices [60, 23].

Due to the intriguing studies on graphene aligned with BN, the twist engineering starts to attract significant attention and be extended to two graphene sheets. It is predicted that two monolayer graphene sheets with several twist angles host flat bands [61], where the strong electron correlation maintain and serves as the important ingredient for the correlated physics. However, the experimental difficulties for realizing the specific twist angles prevent the observation away from the single particle picture. Fortunately, after the improvement of the sample fabrication for the several years, the remarkable and unexpected states were reported in twisted bilayer graphene (tBLG). First, the correlated insulating states and the unconventional superconductivity were revealed in twist bilayer graphene at the magic angle 1.05° with maximized Coulomb interaction [28, 29]. Second, the unique orbital magnetism was detected and can be controlled electrically. The topological Chern states can be also introduced by breaking the symmetries in magic angle tBLG (MA-tBLG) [31, 32, 33, 34, 35, 62, 63, 64].

The enormous success in tBLG motivates more twist studies on other materials beyond graphene. For example, the twisted magnets are able to possess different exchange couplings locally created by different stacking types [65, 66]. The superlattice potential created by moire pattern in twisted TMD materials can trap the exciton more with the longer lifetime [67, 68, 69], which is crucial to study the exciton physics. Similarly, the various correlated insulating states described by the Hubbard model were also

reported in twisted TMDs [70, 71, 72]. A variety of topological states were reported, including fractional [73], double [74] and integer quantum spin Hall effects [73, 74], integer [39, 40, 41] and fractional quantum anomalous Hall effects [40, 41, 75, 76]. Recently, the superconductivity was observed in twisted bilayer WSe_2 [77, 78], which is the only other one twist system beyond graphene exhibiting the superconducting behavior.

Others - Pressure, strain and charge transfer

Hydrostatic pressure serves as a promising tool to manipulate the properties of these vdW materials, as it enhances the interlayer electronic coupling between neighboring crystal layers. Therefore, applying the pressure serves as a promising method to directly enhance the proximity effects. Also, it is shown to not only tune the band gaps in monolayer graphene aligned with BN [79] but also the ability to induce correlated insulating states and superconductivity in non-magic-angle tBLG [30]. Moreover, the exchange coupling types in vdW magnets can be controlled by pressure as well [80, 81].

Strain engineering can be used to lower the intrinsic symmetry of the crystal lattice and as a result modifies the properties of vdW heterostructures. This method has been widely applied to investigate and tune superconductivity, topological phases and nematicity in a variety of bulk quantum materials [82]. Compared with bulk, vdW materials have stronger deformation capacity and larger elastic stain limit, showing the great potentials in strain engineering. People have employed a variety of methods to induce the strain in 2D materials, including the suspension, patterned substrate and piezoelectric substrates [83, 84]. The modifications of electrical, magnetic and phonon properties by strain have been demonstrated.

Charge transfer naturally happen when two materials with the work function mismatch are in contact. Large charge transfer up to 10^{13} $1/cm^2$ was observed in graphene-$RuCl_3$ [85], where charge-transfer plasmon polaritons survive without the external electrical doping. Recently, the concept of charge transfer has been used to make a better electrical contacts to TMD materials to alleviate the Schottky barrier issue [76, 86].

By interfacing TMDs with the specific materials, the lower contact resistances can be achieved and allow for the observation of topological states [76] and superconductivity [77]. Beyond the pure charge transfer, spin-dependent charge transfer can occur by the spin-imbalance from band splitting and further induce novel optical and electrical responses [57, 58].

1.4 The focus of this thesis

In recent years, 2D magnets, 2D topological insulator and twisted 2D structures have been realized and identified as promising platform for fruitful phenomena, such as various topological states, unconventional superconductivity and tunable magnetism. Each systems above has been extensively studied and then the next step is to combine these new systems with each other or old systems to examine the emergent properties. As discussed earlier, due to non-magnetic and weak SOC nature the monolayer graphene will be the ideal model to investigate the modification from the adjacent materials through the proximity effects. In this thesis, I will present my Ph.D. research, focusing on transport studies on graphene-2D magnets, graphene-2D topological insulator and non-magic-angle twisted bilayer graphene (MA-tBLG).

In chapter 2, I'll first present the basics of monolayer graphene. I'll then introduce the modified graphene band and the associated phenomena induced by SOC and magnetic coupling. Finally, I'll give brief introduction of bilayer graphene and an overview of the Bistritzer-MacDonald model and flat bands in tBLG.

In chapter 3 and 4, I'll present the transport studies of graphene-2D magnets and graphene-2D topological insulator heterostructures, respectively. The atypical electrical properties will be reported and the band alignment models are established to explain the anomaly. Finally, I'll present the discussion about the proximity effects and charge transfer in these heterostructures.

In chapter 5, I'll present the transport studies of non-magic-angle tBLG. The unexpected AHE at half filling is reported. I'll discuss the AHE properties and the potential ground state candidates.

Chapter 2

Basics of graphene-based structures

2.1 Crystal and band structure in monolayer graphene

Graphene is a single sheet of carbon atoms arranged in a 2D honeycomb lattice. This honeycomb lattice includes two inequivalent triangular sublattices, often referred to as sublattice A and sublattice B in Figure 2.1a. The lattice constant is approximately 2.46 Å. It is convenient to choose the Bravais lattice to have primitive lattice vectors a_1, a_2 given as shown by Each carbon atom has four valences electrons of which three form sp^2 bonds with its neighboring carbon atoms, creating a stable and planar structure. The remaining unpaired electron in p_z orbital forms a π-bonding system and move freely in the plane of the graphene sheet, leading to the formation of energy bands. Therefore, the graphene band structure can be described by the single orbital tight binding model, which considers the overlap of atomic orbitals and the hopping of electrons between neighboring atoms. The nearest-neighbor tight-binding Hamiltonian has the simple form can be written as

$$H = -t \sum_{\langle i,j \rangle} \left(a_i^\dagger b_j + b_j^\dagger a_i \right) \tag{2.1}$$

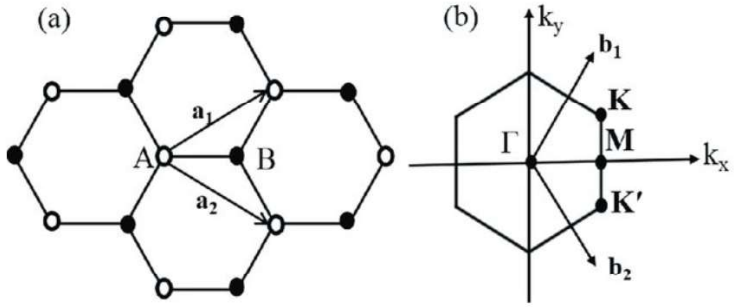

Figure 2.1: **Schematic of graphene lattice structure and the reciprocal lattice.** **a**, Monolayer graphene consisting of carbon atoms in a honeycomb structure with a lattice constant of 2.46 Å. The A and B sublattice are represented by white and black circles respectively. a_1 and a_2 are the primitive unit vectors. **b**, Graphene reciprocal lattice. a_1 and a_2 are the reciprocal lattice vectors and the first Brillouin zone is enclosed by black lines with the K and K' points. (reproduced from [87])

Here, t is the hopping parameter, $a_i^\dagger$ and $b_j^\dagger$ are the creation operators for electrons on sublattices A and B, respectively, and $\langle i,j\rangle$ denotes summation over nearest neighbors. To derive the energy dispersion relation, we can write the wavefunction in terms of Bloch states

$$\psi(\mathbf{r}) = \sum_{\mathbf{R}_A} e^{i\mathbf{k}\cdot\mathbf{R}_A}\phi_A(\mathbf{r}-\mathbf{R}_A) + \sum_{\mathbf{R}_B} e^{i\mathbf{k}\cdot\mathbf{R}_B}\phi_B(\mathbf{r}-\mathbf{R}_B) \tag{2.2}$$

where $\mathbf{R}_A$ and $\mathbf{R}_B$ are the position vectors of the atoms in sublattices A and B, respectively, and ϕ_A and ϕ_B are the atomic orbitals. Then the ultimate goal is to solve the Hamiltonian matrix for the system which is

$$H\psi = E\psi \tag{2.3}$$

Considering the nearest-neighbor interactions, the Hamiltonian matrix for graphene can be written as:

$$H = \begin{pmatrix} 0 & -tf(\mathbf{k}) \\ -tf^*(\mathbf{k}) & 0 \end{pmatrix} \tag{2.4}$$

where $f(\mathbf{k})$ is a function that describes the interaction between nearest neighbors and is given by:

$$f(\mathbf{k}) = \sum_{j=1}^{3} e^{i\mathbf{k}\cdot\delta_j} \tag{2.5}$$

Here, δ_j are the vectors connecting a given atom to its three nearest neighbors. For graphene, these vectors are:

$$\delta_1 = \frac{a}{2}(1, \sqrt{3}), \quad \delta_2 = \frac{a}{2}(1, -\sqrt{3}), \quad \delta_3 = a(-1, 0) \tag{2.6}$$

To find the energy eigenvalues, we solve the determinant of $H - EI$ and it gives

$$E^2 = t^2|f(\mathbf{k})|^2 \tag{2.7}$$

The absolute value of $f(\mathbf{k})$ is:

$$|f(\mathbf{k})|^2 = 1 + 4\cos\left(\frac{k_x a}{2}\right)\cos\left(\frac{\sqrt{3}k_y a}{2}\right) + 4\cos^2\left(\frac{\sqrt{3}k_y a}{2}\right) \tag{2.8}$$

Thus, the energy dispersion relation is

$$E(\mathbf{k}) = \pm t\sqrt{1 + 4\cos\left(\frac{k_x a}{2}\right)\cos\left(\frac{\sqrt{3}k_y a}{2}\right) + 4\cos^2\left(\frac{\sqrt{3}k_y a}{2}\right)} \tag{2.9}$$

Figure 2.2 shows the band calculation using the equation (2.9). We can observe the conduction and valence bands touch at the corners of the first Brillouin zone, K and K points (shown in Fig. 2.1b)

$$K = \frac{4\pi}{3a}(1, 0), \quad K' = \frac{4\pi}{3a}(-1, 0) \tag{2.10}$$

Near these points, the energy dispersion can be approximated as a linear function of crystal momentum, resembling the dispersion relation of relativistic particles described by the Dirac equation

$$E(\mathbf{k}) \approx \hbar v_F |\mathbf{k}| \tag{2.11}$$

Here, v_F is the Fermi velocity, approximately 10^6 m/s for graphene. This linear dispersion is a hallmark of graphene's electronic properties, giving rise to massless Dirac fermions that behave as if they have no effective mass. Due to this unique feature, graphene is able exhibit high electron mobility and other exotic physics including the unconventional quantum Hall effect and Klein tunneling [5, 6, 7].

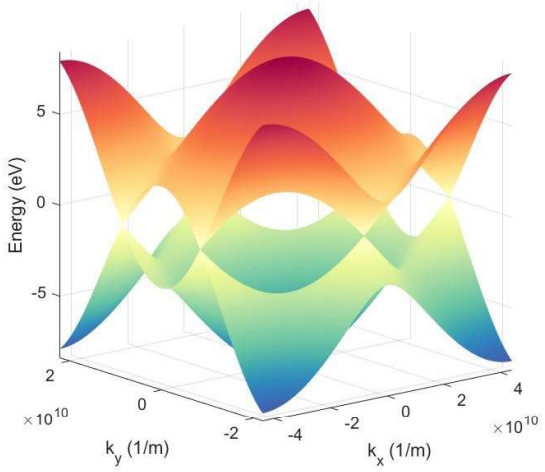

Figure 2.2: **Monolayer graphene band structure.** The graphene band structure calculated by the tight-binding model. The conduction and valence bands touch at the K and K' points. In the low-energy regime, the bands disperse linearly.

2.2 Introduction of the spin-orbit coupling to graphene

Modification of the graphene band by the spin-orbit interaction

The band structure of a pristine graphene can be modified when more couplings

are introduced. In the beginning, people start to investigate band modification and topological phase transition in graphene induced by SOC. The Hamiltonian is written as

$$H = H_{\text{orb}} + H_{\text{soc}} \tag{2.12}$$

where it includes orbital and SOC terms. The orbital part describes gapped Dirac states and is written as

$$H_{\text{orb}} = \hbar v_F(\kappa\sigma_x k_x + \sigma_y k_y) + \Delta\sigma_z \tag{2.13}$$

where v_F is the Fermi velocity , Δ is the staggered potential, σ are the pseudospin Pauli matrices acting on the sublattice A and B, and k_x and k_y are the electron wave vector measured from K (K'); parameter $\kappa = 1$ (-1) for K (K'). Basically, the first term describes low-energy graphene Hamiltonian and the second term describes the gap opening when psuodospin symmtery is broken.

The SOC terms sometimes can be very complicated, including many distinct types originating from different mechanism [88]. For example, the intrinsic SOC $H_I = \lambda_I \tau_z \sigma_z s_z$ is parameterized by λ_I with s the spin Pauli matrices, which exists in a pristine graphene. The valley Zeeman SOC is expressed as $H_{VZ} = \lambda_{VZ}\tau_0 s_z$, where strength λ_{VZ} is pronounced when graphene is interfaced with materials with strong SOC. The Rashba SOC $H_R = \lambda_R(\tau\sigma_x s_y - \sigma_y s_x)$ shows up when space-inversion symmetry breaks by an electric field or the substrate effect. The pseudospin inversion asymmetry (PIA) SOC is $H_{PIA} = \alpha(\lambda_{PIA}\sigma_z + \Delta_{PIA})(k_y s_y - k_x s_x)$, where a is the graphene lattice constant, $\lambda_{PIA} = (\lambda_{PIA,A} + \lambda_{PIA,B})/2$ and $\Delta_{PIA} = (\lambda_{PIA,A} - \lambda_{PIA,B})/2$ with $\lambda_{PIA,A(B)}$ denoting the distinct SOC strength in the graphene sublattice A and B.

By understanding the nature of different SOC, numerous studies aim to examine the graphene band structure when SOC terms are introduced by TMD materials. Each TMD materials is able to offer the different SOC strength, but they can potentially give rise to the band splitting and the gap opening up to a few meV around the Dirac point shown in

Figure 2.3 [89]. This band splitting could be utilized for spin filtering, spin manipulation and efficient charge-to-spin interconversion functionalities. Beyond the splitting, SOC allows to create the inverted band to potentially host nontrivial topological states [90, 42] and is also reported to stabilize the superconductivity [43, 44, 45, 46] in graphene-based structures.

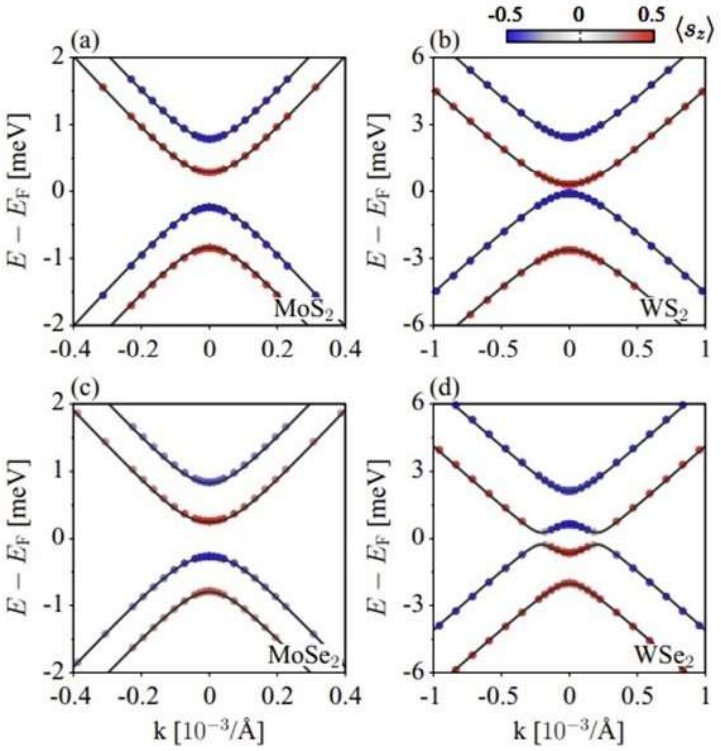

Figure 2.3: **Graphene band structure modified by spin-orbit couplings.** The calculated graphene band structure in graphene in contact with different TMD materials, including MoS_2, WS_2, $MoSe_2$, WSe_2, which introduce different SOC strength into graphene. In the calculation, the graphene band can split and open a gap in the presence of SOC. The band can even go inverted in graphene with WSe_2 to potentially host the topological phenomena. (reproduced from [89])

Weak anti-localization, charge-to-spin interconverion and spin relaxation

The proximity-induced SOC from the TMD layer leads to the suppression of backscattering due to destructive interference of electron wave functions, called weak anti-localization (WAL). This manifests as a characteristic increase in conductivity at low

magnetic fields. Experimental signatures of weak (anti-)localization have been found in graphene-WS_2 [91, 92] and graphene-WSe_2 [93, 94, 95]. The extracted SOC strength ranges from $\sim$1 to 10 meV and and nature of SOC remains unclear, implying the variations in the interface properties in different samples. However, the types of the proximity-induced SOC can be established by charge-to-spin interconverion (CSI) and spin relaxation anisotropy experiments.

Generation of a spin current from a charge current can be triggered by SOC via both the spin Hall effect and the Edelstein effect in a graphene-TMD heterostructure. The efficiency of CSI can be quantified by the spin Hall angle, which measures the ratio of the transverse spin current to the longitudinal charge current. The efficient CSI has been confirmed in several graphene-TMD structures, including graphene-WSe_2 [96], graphene-WS_2 [97, 98] and graphene-MoS_2 [99]. The CSI can be controlled upon electrostatic gating and can be tuned to an optimal value at the proper graphene density. By Kubo–Bastin formula, the nature and the strength of SOC can be obtained [97, 100].

Graphene-TMD heterostructures exhibit the anisotropic spin relaxation, where spin relaxation time on the direction of the spin polarization relative to the crystal axes. This feature originates from proximitized Rashba SOC and the valley-Zeeman SOC. When no spin current is absorbed by the TMD, the anisotropy is mainly dominated by the proximity-induced SOC [101, 102]. The relaxation time between out-of-plane and in-plane directions has been examined to investigate the nature of SOC. It has been proposed that the SOC strength can be tuned with the Fermi energy by the electrostatic gating, leading to an energy-dependent anisotropy [103, 104]. This technique has been employed to study graphene-$MoSe_2$, graphene-MoS_2 and graphene-WS_2 [101, 105].

Emerging topological phenomena

Graphene equipped with appropriate SOC is capable of hosting exotic topological phenomena. The quantum spin Hall effect with helical edge states is predicted to emerge in monolayer graphene via the Kane-Mele SOC [90], although the weak intrinsic SOI in

graphene precludes the experimental observation. However, the result motivates more studies on graphene on TMD materials, which offer stronger SOC into graphene to induce topological phases like quantum spin Hall effect and quantum anomalous Hall effect. Experimentally, the inverted bands accompanied with the SOC-driven gap at charge neutrality has been confirmed in bilayer graphene on WSe_2 probed by the compressibility measurement [42]. Despite that the inverted phase is not expected to be a time reversal invariant quantum spin Hall insulator, the high conductivity and anomalous magnetoresistance are consistent with emergence of the helical edge states. Another experimental work reports the quantum spin Hall insulating state with dissipationless in bilayer graphene-WSe_2 verified by the electrical conductance quantization following the Landauer–Büttiker model prediction [106].

Stabilization of superconductivity

The unconventional superconductivity can stabilized by introducing the SOC into graphene-based systems, including Bernal bilayer graphene, tBLG and twisted double bilayer graphene (tDBG). For the crystalline Bernal bilayer graphene, the superconductivity only survives in the presence of in-plane magnetic field [107], while bilayer graphene interfaced with WSe_2 hosts the superconductivity at the zero field with the critical temperature exceeding the Pauli limit [43, 44]. The large in-plane critical fields were reported to suggest the Ising superconductivity where in-plane mirror and time reversal symmetry protects Cooper pairs against the in-plane field. For tBLG-WSe_2 [45] and tDBG-WSe_2 [46], the superconducting phases start to appear at the twist angles where no SC states emerges in the parent twisted structures without WSe_2. Induced spin-orbit interaction can constrain the nature of the phase diagram and acts as an the symmetry-breaking field that further promotes the superconductivity. The nature of the superconductivity in the crystalline and moiré graphene systems remains elusive and calls for more investigation.

2.3 Introduction of the exchange coupling to graphene

Modification of the graphene band by the exchange interaction

The exchange couplings can be induced when graphene is interfaced with a magnet. The Hamiltonian in the such heterostructure can be expressed as

$$H = H_{\text{orb}} + H_{\text{ex}} \tag{2.14}$$

where the orbital term describes the Dirac band with the staggered potential discussed before and the second proximity exchange coupling term describes the exchange couplings, which is denoted by $H_{EX} = \lambda_{EX} s_z + \lambda_{EX}^{\text{AF}} \sigma_z s_z$ parameterized by λ_{EX} (λ_{EX}^{AF}) and emerges when graphene in contact with ferromagnets (antiferromagnets). This exchange coupling term is usually not able to open the gap at the Dirac point in graphene but break the spin degeneracy instead to induce band splitting similar to what SOC terms do, shown in Figure 2.4. Therefore, efficient control of local spin generation and spin modulation has been extensively studied in graphene-magnets heterostructures. In addition, the large induced exchange coupling from are reported in graphene on different magnetic oxides. Nonlinear AHE signal reported in graphene-YIG is possibly related to the induced magnetic order via the exchange coupling by breaking the time-reversal symmetry.

Exchange splitting

Exchange splitting is expected to emerge when graphene is placed onto a magnet. Early first principle calculation predict a λ_{EX} of tens of millielectronvolts in graphene when proximitized by bulk magnets such as EuO or the ferrimagnet (YIG). Experimentally, examining the Zeeman spin Hall effect via the non-local measurement is one of the most common method is investigate the exchange coupling strength. This technique

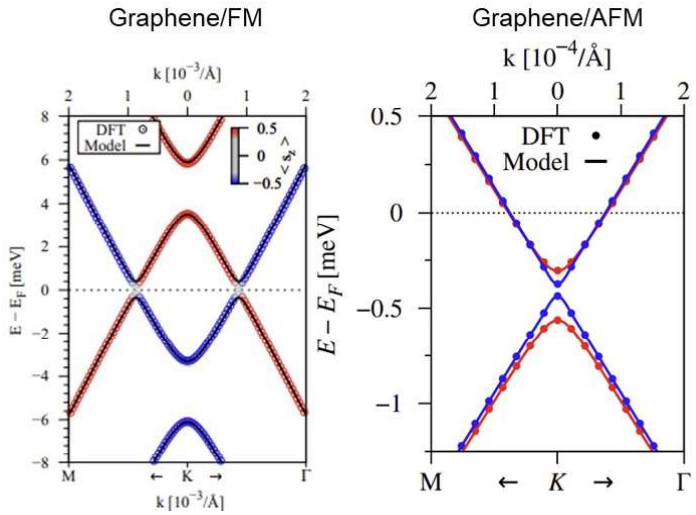

Figure 2.4: **Graphene band structure modified by exchange couplings.** The calculated graphene band structure in graphene in contact with FM and AFM materials which introduce different exchange couplings into graphene. (reproduced from [108, 109], respectivley)

has been applied the examine the λ_{EX} in graphene-EuS [49], graphene-YIG, graphene-NiFe [110], graphene-$CrBr_3$ [51], graphene-$CrCl_3$ [52], graphene-CrSBr [53]. However, the extracted λ_{EX} values on experiment are usually a few meV. The discrepancy about λ_{EX} is likely related to rough interface between graphene and magnets, which is detrimental to the MPE. Despite the smaller λ_{EX}, the graphene-magnet structure has been prove a powerful system to efficiently generate and manipulate the spin polarization for the future applications.

Induced magnetism

Long-range ferromagnetic order can be generated in graphene-magnet heterostructures, manifested by the anomalous Hall signal. The nonlinear AHE signal is reported in graphene-YIG [47, 48], graphene-CrSBr [53] and graphene-EuO [111] by the transport measurement and it can survive up to the room temperature, implying the strong exchange coupling existing in graphene. In addition, the gate tunablity of AHE is demonstrated from the above work and the anomalous Hall conductance can reach $\frac{1}{4}$

of the quantized conductance $\frac{2e^2}{h}$ as the Dirac point approaches from both electron and hole sides [48]. It is pointed out that BN as a encapsulation layer is able to facilitate the exchange coupling by reducing the disorder strength, promoting the opportunity for the quantized conductance. These results motivates the exploration of the topological phases in graphene-magnet heterostructures.

Predicted quantum anomalous Hall effect

Exchange coupling and SOC play different roles in engineering the graphene band structure. Introducing these two couplings to graphene at the same time is predicted to host exotic states. One long-pursing goal is to realize the quantum anomalous Hall effect (QAHE) by providing the exchange coupling and Rashba SOC into graphene through the proximity effects [112, 113, 114, 115]. For the pristine graphene, there are four-fold spin and valley degeneracy close to K(K') points shown in Figure 2.5a. As the exchange coupling is introduced, the spin degeneracy is lifted but the gap remains close (shown in Fig. 2.5b). Once the Rashba SOC is also taken into account, spin-up and spin-down states are mixed around the band crossing points and four bands become completely nondegenerate (shown in Fig. 2.5c-d). Importantly, they together introduce a nontrivial gap at the Dirac point. The bands are characterized to be topological with Chern number C=2, in agreement with the number of chiral edge states from tight-binding calculations. Other DFT calculation also supports that this C=2 QAHE state emerges in graphene-$CrBr_3$ [116] and graphene-CrI_3 [117]. Therefore, people attempt to seek for the experimental observations for quantized σ_{yx} value $\frac{2e^2}{h}$ in graphene/magnet and TMD/graphene/magnet systems.

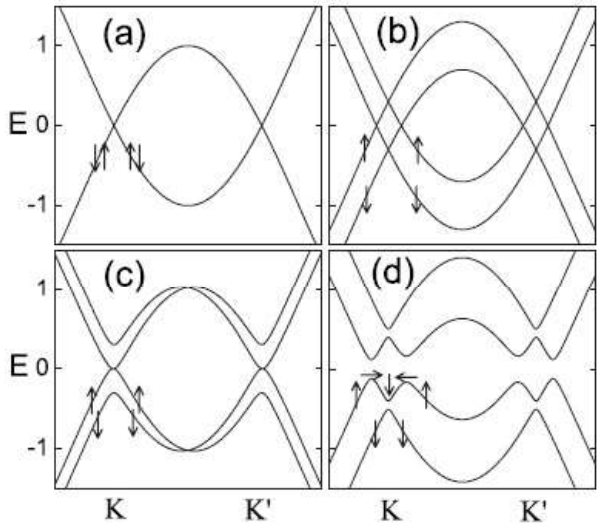

Figure 2.5: **Graphene band structure modified by spin-orbit and exchange couplings.** **a**, The pristine graphene band structure with spin degeneracy. **b**, The graphene band structure in the presence of exchange coupling, which break the spin degeneracy and split the bands by Zeeman effect. **c**, The graphene band structure in the presence of Rashba SOC. which mixes the spin-up and spin-down states around the K(K') points. **d**, The graphene band structure in the presence of Rashba SOC and exchange coupling, which open a gap and make four bands become nondegenerate. (reproduced from [112])

2.4 Band structure in Bernal bilayer graphene

Modification of the graphene band by the fixed interlayer couplings

Before introducing the more complicated tBLG, it's good to review the lattice and band structure of Bernal bilayer graphene first. Bernal bilayer graphene is composed of two monolayer graphene layers in a specific arrangement, shown in Figure 2.6. The two graphene layers are stacked such that one sublattice of the top layer (sublattice A) is positioned directly above a sublattice of the bottom layer (sublattice B). The other sublattice (sublattice B of the top layer and sublattice A of the bottom layer) does not have an atom directly above or below it, creating an AB stacking sequence with a layer separation of 3.35 Å. The unit cell of a bilayer consists of four atoms, two from each layer, which we conventionally label as A1, B1, A2 and B2 corresponding to their layer and sublattice. The electronic properties are primarily governed by the hopping of

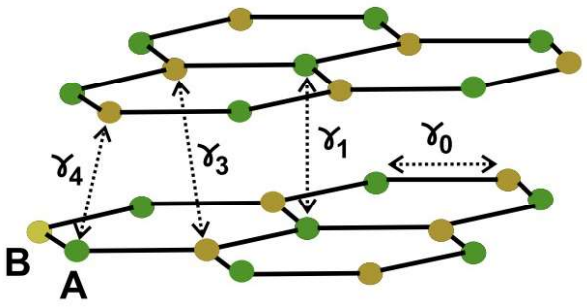

Figure 2.6: **Bernal bilayer graphene lattice structure.** Lattice structure of Bernal stacked bilayer graphene. The A sublattice (green) of the top graphene layer sits vertically onto the B sublattice (yellow) of the bottom layer. The most relevant nearest hopping terms determine the bilayer graphene band structure are labelled. (reproduced from [118])

electrons between the nearest neighbors within the same layer and between the layers, which are intralayer and interlayer couplings, respectively. The total Hamiltonian for Bernal bilayer graphene considering the sum of the intralayer and interlayer hopping

Hamiltonians can be expressed as

$$H_{\text{BLG}} = H_{\text{intra}}^{(1)} + H_{\text{intra}}^{(2)} + H_{\text{inter}} \tag{2.15}$$

where $H_{\text{intra}}^{(1)}$ and $H_{\text{intra}}^{(2)}$ are the intralayer hopping Hamiltonians for the first and second layers, respectively. The intralayer hopping term is similar to that in monolayer graphene discussed earlier and the Hamiltonian for intralayer hopping in a single layer can be written as

$$H_{\text{intra}} = -t \sum_{\langle i,j \rangle} \left(a_i^\dagger b_j + b_j^\dagger a_i \right) \tag{2.16}$$

where t is the hopping parameter (approximately 2.7 eV), $\langle i, j \rangle$ denotes summation over nearest-neighbor pairs, and $a_i^\dagger$ and $b_j^\dagger$ are the creation operators for electrons on sublattices A and B, respectively. For interaction between two layers, the primary interlayer hopping parameter γ_1 describes the hopping between atoms that are directly aligned in the AB stacking configuration (A1 to B2). Additionally, there are weaker interlayer hopping parameters γ_3 and γ_4 that account for the hopping between other atoms not directly aligned. The Hamiltonian for the interlayer hopping can be written as

$$H_{\text{inter}} = \gamma_1 \sum_i \left(a_{1i}^\dagger b_{2i} + b_{2i}^\dagger a_{1i} \right) + \gamma_3 \sum_{\langle i,j \rangle} \left(a_{1i}^\dagger a_{2j} + a_{2j}^\dagger a_{1i} \right) + \gamma_4 \sum_{\langle i,j \rangle} \left(b_{1i}^\dagger b_{2j} + b_{2j}^\dagger b_{1i} \right) \tag{2.17}$$

where $a_{1i}^\dagger$ and $b_{1i}^\dagger$ are the creation operators for sublattices A1 and B1 in the first layer, $a_{2j}^\dagger$ and $b_{2j}^\dagger$ are the creation operators for sublattices A2 and B2 in the second layer, γ_1 (approximately 0.4 eV), γ_3, and γ_4 are the interlayer hopping parameters. We could also consider potential difference Δ for layer asymmetry in the band calculation. Then we

could write down the Hamiltonian in the basis of Bloch states $(\psi_{A1}, \psi_{B1}, \psi_{A2}, \psi_{B2})$ as

$$H(k) = \begin{pmatrix} \frac{\Delta}{2} & \gamma_0 f(k) & 0 & \gamma_4 f(k) \\ \gamma_0 f^*(k) & \frac{\Delta}{2} & \gamma_1 & \gamma_3 f(k) \\ 0 & \gamma_1 & -\frac{\Delta}{2} & \gamma_0 f^*(k) \\ \gamma_4 f^*(k) & \gamma_3 f^*(k) & \gamma_0 f(k) & -\frac{\Delta}{2} \end{pmatrix} \tag{2.18}$$

where the function $f(k)$ represents the in-plane nearest-neighbor interactions and is written as

$$f(k) = e^{ik_x a} + 2e^{-ik_x a/2} \cos\left(\frac{\sqrt{3}}{2} k_y a\right) \tag{2.19}$$

where a is the lattice constant of graphene. For the simplicity, we could ignore γ_3 and γ_4 first since they have less impact on the band compared to t and γ_1. After the solving the eigenvalue problem for the Hamiltonian, the energy around the low-energy regime is expressed as

$$E(\mathbf{q}) = (v_F q)^2 + \frac{\gamma_1^2}{2} + \frac{\Delta^2}{4} \pm \sqrt{(v_F q)^2(\gamma_1^2 + \Delta^2) + \frac{\gamma_1^4}{4}} \tag{2.20}$$

Figure 2.7 summarizes the band structure using the equation (2.20). When $\Delta = 0$, the energy dispersion is approximately parabolic with electron-hole symmetry. There are two bands touching at zero energy and the other two bands are separated by 2t at the q=0. In the presence of Δ by electric field on experiment, the gap is open induced by breaking the layer (inversion) symmetry and the gap size is controlled by the magnitude of Δ. A more realistic band structure can be established by considering higher hopping terms that we ignore early. For example, the γ_3 term is known for causing the trigonal distortion of the bands at low energies.

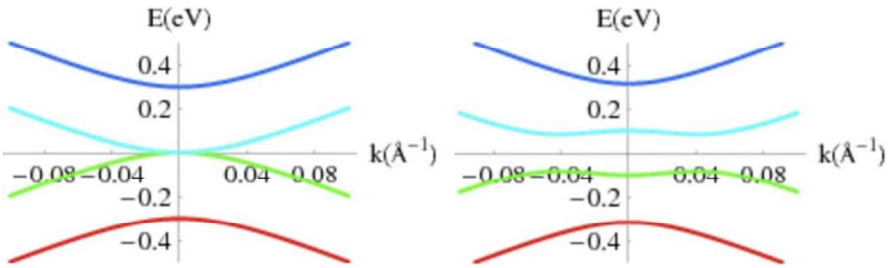

Figure 2.7: **Bernal bilayer graphene electronic band structure.** **a**, The bilayer graphene parabolic band structure in the absence of the external electric field. **b**, The bilayer graphene band structure in the presence of the external electric field, which breaks the inversion symmetry and incduces a gap at the K(K') points. (reproduced from [119])

2.5 Moiré pattern and flat band in twisted bilayer graphene

Modification of the graphene band by the varying interlayer couplings

In the previous sections, we have learned that the electron hopping in the graphene lattice plays a crucial role in the band structure. The intralayer hopping between nearest atoms leads to the linear dispersion in the monolayer graphene, while the interlayer hopping between two layers can contribute to the parabolic dispersion with trigonal warping in the Bernal bilayer graphene. As mentioned earlier, the p_z electrons primarily participate in determining electronic properties in the graphene and different overlapping of p_z orbitals between two layers can create different interlayer couplings. Therefore, rotating two graphene sheets in principle is able to modify the interlayer coupling strength by changing the lateral displacement of p_z orbitals, potentially create a dramatically distinct band compared to the parent band.

For the artificial bilayer graphene with a twist, a moiré pattern emerges with the periodicity of $\lambda = \frac{a}{2\sin(\theta/2)}$, where a is the lattice constant and θ is the twist angle,

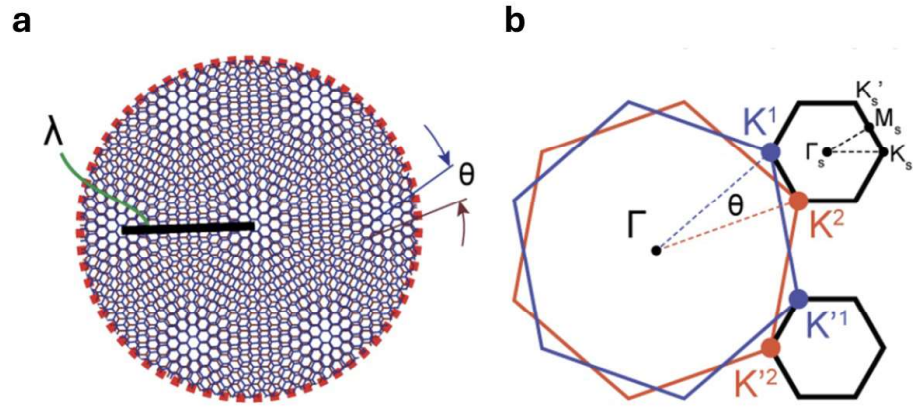

Figure 2.8: **tBLG lattice structure and reciprocal lattice.** **a**, The moiré pattern in twisted bilayer graphene. The new periodicity of the moiré superlattice is $\lambda = a/[2\sin(\theta/2)]$. The schematic shows a tBLG with $\theta = 1.08°$. **b**, tBLG momentum space and the moiré mini Brillouin zone. The mini Brillouin zone is constructed from the difference between the two K (K) wave vectors from the two graphene layers (reproduced from [28]).

shown in Figure 2.8a. This moiré pattern results in a large-scale periodic superlattice that significantly alters the electronic properties. In order to obtain the band structure for tBLG, we again need to solve the eigenvalues problem for the relevant Hamiltonian

$$H_{\text{tBLG}} = H^{(1)}_{\text{intra}} + H^{(2)}_{\text{intra}} + H_{\text{inter}} \tag{2.21}$$

This Hamiltonian H_{tBLG} is pretty similar as H_{BLG}. The first two terms are the intralayer hopping Hamiltonian. The last term is related to the interlayer hopping Hamiltonian, which are sensitively dependent on the twist angle and are therefore different to that in Bernal bilayer graphene in general. We can write Hamiltonian near the Dirac points into a matrix form as

$$H(\mathbf{k}) = \begin{pmatrix} H_1(\mathbf{k}) & T(\mathbf{r}) \\ T^{\dagger}(\mathbf{r}) & H_2(\mathbf{k}) \end{pmatrix} \tag{2.22}$$

The intralayer Hamiltonians $H_1(\mathbf{k})$ and $H_2(\mathbf{k})$ can be easily written as

$$H_1(\mathbf{k}) = \hbar v_F \begin{pmatrix} 0 & k_x - ik_y \\ k_x + ik_y & 0 \end{pmatrix} \tag{2.23}$$

$$H_2(\mathbf{k}) = \hbar v_F \begin{pmatrix} (k_x - \Delta K_x) & 0 \\ 0 & (k_x - \Delta K_x) + i(k_y - \Delta K_y) \end{pmatrix} \tag{2.24}$$

where v_F is the Fermi velocity, and $\Delta\mathbf{K}$ is the shift in the Dirac point due to the twist angle, shown in Fig. 2.8b.

It's relatively difficult to write down the exact form of interlayer hopping. The main reason is related to commensurability of the twist angle. Commensurability refers to the condition where the moiré pattern formed by the two rotated graphene layers has a periodic structure that can be described by a superlattice with a finite unit cell. For certain twist angles, the superlattice vectors of the moiré pattern form a periodic structure. These commensurate angles are typically small and can be described by a rational fraction of the original lattice vectors. At these angles, the resulting superlattice can be described using a finite number of atoms within a unit cell, greatly simplifying theoretical and numerical calculations. However, incommensurate angles result in a moiré pattern that lacks periodicity over long distances. The superlattice is quasi-periodic, making the calculation of electronic properties significantly more complex.

For this section, we focus on commensurate angles and use the continuum model [61] to write down the interlayer coupling $T(\mathbf{r})$ as

$$T(\mathbf{r}) = \sum_{j=0}^{2} T_j e^{i\mathbf{q}_j \cdot \mathbf{r}} \tag{2.25}$$

where $\mathbf{q}_j$ are the moiré reciprocal lattice vectors, and T_j are the coupling matrices:

$$T_0 = w \begin{pmatrix} 1 & 1 \\ 1 & 1 \end{pmatrix}, \quad T_1 = w \begin{pmatrix} e^{i\phi} & 1 \\ 1 & e^{-i\phi} \end{pmatrix}, \quad T_2 = w \begin{pmatrix} e^{-i\phi} & 1 \\ 1 & e^{i\phi} \end{pmatrix} \tag{2.26}$$

where w is the interlayer coupling strength, and ϕ is a phase factor related to the twist angle. $\mathbf{T}_0$ is associated with the direct coupling between the layers with the same reciprocal lattice vectors. $\mathbf{T}_1$ and $\mathbf{T}_2$ are related to the first two indirect coupling between points in the Brillouin zones that are separated by the moiré reciprocal lattice vectors $\mathbf{q}_1$ and $\mathbf{q}_2$ through Umklapp scattering processes. Figure 2.9 summarizes the band structure at the twist angle $\theta = 5°$, $1.05°$ and $0.5°$ with $w = 110$ meV. For the large twist angle, the band structure at low energies is similar to two uncoupled graphene sheets with the slightly renormalized Fermi velocity and the interlayer coupling mainly affects the higher energy band. As the twist angle decreases, the more bands appear within the certain energy range around the Dirac point. The bandwidth for the lowest conduction and valence becomes smaller at the lower angles but behaves non-monotonically with respect to the twist angle. Remarkably, the extremely flat bands with the vanishing Fermi velocity are shown to be discovered at the series of magic angles [61]. The effective Hamiltonians of tBLG at these magic angles are identical to that of monolayer graphene with the renormalized Fermi velocity written as

$$\frac{v_F}{v_{F0}} = \frac{1 - 3\alpha^2}{1 + 6\alpha^2} \tag{2.27}$$

where $\alpha = \frac{\omega}{\hbar v_{F0}|\mathbf{K}|\theta}$ is the dimensionless parameter. The numerator captures the contribution to the velocity. The renormalized Fermi velocity becomes the zero when the numerator is in the process of changing sign. The first and most well-known magic angle is $1.05°$, where large DOS emerging in the flat band with the quenched kinetic energy amplifies the Coulomb interaction. Therefore, twist bilayer graphene becomes a novel

platform for the investigation of strongly correlated physics.

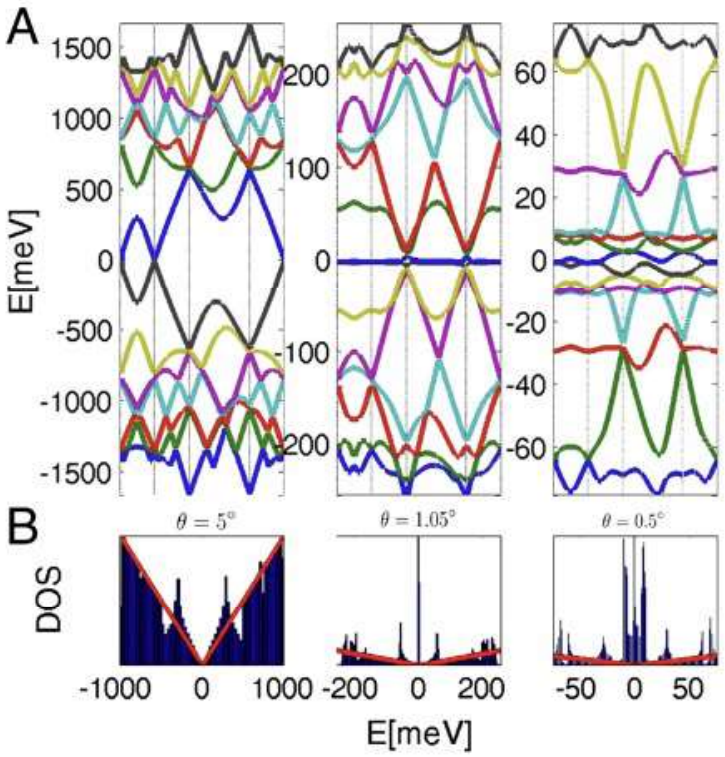

Figure 2.9: **Moiré electronic band structure.** **a**, Calculated energy dispersion closest to the Dirac point plotted along the k-space using $w = 110$ meV with twist angle $\theta = 5°$, 1.05° and 0.5°. **b**, Calculated DOS as a function of the energy with different twist angles. These results demonstrate that flat bands emerge at some magic angles. (reproduced from [61])

Magic-angle tBLG

The initial experimental evidence for strong electron correlation in MA-tBLG is the observation of correlated insulting states and the unconventional superconductivity reported by the MIT group. The big surprise is the similarity of phase diagrams in MA-tBLG and cuprate high-temperature superconductors, implying the two materials are fundamentally related. These results trigger tremendous investigation of MA-tBLG, and more strong correlated and topological states are reported, including orbital magnetism, Chern insulators , symmetry-broken Chern insulators and fractional Chern insulators.

Investigation of isospin symmetry breaking in MA-tBLG is to facilitate our understanding the mechanism for emergent states. For the small twist angles, the isospin degeneracy is four-fold (spin and valley) , same as it in Bernal bilayer graphene [61, 120]. Therefore, the band insulator corresponds to four electron (holes) populating in each moiré unit cell. The initial transport experiments revealed a correlated insulator at half-filling $\nu = -2$ [28, 29] and subsequent work uncovered the these insulating states appearing at each integer filling [30, 31, 32, 33, 34, 35]. However, MA-tBLG acts like Fermi liquid behavior when the ν is not a integer. The observation implies the enhanced electron correlation at the integer filling and the associated cascade of electronic transitions was detected by chemical potential [121], STM [122, 123] and SET [124] measurements.

In addition to strong Coulomb interaction, the topology in the MA-tBLG band is another crucial ingredient to induce various topological states and orbital magnetism. The topology in MA-tBLG originates from the low-energy dispersion of monolayer graphene, which host singularities of Berry curvature around the Dirac points. These Dirac points are protected by C_2T symmetry, where C_2 is the two-fold rotation symmetry and T is the time-reversal symmetry (shown in Figure 2.10a). Breaking either C_2 or T symmetry can gap the Dirac points and generate the flat valley-Chern subbands shown in Fig. 2.10b. Filling a subset of these Chern bands with a nonzero Chern number or Berry curvature can induce the topological states or magnetism [62, 63, 64, 125, 126, 120, 127].

The first observation of magnetism was reported in tBLG aligned with BN [32], where the C_2 symmetry is broken by the influence of a BN substrate. Later, the Chern insulator with C=1 was realized at $\nu = 3$ in tBLG aligned with BN [33], confirmed by quantized R_{xy} and the slope of streda formula. One thing to point out is that ferromagnetic behavior is striking in a pure carbon-based system due to its non-magnetic and weak SOC nature, implying the magnetism is not related to the spin. Therefore, MA-tBLG is likely to exhibit the orbital magnetism from bulk and edge states. This orbital

magnetism is intimately related to electrical switching of magnetic order. In contrast to C_2 symmetry breaking, the time-reversal symmetry can be broken in the presence of the magnetic field. A series of Chern insulating states projecting to the integer fillings is detected by transport [128, 129], STS [130] and SET [131] measurements. By considering the correlation effects, symmetry-broken Chern insulators and fractional Chern insulators can be realized and they are confirmed in the Landau fan diagrams obtained by transport [128, 129] and SET [131] measurements.

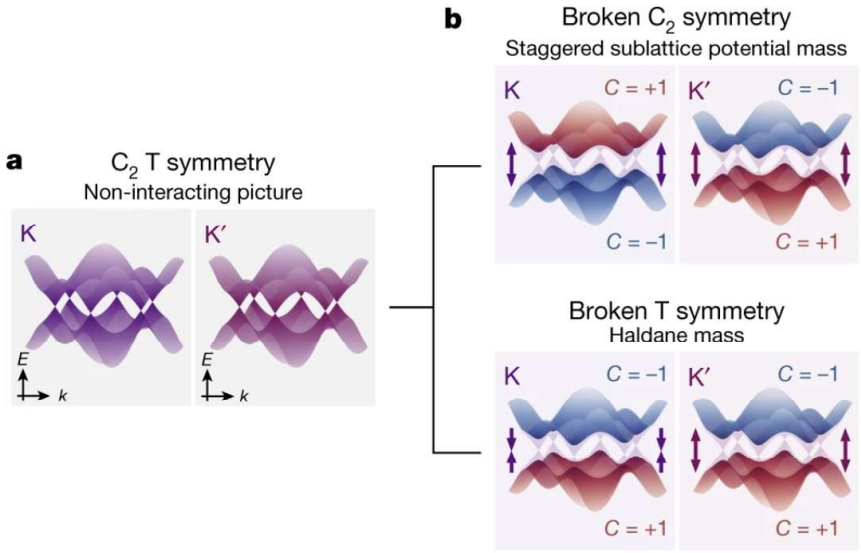

Figure 2.10: **Topological flat band in tBLG. a**, Schematic depiction of a non-interacting model of the band structure of MA-tBLG. Depicted are the eightfold-degenerate Dirac points attributed to two spins, two valleys of the graphene Brillouin zone, and two corners of the moiré Brillouin zone. **b**, Schematic depiction of the two types of broken symmetries that cause the Dirac points to gap. C_2 symmetry is broken by a staggered potential mass. Time-reversal symmetry is broken by an interaction-induced Haldane mass, which opens a mass gap of equal and opposite magnitude in the K and K' valleys. (reproduced from [132])

Chapter 3

Investigation of graphene-2D magnets structures

In the previous chapter, we learn that magnetic proximity effects in graphene can induce intriguing phenomena and topological phases. However, initial studies on graphene-magnet heterostructures involved either growing magnetic films directly on graphene or transferring graphene onto sputtered magnetic films, introducing interdiffusion/interaction, and interface roughness issues, respectively. Consequently, the experimental validation of magnetic proximity effects in graphene on bulk magnets was largely constrained. Fortunately, with the discovery of 2D magnetic materials, there is a renewed opportunity to re-examine proximity effects with clean interfaces in all-vdW-heterostructures. In this chapter, I'll give the brief overview of 2D magnets and investigate the transport properties of graphene in contact to layered magnets CrX_3 (X= I, Br, Cl).

3.1 Overview of 2D magnets

The field of vdW materials began with the groundbreaking isolation of monolayer graphene in 2004. This discovery paved the way for exploring a wide variety of semiconducting, su-

perconducting, and insulating vdW materials. However, a crucial and long-missing member of the 2D material family was the vdW magnet. According to the Mermin–Wagner theorem, spontaneous polarization cannot exist in the isotropic 2D Heisenberg model at finite temperatures [133], leading to the belief that long-range magnetic order could not survive in the 2D limit. For a long time, it was thought impossible to achieve magnetic order in 2D materials. A necessary condition for establishing magnetic order in two dimensions is strong magnetic anisotropy [134], which can open an energy gap in the spin-wave spectrum and suppress thermal fluctuations. This changed when, in 2016, researchers reported stable antiferromagnetic ordering signatures in atomically thin $FePS_3$ using Raman spectroscopy [135]. The following year, in 2017, researchers from the University of Washington and UC Berkeley observed direct spontaneous magnetization in CrI_3 [136] and $Cr_2Ge_2Te_6$ [18] down to the 2D limit using MOKE measurements. These landmark studies have sparked extensive exploration of additional vdW magnets and provided an exciting research platform for understanding low-dimensional magnetism.

Due to their atomically thin nature, 2D magnets exhibit unique magnetic properties that are highly susceptible to changes in thickness, distinguishing them from traditional 3D magnetic materials. For example, $Cr_2Ge_2Te_6$ demonstrates clear ferromagnetic order in layers thicker than two layers, with the T_c increasing monotonically with thickness—from 30 K in a bilayer to 68 K in bulk samples [18]. CrI_3, on the other hand, displays even more striking thickness-dependent magnetism. Odd-layer CrI_3 is ferromagnetic, whereas even-layer CrI_3 shows antiferromagnetic coupling [136]. These observations reveal the unique intralayer ferromagnetic (FM) and interlayer antiferromagnetic (AFM) couplings in CrI_3. Beyond detecting 2D magnetism, considerable efforts have been directed towards manipulating these magnetic properties for future applications. Electrical doping has been shown to control the magnetic coupling strength in CrI_3, even altering the type of magnetic coupling [19, 20]. Additionally, hydrostatic pressure and strain engineering have been employed to tune the magnetic states in CrI_3 [80, 81] and

CrSBr [137], respectively. These studies highlight the intriguing and tunable nature of 2D magnetism, emphasizing the potential for innovative applications that leverage the unique properties of vdW magnets.

The utilization of 2D magnets in vdW heterostructures has led to unprecedented advancements. Initial studies, such as those on magnetic tunnel junctions (MTJs) involving few-layer CrI_3, demonstrated a giant tunneling magnetoresistance that drastically increased with CrI_3 layer thickness, reaching a remarkable 19,000 [138]. This not only underscores the potential of 2D magnets for magnetic information storage but also introduces an alternative technique for studying the magnetic configurations of 2D magnets. Following these pioneering studies, research extended to thicker CrI_3, other chromium trihalides, and additional vdW magnets, further broadening the scope of MTJ applications [139]. Researchers also have employed vdW magnets to induce exchange splitting in adjacent materials. Significant exchange splitting has been reported in systems such as graphene-vdW magnet heterostructures [51, 52, 53]. However, the practical implementation of vdW magnets in conventional device fabrication remains challenging, as these materials are highly susceptible to degradation. The sample conditions and properties often fall short of the ideal standards required for detailed studies of vdW magnet-based heterostructures. Therefore, there is an urgent need to develop advanced fabrication techniques that can accommodate the sensitive nature of vdW magnets. Ensuring sharp and clean interfaces in all-vdW-heterostructures is crucial for accurately examining their relevant properties. The well-studied chromium trihalides are chosen to be the 2D magnets for this study.

3.2 Experimental setup and methods

Chromium trihalides CrX_3 (X=I/Br/Cl)are extremely sensitive materials, so that a conventional device fabrication is not compatible. Therefore we develop an alternative method to circumvent the sensitiveness issue of CrX_3. The basic idea is to keep CrX_3 either under an inert environment or double-encapsulated by BN flakes from degradation during the whole fabrication. Air-stable materials, like graphene and BN, are exfoliated under the ambient, while CrX_3 are exfoliated in the glovebox filled with Ar (both O_2 and H_2O <0.5 ppm). Samples are assembled using a dry-transfer technique with a polycarbonate (PC)/polydimethyl siloxane (PDMS) stamp [22]. In order to protect CrX_3 from degradation, we first shape a flake of monolayer graphene into a Hall bar geometry using a polymer-free anodic oxidation lithography technique with an atomic force microscope tip [140]. The vdW heterostructure consists of a graphene/CrX_3 interface encapsulated between flakes of BN. Additional graphite flakes encapsulate some samples to act as gates. The sample is deposited onto a Si/SiO_2 wafer after assembly by melting the PC film at 180°C. The entire vdW heterostructure assembly is performed inside a glovebox filled with argon. It is then removed from the glovebox, and the PC film is dissolved in chloroform. The CrX_3 crystals are protected from degradation as long as they remain fully encapsulated by BN flakes. We use standard electron beam lithography, CHF_3/O_2 plasma etching, and metal deposition techniques (Cr/Au) in order to electrically contact the graphene Hall bar in regions far from the CrX_3 flake. Fig. 3.2 illustrates the fabrication procedure in detail.

In this study, we study six devices of graphene on various CrX_3 substrates, and one device with a monolayer WSe_2 spacer. Table 3.1 summarizes the details of these devices. Data in the main text is acquired from Device A. Figure 3.1 shows optical micrographs of all seven devices. Device A has a silicon back gate and gold top gate. All other devices have graphite top and bottom gates.

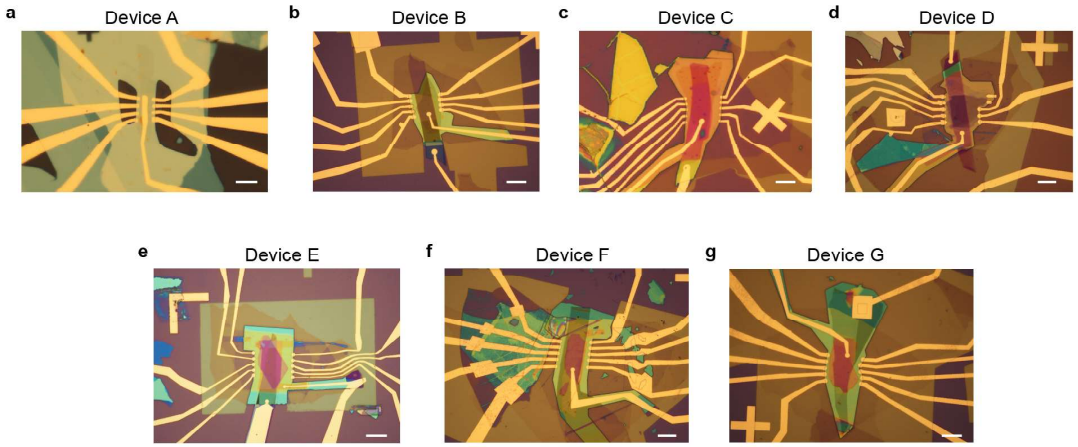

Figure 3.1: **Optical micrographs of the seven devices in this study.** All scale bars are 10 μm.

Device	Material	CrX_3 Thickness
A	CrI_3	3 layers
B	CrI_3	7 layers
C	CrI_3	10 layers
D	WSe_2/CrI_3	1/3 layers
E	$CrBr_3$	28 nm
F	$CrCl_3$	40 nm
G	$CrCl_3$	80 nm

Table 3.1: Summary of the devices reported in our study.

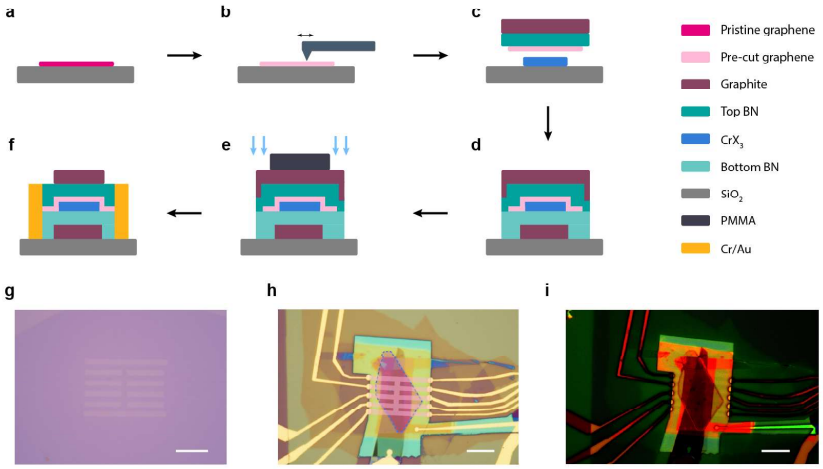

Figure 3.2: **Device fabrication procedure.** **a**, Flakes of monolayer graphene, graphite, BN, and CrX_3 are isolated by mechanical exfoliation. **b**, The graphene is cut into a Hall bar geometry using a polymer-free anodic oxidation lithography technique with an atomic microscope tip. **c**, The vdW layers are assembled using conventional dry transfer techniques with a PC stamp. The entire transfer process is conducted inside an inert gas glovebox (filled with Ar), with oxygen and water levels below 1 ppm. **d**, The vdW heterostructure is deposited onto a clean Si/SiO_2 chip and removed from the glovebox. The CrX_3 is protected from degredation by the encapsulating top and bottom BN crystals. **e**, The device is etched with CHF_3 and O_2 plasma using a protective PMMA mask. The CrX_3 remains completely encapsulated in BN after the etch procedure, however, the arms of the graphene Hall bar are exposed. **f**, Cr/Au is evaporated to form electrical contacts to the graphene Hall bar and the graphite gates. **g-i**, Optical micrographs of a flake of monolayer graphene cut by an AFM tip to form an internal Hall bar geometry (**g**), a representative completed device (Device E) (**h**), and the same device with digital color filtration to make the graphene Hall bar arms visible (**i**). The pink Hall bar overlay in **h** indicates the region of the pre-cut graphene, and blue dashed curve outlines the $CrBr_3$ flake. All scale bars are 10 μm.

3.3 Transport in monolayer graphene with 3L CrI_3

Figure 3.3a shows a schematic of the general device structure we fabricate. Interfaces of graphene and thin CrX_3 are encapsulated with BN and surrounded by top and bottom gates. The CrX_3 crystals we use range from three to tens of layers in thickness, however, the majority of our results do not appear to depend meaningfully on this parameter. In order to avoid degradation of the CrX_3 crystals during device fabrication, we first shape a flake of exfoliated graphene into a Hall bar geometry using a polymer-free anodic oxidation technique with an atomic force microscope tip [140], and then assemble the entire vdW heterostructure in an argon-filled glovebox. We fabricate devices in which the graphene rests atop CrX_3, and vice versa, and see the same behavior in both cases. For clarity, we henceforth refer to the bias on the gate facing the graphene (CrX_3) as V_{gr} (V_{mag}).

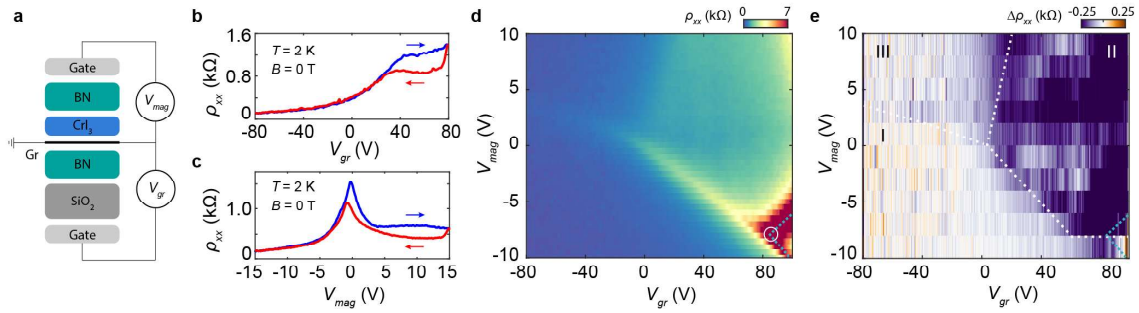

Figure 3.3: **Transport in graphene on CrI_3 at zero magnetic field.** **a**, Schematic of the device structure. Monolayer graphene is interfaced with CrI_3 and encapsulated by BN. The voltage on the gate facing the graphene is V_{gr}, and the voltage on the gate facing the CrI_3 is V_{mag}. **b**, Four-terminal resistivity of a device with trilayer CrI_3 (Device A) as V_{gr} is swept back and forth, with $V_{mag} = 0$. **c**, Resistivity as V_{mag} is swept back and forth with $V_{gr} = 0$. **d**, Map of the device resistivity acquired by sweeping both gates. The trajectory of the Dirac point is denoted by the blue dashed curve, as determined by Hall effect measurements at $B = 4$ T. The white circle denotes the point at which the trajectory of the Dirac point reverses. **e**, Map of the transport hysteresis, $\Delta\rho_{xx}$, acquired by taking the difference between the resistivity upon slowly sweeping V_{gr} forward and backward. The white dashed curve is a guide to the eye, corresponding approximately to resistive peaks and plateaus seen in **d**.

Atypical gate dependence induced by charge transfer

We focus our attention primarily on graphene/CrI_3 heterostructures, from which we can additionally understand the salient properties of graphene/$CrBr_3$ and $CrCl_3$ later. CrI_3 has the lowest electron affinity of the three chromium trihalides, and as a result the modulation doping of the graphene is the smallest. Figure 3.3b (c) shows the resistivity of a graphene on trilayer CrI_3 device (Device A) measured as V_{gr} (V_{mag}) is swept back and forth with the other gate grounded at a temperature of $T = 2$ K. We see a number of features that are uncharacteristic of pristine graphene encapsulated only with BN. First, the transport differs notably depending on which of the two gates is swept. Second, the transport is hysteretic, with the hysteresis most pronounced at positive values of either gate voltage. Although there are kinks or peaks in the resistivity suggestive of a Dirac point, measurements of the corresponding Hall resistance reveal that the graphene is hole-doped over most of the accessible gate voltage range in Fig. 3.4, indicating that these resistive peaks arise from a different mechanism.

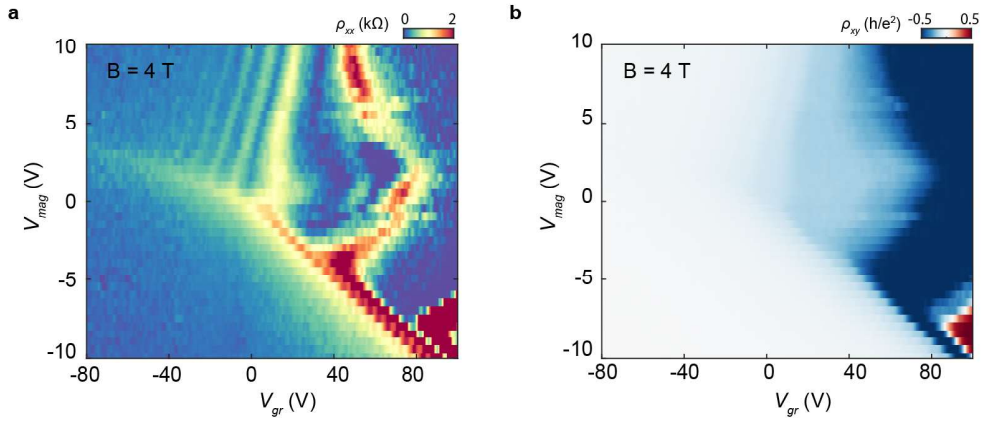

Figure 3.4: **Transport measurements of Device A at $B = 4$ T. a-b**, Maps of ρ_{xx} (**a**) and ρ_{xy} (**b**) acquired by sweeping both gates at $B = 4$ T. The sign of the Hall effect is negative over the entire map except for a small region in the bottom right, indicating that the graphene is hole-doped. The blue dashed curve in Fig. 1d of the main text corresponds to the condition of $\rho_{xy} = 0$ in (**b**).

Figure 3.3d shows a map of the device resistivity acquired by sweeping both of the

gates. The blue dashed curve traces the position of the Dirac point as determined by Hall effect measurements in Fig. 3.4. The Dirac point evolves with the two gate voltages as anticipated from simple electrostatics in the bottom rightmost portion of the map. However, its trajectory abruptly reverses as the bias on V_{mag} is further reduced towards zero (white circle in Fig. 3.3d). The bent trajectory of the Dirac point indicates a nonlinear and nonmonotonic relationship between the gate voltage and graphene charge carrier density, in stark contrast with the behavior of conventional monolayer graphene devices in which the gate capacitance is fixed. We see other transport features atypical of graphene, including an anomalous resistive peak that moves roughly diagonally across the map, as well as an abrupt resistive step separating the top left and right halves of the map. There is also a sharp resistivity increase in the top rightmost corner of the map that indicates the reappearance of the Dirac point. Further, these features are directly associated with the hysteretic graphene transport. Figure 3.3e shows a measurement of $\Delta\rho_{xx}$ acquired by taking the difference between ρ_{xx} measured as V_{gr} is slowly swept back and forth. As a guide to the eye, the white dashed curve denotes the positions of the anomalous resistive peaks we observe in Fig. 3.3d, and separates the map into Regions I, II, and III. The hysteresis is most prominent in Region II of the map, approximately bounded by the anomalous resistive peaks and plateaus.

Atypical transport features in Landau fan diagrams

Transport measurements in a magnetic field, B, help to reveal the origin of these unusual features. Figures 3.5a-b show Landau fan diagrams of the longitudinal, ρ_{xx} (top), and Hall, ρ_{xy} (bottom), resistivities acquired by sweeping V_{gr} from negative to positive bias with fixed values of $V_{mag} = 15$ V and -10 V, respectively. The latter is consistent with typical hole-doped graphene: the Dirac point appears at large positive V_{gr} and is associated with a sign change in ρ_{xy} upon doping, and there is a series of integer quantum Hall (IQH) states that disperse linearly away from the Dirac point. These correspond to filling factors of $\nu = -2, -6, -10, ...$, consistent with the usual

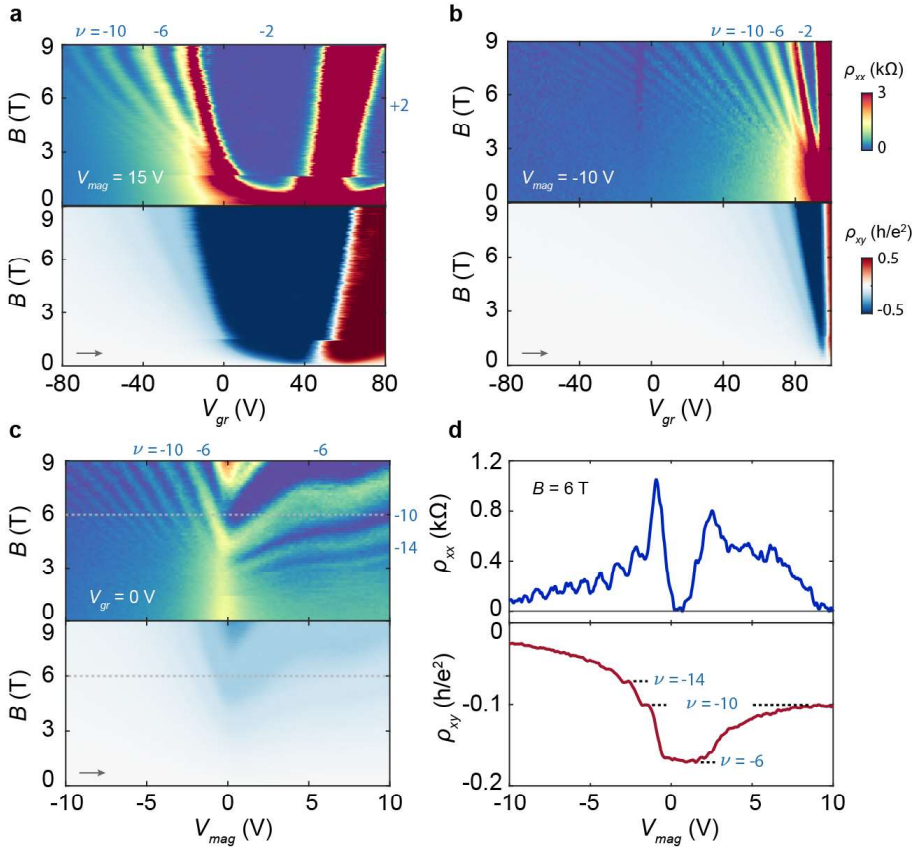

Figure 3.5: **Landau fan diagrams of graphene on CrI_3. a-b**, (top) Longitudinal, ρ_{xx}, and (bottom) Hall, ρ_{xy}, resistivities of Device A acquired by sweeping V_{gr} from negative to positive values with $V_{mag} = 15$ V (**a**) and $V_{mag} = -10$ V (**b**), respectively. **c**, Landau fan diagram acquired by sweeping V_{mag} from negative to positive with $V_{gr} = 0$. **d**, ρ_{xx} (top) and ρ_{xy} (bottom) cuts from **c** acquired at $B = 6$ T.

sequence of states arising from spin- and valley-degenerate monolayer graphene Landau levels. In contrast, at $V_{mag} = 15$ V we see a number of anomalous features in the Landau fan, including the Dirac point drifting with magnetic field, an abrupt resistivity jump at $B = 1.6$ T, extremely wide $\nu = \pm 2$ IQH plateaus, and IQH states at higher filling factors with slightly widened plateaus that move nonlinearly.

Landau fans acquired by sweeping V_{mag} at fixed V_{gr} exhibit even more striking peculiarities. Figure 3.5c shows a representative example, in which the IQH states disperse as expected for $V_{mag} = 0$, but abruptly reverse direction for $V_{mag} = 0$. The latter regime

corresponds to an apparent negative compressibility of the system, in which applying more positive gate voltage results in filling additional hole-type Landau levels, rather than their anticipated depletion. Figure 3.5d shows a representative example of this phenomenon at $B = 6$ T, in which the graphene exhibits two disconnected regimes of doping corresponding to the $\nu = -10$ IQH state.

The IQH states in typical graphene devices fan out linearly from the Dirac point as the magnetic field is raised. Their trajectories are described by the Středa formula [141], $\nu = (h/e)(\partial n/\partial B)$, where h is Planck's constant, e is the charge of the electron, and n is the charge carrier density. Departure from this behavior provides further evidence of the nonlinear relationship between the gate voltage and the charge carrier density in the graphene originating from the charge transfer with the CrI_3, consistent with the bent trajectory of the Dirac point observed in Fig. 3.3d. The wide IQH plateaus and their nonlinear trajectories in the fan diagram indicate that the charges induced by the gate do not accumulate in the graphene but rather fill the CrI_3, since electrons become localized in the insulating CrI_3 and do not contribute to transport. Related effects have been previously observed in graphene on SiC [142, 143] and CrOCl [55]. The coexistence of normal and atypical quantum Hall effects within our device suggests that the modulation doping can be controlled by gating, and under suitable conditions is even suppressed entirely.

Band alignment between graphene and CrI_3

We characterize the full dependence of the charge transfer on gating and magnetic field by measuring ρ_{xx} and ρ_{xy} over the entire accessible range of both gate voltages at a fixed $B = 9$ T (shown in Fig. 3.6a-b). For the purposes of analyzing the behavior, we divide the map into three regions as marked by the white dotted lines (reproduced from Fig. 3.3e). Region I exhibits typical graphene magnetotransport, in which a sequence of hole-doped IQH states disperses diagonally. The negative slope of these features is consistent with the ratio of the geometrical capacitances of the top and bottom gates.

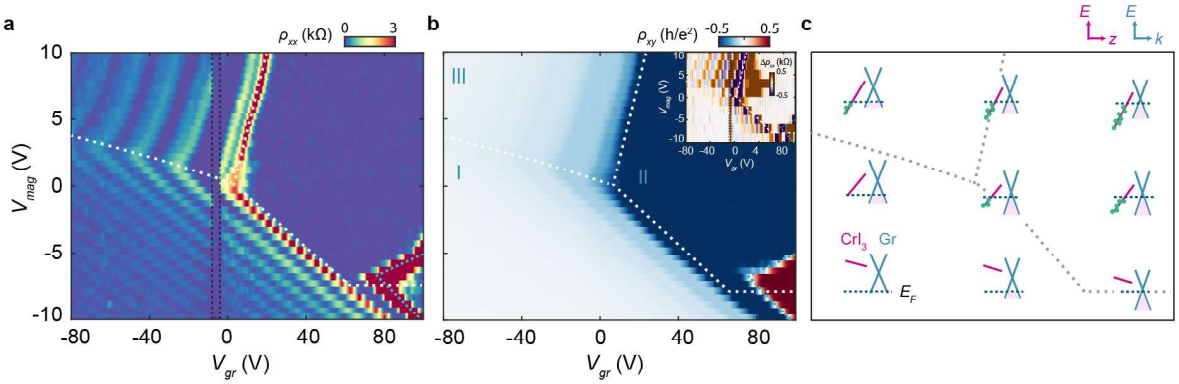

Figure 3.6: **Mapping the charge transfer and band alignment in graphene on CrI_3. a-b**, Maps of ρ_{xx} (**a**) and ρ_{xy} (**b**) acquired by sweeping both gates at $B = 9$ T. The white dotted lines are the same guides to the eye as in Fig. 5.1e, and separate the map into Regions I, II, and III. The $\nu = 0$ state, corresponding to the Dirac point, is determined by the sign change in ρ_{xy} (blue dashed curve). (inset of **b**) Map of the transport hysteresis, $\Delta\rho_{xx}$, acquired at $B = 9$ T. The regions enclosed within the vertical black and gray boxes in **a** and the inset of **b** are contaminated by artifacts owing to insulating behavior at the contacts. **c**, Inferred alignment of the graphene Dirac cone (blue) and the lowest electron-holding states in CrI_3 (red) under different gating conditions, corresponding to the approximate corresponding positions from the maps in **a-b**. Because the CrI_3 is multiple layers thick, gate voltages establish an electric field across the sheet which tilts the bands. The band offset at the interface between the graphene and adjacent CrI_3 layer is a fixed quantity determined by the graphene work function and CrI_3 electron affinity. The dark blue dashed line denotes the Fermi energy, E_F, in the graphene. Filled states in graphene are indicated in pink, and electrons in CrI_3 are denoted schematically by the green dots.

This remains true for the $\nu = 0$ insulating state in the bottom right corner of the map, across which the sign of the Hall effect flips. In contrast, Region II corresponds almost entirely to the $\nu = -2$ IQH state. At the foot of Region II, we observe an abrupt reversal in the trajectory of the $\nu = 0$ state similar to that of the Dirac point at $B = 0$ (shown in Fig. 3.3d). In Region III, the IQH states become nearly insensitive to V_{mag} and develop a positive slope. The inset of Fig. 3.6b shows hysteresis measurements, $\Delta\rho_{xx}$, acquired at $B = 9$ T, analogous to the zero-field map shown in Fig. 3.3e. The hysteresis is primarily confined to Region III; however, we note that this measurement scheme is largely insensitive to hysteresis in Region II owing to the extended $\nu = -2$ plateau. In

combination with the zero-field measurements (shown in Fig. 3.3e), we deduce that the device exhibits hysteresis in both Regions II and III. The hysteresis is therefore directly associated with regions of atypical graphene transport, and does not occur in Region I where the transport is conventional.

The above measurements can all be qualitatively understood by taking into account the gate- and field-dependent charge density in the CrI_3. Figure 3.6c shows a series of cartoon diagrams that depict the electron states and their occupancies in the graphene (blue) and CrI_3 (red) for different combinations of the top and bottom gate voltages. Filled states in graphene below the chemical potential (blue dashed line) are colored pink. The red line represents the lowest-energy electron states in the CrI_3, and corresponds either to the bottom of the conduction band or a band of in-gap defect states; the latter is more likely because the charge mobility is very low. Electrons in the CrI_3 are indicated by the green dots. We assume that the alignment between the graphene Dirac point and the lowest-energy electron band in the neighboring CrI_3 layer is fixed by the combination of the graphene work function and CrI_3 electron affinity. Biasing V_{mag} establishes an electric field across the few-layer CrI_3, shifting the energy of the CrI_3 states either up or down relative to the graphene.

Within Region I, the chemical potential lies beneath the lowest-energy electron states throughout the CrI_3, and as a result they are all unoccupied. The CrI_3 then simply behaves as a dielectric, and changing the bias on either gate capacitively dopes the graphene as usual. In Regions II and III, the bias V_{mag} is such that some electron states in the CrI_3 are below the chemical potential, causing electrons to tunnel into them from the graphene. These electrons become almost entirely localized and contribute negligibly to the conductivity, but are mobile enough in the out-of-plane direction to screen the underlying gate. This results in a greatly altered sensitivity of the graphene doping to changes in V_{mag}. The hysteresis observed in these regions results from an inability of the electrons to reach a true equilibrium due to long timescales in the CrI_3.

As further evidence for this, we observe irreversible changes in the modulation-doping of the graphene in measurements performed days apart (shown in Fig. 3.7), and in a graphene/$CrCl_3$ device doped to a similar regime, the resistance exhibits telegraph noise on a timescale of tens of minutes when both gate voltages are held fixed (shown in Fig. 3.8).

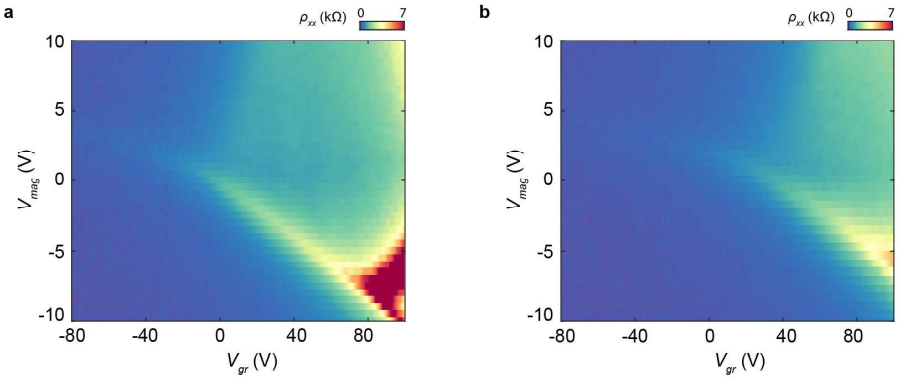

Figure 3.7: **Drifting of the charge doping in graphene over multiple days in Device A. a-b**, Maps of ρ_{xx} acquired by sweeping both gates at $B = 0$ T. The measurements in **a** and **b** were performed three days apart within the same cooldown, under otherwise identical conditions.

The distinction between Regions II and III can be explained by the DOS in the graphene, which is small or vanishing in the former and much larger in the latter. These regions are separated by a resistivity plateau at zero field, and by a crossover at 9 T from the highly extended $\nu = -2$ IQH plateau to a sequence of less extended IQH states with higher filling factors. In Region II, changes in V_{mag} are almost entirely screened. In this region, changing V_{gr} only weakly dopes the graphene because the low DOS means that adding electrons to the graphene causes its electrochemical potential to rise rapidly, leading to more electrons tunneling into the CrI_3. In Region III, changing V_{gr} dopes the graphene more strongly because its DOS is larger. Meanwhile, changing V_{mag} does somewhat dope the graphene, but, strikingly, it does so in the wrong sense. In this case, the IQH states have positive slope indicative of an effectively negative

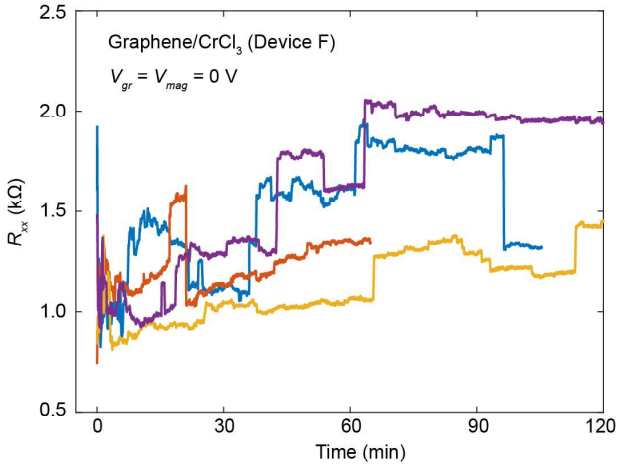

Figure 3.8: **Telegraph noise in the resistance of graphene on $CrCl_3$.** Measurements of the graphene resistance in Device F acquired as a function of time with $V_{gr} = V_{mag} = 0$ at $B = 12$ T. The system is initialized by quickly sweeping from $V_{gr} = 10$ V just prior to the measurement. The measurement is repeated four consecutive times, with each shown in a different color.

differential capacitance. In other words, a more positive V_{mag} results in larger hole doping of the graphene, whereas naively it would be expected to instead reduce the hole doping. This effect is also responsible for the peculiar reversal of the trajectories of the IQH plateaus seen near $V_{mag} = 0$ in the Landau fans shown in Figs. 3.5c-d. Negative differential capacitance can result from negative compressibility in a strongly correlated conductor, such as has been reported for graphene on MoS_2 [144]. It can also result from a large rearrangement of charge in the dielectric induced by a small change in applied electric field, such as occurs when a ferroelectric polarization flips. Rearrangement of the interacting electrons within the CrI_3 therefore seems the most likely explanation for this phenomenon, and is consistent with the associated hysteresis, though it appears too complex to be usefully modeled at this point.

Magnetic order dependence of modulation doping

So far, we have not considered the role of the magnetic ordering of the CrI_3, which exhibits out-of-plane intralayer ferromagnetism (FM) and antiferromagnet (AFM) in-

terlayer ordering at low temperature. Figure 3.9a shows a low-field Landau fan diagram acquired for both positive and negative values of B. As noted earlier, upon increasing the field there is an abrupt jump close to $|B| = 1.6$ T at which all resistance features shift towards more positive V_{gr}, indicating a sudden transfer of electrons out of the graphene. To interpret this, we consider a simple model in which the CrI_3 is a bilayer in order to investigate the origin of this effect, justified by the expectation that the graphene couples most strongly to the nearest few layers of the CrI_3. Ab initio calculations show that the energy of the CrI_3 conduction band depends on its interlayer magnetic ordering, shifting to lower energy as the material undergoes a transition from interlayer AFM to FM (shown in Fig. 3.9b). This transition likely also reduces the energy levels of defect states, and results in additional electrons tunneling into the CrI_3 (see band schematics in Fig. 3.9b). This abrupt jump is absent in Region I, where the states in the CrI_3 remain too high to be occupied (e.g., see Fig. 3.5b). This effect demonstrates that the graphene resistivity is highly sensitive to the interlayer magnetic ordering of the CrI_3. We find that the critical field becomes asymmetric with the sweeping direction of the magnetic field for thicker CrI_3 substrates, indicating that the graphene is only sensitive to the magnetic ordering of the nearest few CrI_3 layers. We'll discuss this in detail in the next section.

The AHE signals are anticipated in graphene endowed with both a magnetic exchange field and Rasbha spin orbit coupling [112, 113, 114, 117, 115], owing to the formation of an inverted gap at the Dirac point and associated Berry curvature at the band edges. We search for the AHE by measuring ρ_{xy} as the magnetic field is swept back and forth at different values of V_{gr} (shown in Figure 3.9c). We see hysteretic loops surrounding $|B| \approx 1.6$ T owing to the AFM/FM transition in the CrI_3, but do not observe hysteresis at $B = 0$. For measurements acquired nearby the Dirac point, we observe nonlinear $\rho_{xy}(B)$ surrounding $B = 0$ reminiscent of a weak AHE. However, we also notice that the Dirac point drifts with magnetic field in the Landau fans shown in Fig. 5.2a and

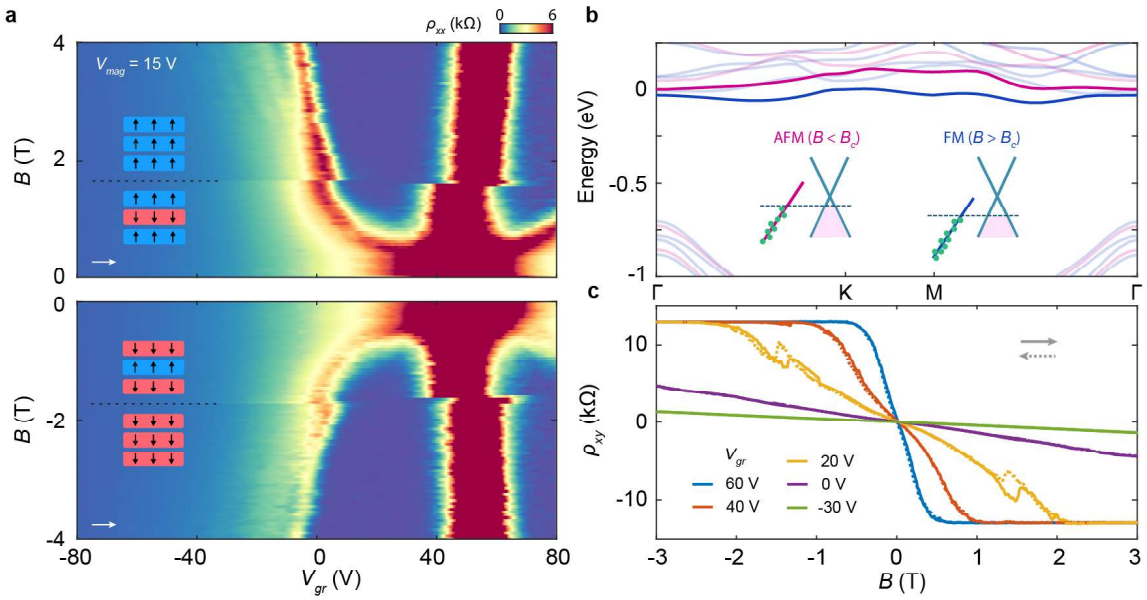

Figure 3.9: **Magnetic field-dependent modulation doping of graphene on CrI_3.** **a**, Low-field Landau fan diagram acquired by sweeping V_{gr} from negative to positive with $V_{mag} = 15$ V. An abrupt shift in the modulation doping is denoted by the black dashed line, corresponding to the critical field at which the trilayer CrI_3 flips between interlayer AFM and FM (illustrated by the cartoon insets). **b**, Ab initio calculation of the band structure of bilayer CrI_3 in the interlayer FM (blue) and AFM (red) states. The lowest conduction band is highlighted for clarity. The cartoon illustrates the additional modulation doping of graphene anticipated in the FM state compared with the AFM state owing to the lower conduction band energy. **c**, ρ_{xy} acquired by sweeping B back and forth at different values of V_{gr}, with $V_{mag} = 15$ V.

Fig. 3.9a. Although we do not understand the origin of this effect, and further find that it is highly sample dependent (shown in Fig. 3.11f), its presence here implies that the charge transfer between the graphene and CrI_3 changes continuously with the magnetic field. As a result, the charge carrier density in graphene also changes with B at fixed gate voltage, potentially driving a nonlinearity in the observed Hall effect that is completely unrelated to the usual AHE mechanism.

Upper limit estimation of the exchange coupling

Careful analysis of the Landau fans can provide further insights into the strength of the magnetic proximity coupling in graphene. As detailed earlier, we observe a four-fold

degeneracy in nearly all of the IQH states in our sample (with only weak signatures of symmetry-breaking at high B), indicating preserved spin and valley degeneracy. The absence of symmetry-broken IQH states is expected given the modest graphene mobility of $\sim$ 5000 cm^2/Vs (shown in Fig. 3.10), presumably resulting from scattering due to defects in the CrI_3 substrate. However, the absence of detectable Landau-level splitting also sets an upper bound on the magnitude of the magnetic exchange coupling, which is expected to act as a Zeeman term that lifts the spin degeneracy at zero field. The magnetic exchange coupling must therefore be less than the smallest resolvable Landau level gap in our measurements. We estimate this to be $\sim$25 meV from the fact that the $\nu = -2$ state fully develops at $B \approx 0.5$ T (shown in Fig. 3.9c), following the expectation that the corresponding cyclotron gap is $\Delta E_{-2} = v_F\sqrt{2\hbar eB}$, where $v_F = 10^6$ m/s is the presumed Fermi velocity of graphene and $\hbar$ is Planck's reduced constant. This is in tension with theoretical predictions of magnetic exchange couplings ranging from tens of meV to as large as $\sim$120 meV in graphene on CrI_3 [145, 146, 147]. Furthermore, unambiguous evidence for a proximity exchange field has been observed in optical spectroscopy measurements of monolayer WSe_2 on a CrI_3 substrate [57, 58]. The apparent unexpectedly small exchange coupling for graphene on CrI_3 may be intrinsic, but it may also be degraded by disorder in the CrI_3 for reasons that are not clear at present. Progress towards a high-temperature QAHE in proximitized graphene will likely require a reduction of the defect concentration in the CrI_3 crystal, or the discovery of more favorable magnetic insulator substrates.

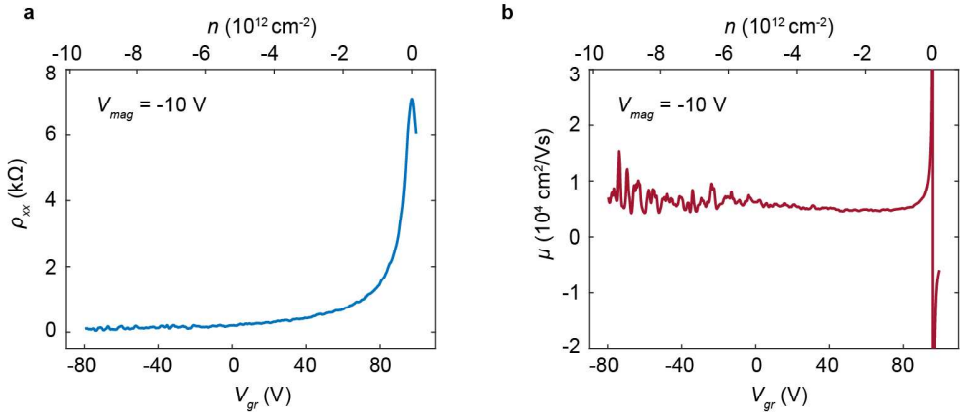

Figure 3.10: **Extraction of the graphene mobility in Device A. a**, Graphene resistivity acquired as V_{gr} is swept at $V_{mag} = -10$ V. The charge transfer is suppressed at this value of V_{mag}, therefore we are able to extract the charge carrier density, n, in the graphene from the known gate capacitance (top axis). **b**, Charge carrier mobility as a function of V_{gr} (bottom axis) and n (top axis), calculated as $\mu = 1/en\rho$.

3.4 Transport in monolayer graphene with 7L and 10L CrI_3

We have studied two graphene/CrI_3 devices (Devices B and C) in addition to the one reported in the main text (Device A). These two devices have thicker CrI_3 substrates of 7 and 10 layers, respectively. Figure 3.11a shows a schematic of Device C, which has graphite top and bottom gates. Figures 3.11b-c show the device resistivity acquired by sweeping one gate back and forth with the other grounded, and Fig. 3.11d shows the resistivity map acquired by sweeping both gates, analogous to the measurements of Figs. 1b-d of the main text for Device A. The basic transport phenomenology is nearly identical between the two devices, including the gate-tunable modulation doping, the bent trajectory of the Dirac point, anomalous resistive peaks and plateaus in the hole-doped regime, and hysteresis confined only to certain portions of the phase diagram. We note that this device appears to be aligned with the encapsulating boron nitride and manifests a weak secondary Dirac point at large hole doping (diagonal feature in the

bottom left of Fig. 3.11d), however, this does not appear to have a meaningful impact on the overall transport properties arising from the graphene/CrI_3 interface. Figure 3.11e shows a similar resistivity map at $B = 12$ T, and Figs. 3.11f-g show Landau fan diagrams of the longitudinal (top) and Hall (bottom) resistivities acquired by sweeping V_{gr} and V_{mag}, respectively, with the other gate held at ground. Again, we see that this device reproduces the salient high-field features of Device A reported in the main text, including a highly extended $\nu = -2$ plateau, nonlinear trajectories of the IQH states, signatures of negative compressibility when tuning V_{mag} in the equivalent of Region III, and an abrupt jump in the modulation doping around the magnetic field at which the CrI_3 becomes a layer ferromagnet.

Figures 3.12a-b show the hysteresis maps of this device acquired at $B = 0$ and 12 T, respectively. As in Device A, the combination of these measurements reveals hysteretic behavior everywhere except the bottom left portion of the map (Region I). Device B also behaves quite similarly overall (shown in Fig. 3.13), indicating excellent reproducibility of the transport properties of graphene/CrI_3 heterostructures.

Sensing the surface magnetic ordering of bulk CrI_3 with graphene

Figure 3.14a (b) shows a Landau fan diagram of a graphene on 10 layer CrI_3 device (Device C) acquired by changing V_{gr} at fixed $V_{mag} = 6$ V, and with B swept from positive to negative (negative to positive) values. We observe one abrupt jump in the modulation doping at all values of V_{gr} for each sign of B, as indicated by the white dashed lines (other small jumps are also occasionally observed, but only occur over small ranges of V_{gr} and likely arise due to randomly moving charges in the CrI_3). Unlike for the 3 layer CrI_3 device in which these jumps occur at the same absolute value of B as discussed earlier, we find an asymmetry in the switching field in the 10 layer device. In particular, the first jump occurs when the field crosses $|B| = 1.9$ T, and the second jump occurs when the opposite sign of the field exceeds $|B| = 0.9$ T.

Magnetic switching at fields of 0.9 T and 1.9 T (in addition to at many smaller

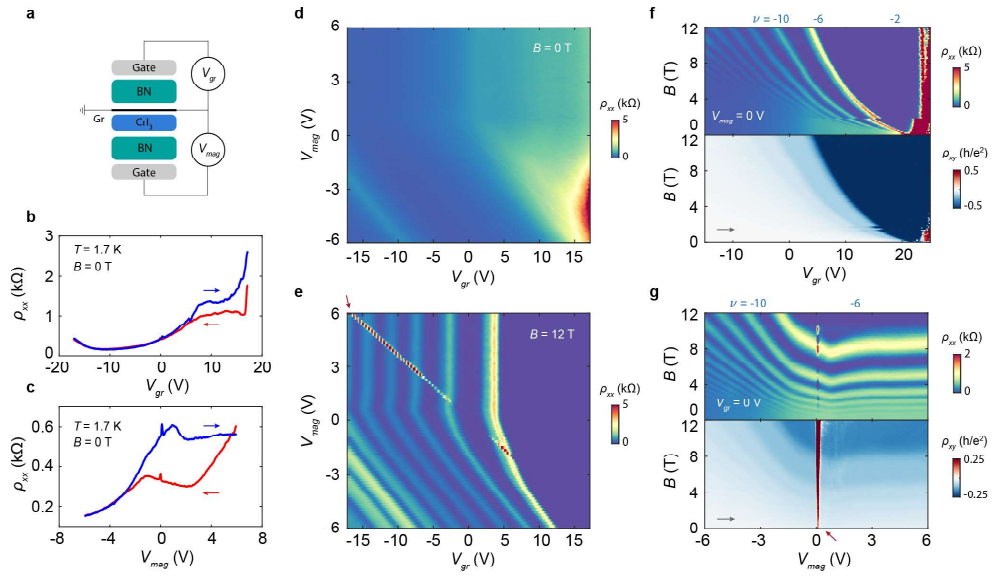

Figure 3.11: **Transport measurements of graphene on a 10 layer CrI_3 (Device C). a**, Cartoon schematic of the device structure. **b**, ρ_{xx} as V_{gr} is swept back and forth with $V_{mag} = 0$ V. **c**, ρ_{xx} as V_{mag} is swept back and forth with $V_{gr} = 0$ V. **d-e**, Maps of ρ_{xx} acquired by sweeping both gates at $B = 0$ T (**d**) and $B = 12$ T (**e**), respectively. **f-g**, Landau fan diagrams acquired by sweeping V_{gr} (**f**) and V_{mag} (**g**), respectively, from negative to positive with the other gate held at ground. Features denoted by red arrows in **e-g** are artifacts arising due to insulating behavior at the contacts.

fields) is routinely observed in magnetic tunnel junction measurements of CrI_3 up to ten layers [21, 139, 148, 149, 150]. These structures, consisting of graphite/few-layer CrI_3/graphite, exhibit symmetric tunneling properties for both signs of the magnetic field. In contrast, our transport measurements are inherently asymmetric, since the graphene layer sits only on one side of the CrI_3. Seeing jumps in the modulation doping at different fields depending on the field sweeping direction indicates that the graphene is sensitive only to the spin configuration of the nearest few CrI_3 layers. The schematics in Figs. 3.14c-d illustrate one possible evolution of the interlayer spin arrangement as the magnetic field is swept. Starting from the interlayer ferromagnetic configuration at high field, our results are consistent with the spins in the CrI_3 layer neighboring the graphene flipping first at $|B| = 1.9$ T. In contrast, the spins in the second layer do not flip until

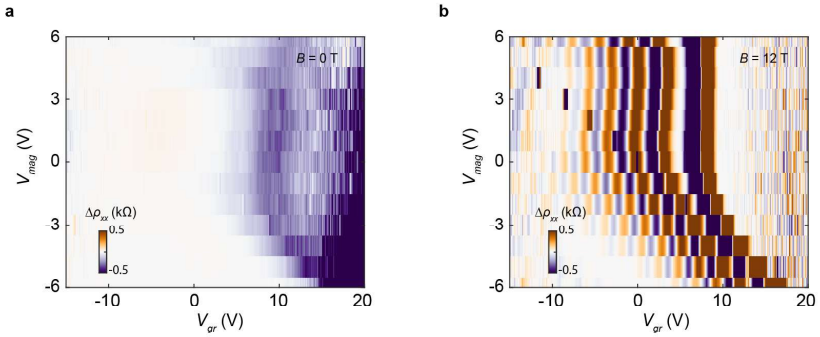

Figure 3.12: **Map of the transport hysteresis in Device C. a-b**, $\Delta\rho_{xx}$ acquired by taking the difference between the resistivity upon sweeping V_{gr} forward and backward at $B = 0$ T (**a**) and $B = 12$ T (**b**).

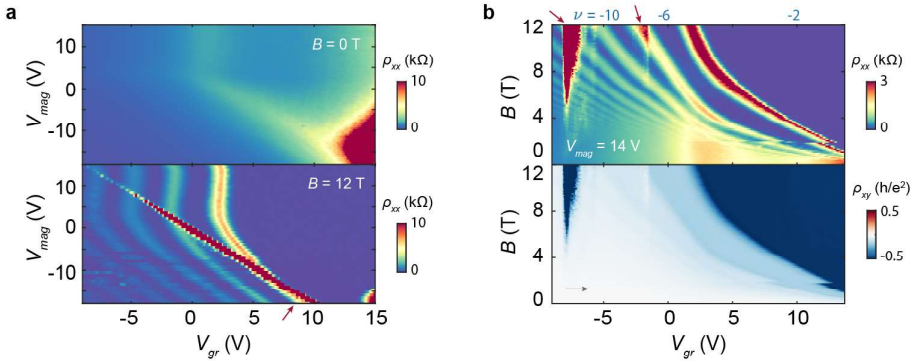

Figure 3.13: **Transport measurements of graphene on a 7 layer CrI_3 (Device B). a**, Maps of ρ_{xx} acquired by sweeping both gates at $B = 0$ T (top) and $B = 12$ T (bottom). **b**, Landau fan diagram acquired by sweeping V_{gr} from negative to positive values with $V_{mag} = 14$ V. Features denoted by red arrows are artifacts arising due to insulating behavior at the contacts.

the field reaches a value of 0.9 T with the opposite sign. The spins in the remaining bulk layers likely flip in a correlated fashion, however, the graphene transport is apparently not sensitive to these spin flips.

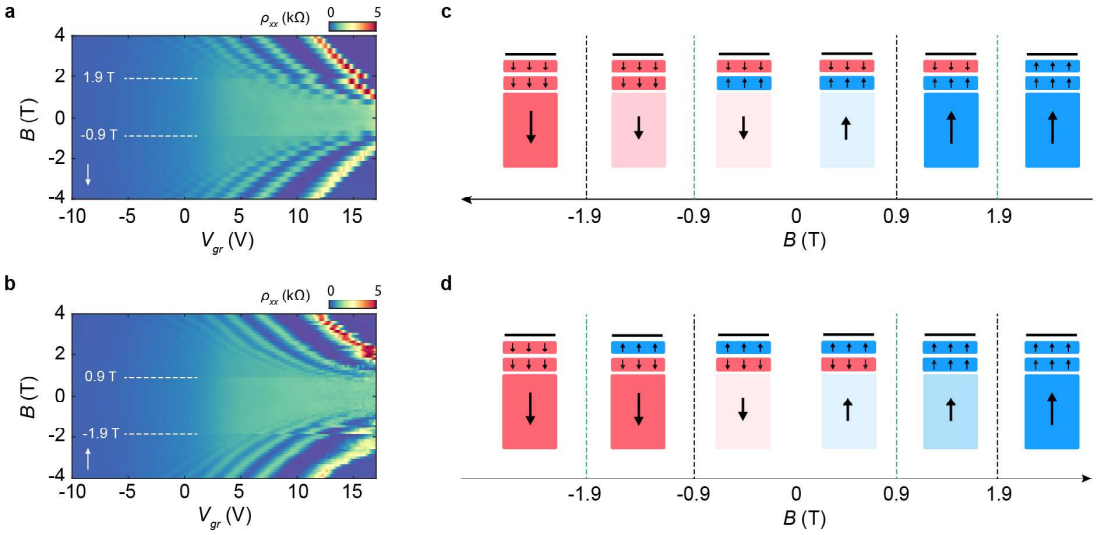

Figure 3.14: **Sensing the magnetic order of nearest few CrI_3 layers with graphene.** **a-b**, Landau fan diagrams measured as the magnetic field is swept from positive to negative (**a**) and from negative to positive (**b**) in a device with graphene on a 10 layer CrI_3 (Device C). $V_{mag} = 6$ V in both measurements. The white dashed lines denote the most robust abrupt jumps in the modulation doping of the graphene, determined as those which span the entire accessible range of V_{gr}. **c-d**, Schematics of the inferred magnetic ordering of the 10 layer CrI_3 as a function of B, for the case of sweeping B from positive to negative (**c**) or visa versa (**d**). The graphene sheet is depicted as the solid black line atop a number of layers of CrI_3. Our measurements are evidently not sensitive to the spin configuration of the outer CrI_3 layers, which we aggregate into one large rectangle and color in light red/blue at intermediate magnetic fields to reflect a complicated (and unknown) interlayer magnetic ordering. Dashed green lines denote the value of B corresponding to the experimentally observed jump in the graphene modulation doping, resulting from spin flips in either the nearest or next-nearest CrI_3 layer.

3.5 Transport in monolayer graphene with $CrBr_3$ and $CrCl_3$

Transport characterization of graphene on $CrBr_3$

We have performed transport characterization similar to that described in the main text for graphene/$CrBr_3$ and graphene/$CrCl_3$ heterostructures. $CrBr_3$ is both an intra- and inter-layer ferromagnet at low temperature. We construct a dual graphite-gated device with a graphene/$CrBr_3$ interface (shown in Fig. 3.15a) and measure the graphene resistivity as a function of each gate (shown in Figs. 3.15b-c). Upon sweeping both gates, we find that the graphene resistivity is very low over the entire accessible range of doping (shown in Fig. 3.15d), with much smaller gate-induced changes in resistivity than in graphene/CrI_3. In a similar measurement at $B = 7.5$ T, we see IQH states that exhibit highly unusual trajectories as a function of gating. These states move nonlinearly with gate voltage, and disperse in the opposite direction than anticipated upon gating with V_{mag} indicative of an apparent negative compressibility.

These observations are corroborated by measurements of the Landau fan diagrams. In the fan acquired by tuning V_{gr} at fixed $V_{mag} = 0$ (shown in Fig. 3.15f), we observe magnetotransport that is mostly consistent with typical highly-doped graphene. The four-fold degenerate IQH states disperse nearly linearly with B, projecting to a very positive V_{gr} indicating large modulation hole doping. Corresponding measurements of ρ_{xy} further corroborate the large filling factors of the IQH states and their hole-type doping. In contrast, the Landau fan acquired by tuning V_{mag} at fixed $V_{gr} = 12$ V is highly atypical, with IQH states dispersing away from the apparent Dirac point over the majority of the accessible gate range (shown in Fig. 3.15g). The upturn of these states at very negative V_{mag} is a consequence of hysteresis in the system. These oppositely dispersing IQH states indicate the negative differential capacitance of the system upon

tuning V_{mag} over the entire accessible gate range of the device. These observations are phenomenologically consistent with Region III of the graphene/CrI_3 phase diagram, and indicate that the electron affinity of $CrBr_3$ is larger than CrI_3. In this case, the lowest electron band of $CrBr_3$ resides below the Dirac point of graphene, resulting in modulation doping that cannot be suppressed with gating.

We do not find any signs of a magnetic exchange field in the graphene, very similar to the case of graphene/CrI_3. We observe an ordinary (linear) Hall effect over the entire accessible gate range (see Fig. 3.16 for a representative example), although this is expected even in the case of a sizable magnetic exchange field since the Berry curvature is likely concentrated close to the Dirac point. However, we do not observe any signatures of degeneracy lifting in the main-sequence IQH states. We follow a similar analysis of the quantum Hall gap as described in the main text to estimate the approximate upper bound strength of the magnetic exchange field as $\sim$15 meV, which is similar to that of graphene/CrI_3. In contrast, calculations suggest exchange couplings of $\sim$70 meV in graphene on $CrBr_3$ [151]. As in graphene/CrI_3, this rough upper bound estimate is much less than the theoretical expectation, and the reason for the discrepancy is not presently clear.

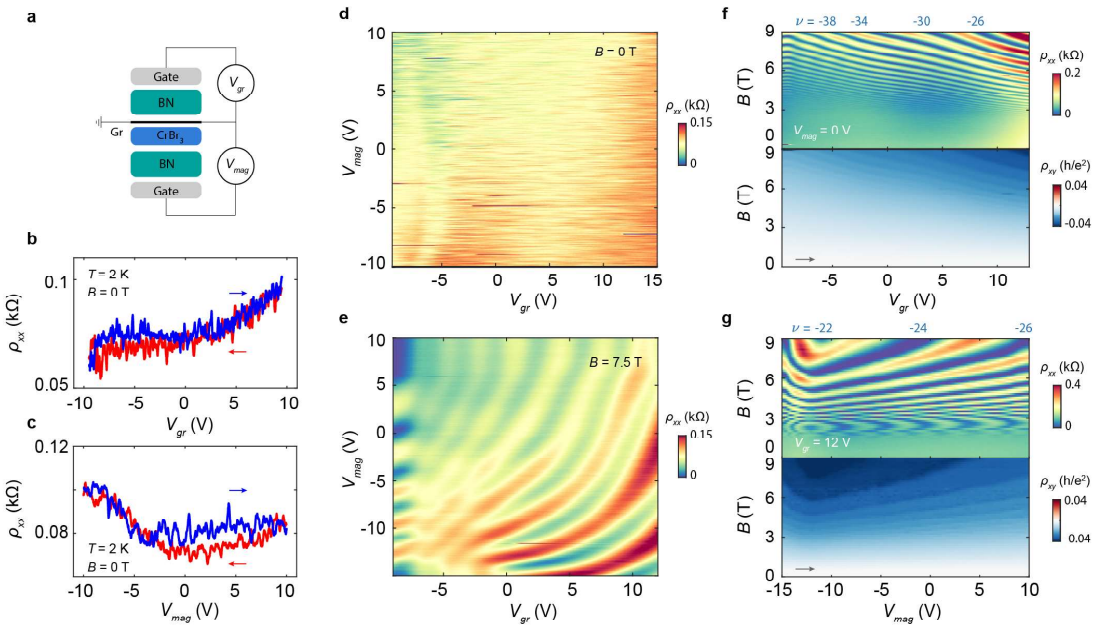

Figure 3.15: **Transport measurements of graphene on a 28 nm $CrBr_3$ (Device E). a**, Cartoon schematic of the device structure. **b**, ρ_{xx} as V_{gr} is swept back and forth with $V_{mag} = 0$ V. **c**, ρ_{xx} as V_{mag} is swept back and forth with $V_{gr} = 0$ V. **d-e**, Maps of ρ_{xx} acquired by sweeping both gates at $B = 0$ T (**d**) and $B = 7.5$ T (**e**), respectively. **f-g**, Landau fan diagrams acquired by sweeping V_{gr} from negative to positive with $V_{mag} = 0$ (**f**), and V_{mag} with $V_{gr} = 12$ V (**g**), respectively.

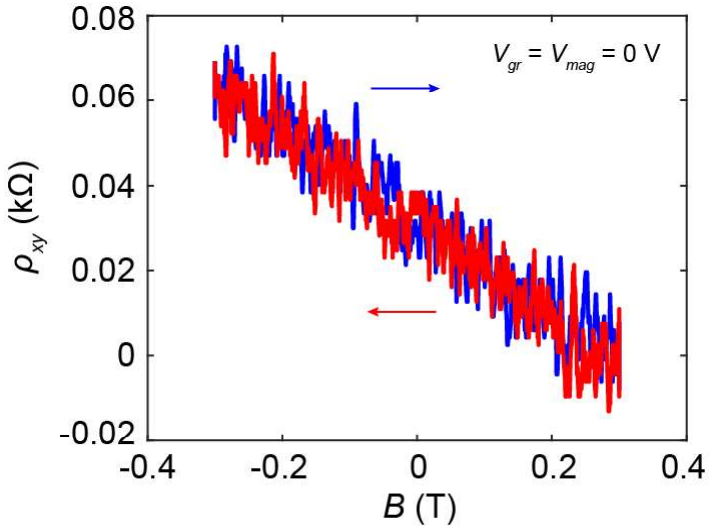

Figure 3.16: **Measurement of the Hall resistance in Device E.** ρ_{xy} measured as B is swept back and forth with $V_{gr} = V_{mag} = 0$ V.

Transport characterization of graphene on $CrCl_3$

$CrCl_3$ is an intralayer ferromagnet and interlayer antiferromagnet. Spins in $CrCl_3$ are aligned in the 2D plane, rather than perpendicular as in CrI_3 and $CrBr_3$, although bulk $CrCl_3$ requires an out-of-plane field of only ≈ 0.25 T to fully polarize its spins out of the 2D plane [152]. In spite of the different magnetic structure, we find that transport in graphene/$CrCl_3$ heterostructures is qualitatively consistent with $CrBr_3$. Figure 3.17a shows the device structure for a sample of graphene on an 80 nm thick $CrCl_3$, and Figs. 3.17b-g show transport measurements analogous to those presented for the graphene/$CrBr_3$ device in Fig. 3.15. Although the exact details differ, the basic properties look very similar. We find that the apparent modulation doping is slightly less in a second device with a 40 nm $CrCl_3$ (shown in Fig. 3.18, as we are just barely able to access the Dirac point by gating. At present, it is not clear what controls the precise amount of modulation doping in graphene/$CrCl_3$ devices. Despite this ambiguity, the majority of the accessible gate range in both devices phenomenologically corresponds to the behavior of Region III described in the main text.

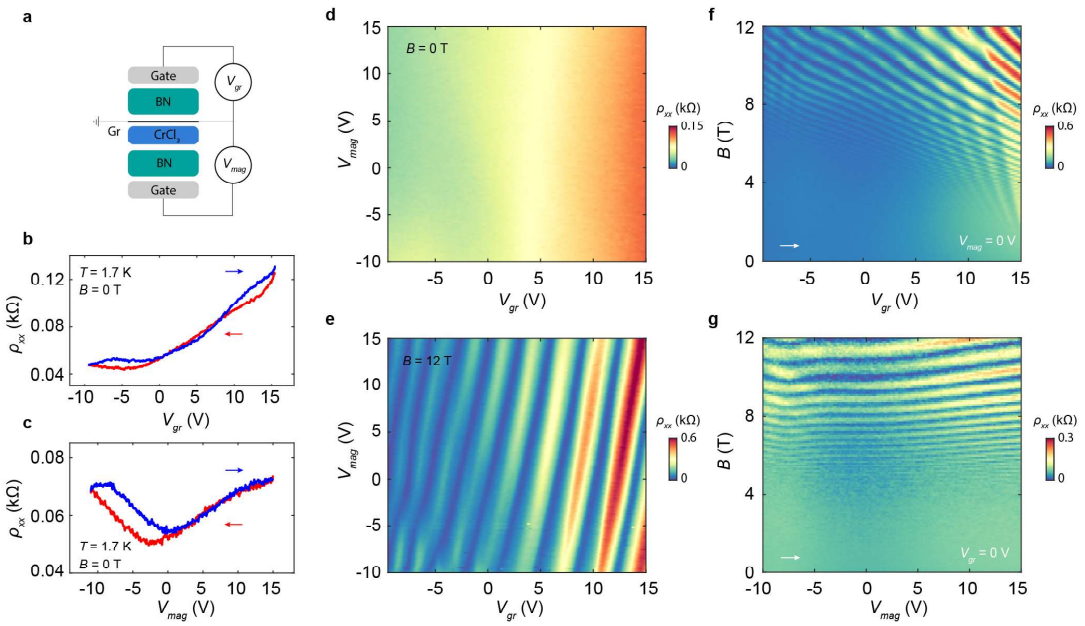

Figure 3.17: **Transport measurements of graphene on a 80 nm $CrCl_3$ (Device G). a**, Cartoon schematic of the device structure. **b**, ρ_{xx} as V_{gr} is swept back and forth with $V_{mag} = 0$ V. **c**, ρ_{xx} as V_{mag} is swept back and forth with $V_{gr} = 0$ V. **d-e**, Maps of ρ_{xx} acquired by sweeping both gates at $B = 0$ T (**d**) and $B = 12$ T (**e**), respectively. **f-g**, Landau fan diagrams acquired by sweeping V_{gr} (**f**) and V_{mag} (**g**), respectively, from negative to positive with the other gate held at ground.

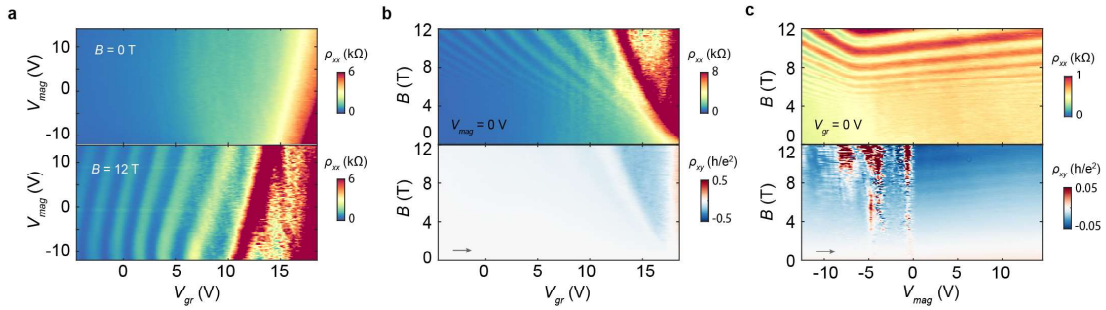

Figure 3.18: **Transport measurements of graphene on a 40 nm $CrCl_3$ (Device F). a**, Maps of ρ_{xx} acquired by sweeping both gates at $B = 0$ T (top) and $B = 12$ T (bottom). **b**, Landau fan diagram acquired by sweeping V_{gr} from negative to positive values with $V_{mag} = 0$ V. **c**, Landau fan diagram acquired by sweeping V_{mag} from negative to positive values with $V_{gr} = 0$ V.

Temperature-dependent transport of graphene/CrX_3

Figure 3.19 shows the resistivity of graphene on CrI_3, $CrBr_3$, and $CrCl_3$ measured as a function of temperature and V_{gr} at fixed V_{mag}. The overall resistivity drifts with temperature in ways that we do not fully understand, however, in the case of CrI_3 we see clear resistivity jumps within a few kelvin of the anticipated magnetic ordering temperature (denoted by the blue dashed line for the case of monolayer CrI_3 and the red dashed line for the case of bulk CrI_3 [153]). This indicates that the onset of magnetism in the CrI_3 impacts the graphene transport, likely by changing the magnitude of the modulation doping as the band edge shifts. Similar effects have been observed previously in graphene/$RuCl_3$ heterostructures [154]. The resistivity drifts over a much wider range of temperature for $CrBr_3$ and $CrCl_3$ substrates, and the potential connection of these features with magnetic ordering is less clear.

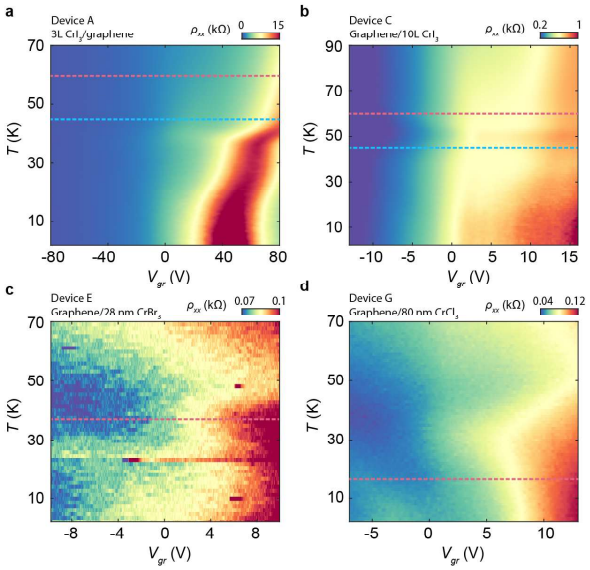

Figure 3.19: **Temperature dependence of the graphene resistivity on various CrX_3 substrates. a-b**, ρ(T) as a function of V_{gr} in graphene/CrI_3 for Device A (**a**) and Device C (**b**). The blue (red) dashed line indicates the magnetic ordering temperature for monolayer (bulk) CrI_3. **c-d**, Similar measurements for **c**, $CrBr_3$ (Device E) and **d**, $CrCl_3$ (Device G). The red dashed lines indicate the bulk magnetic ordering temperature of these materials. V_{mag} is 15 V in **a**, 0 V in **b** and **d**, and 10 V in **c**.

3.6 Transport in a graphene/WSe_2/CrI_3 heterostructure

Interfacing graphene with WSe_2 is known enhance the SOC of the graphene [155, 156, 157, 92, 42]. We have additionally fabricated devices in which there is a monolayer of WSe_2 in between the graphene and the CrI_3. We find that even with the monolayer WSe_2 spacer layer, there is similar modulation doping of the graphene due to charge transfer with the CrI_3. Figure 3.20 summarizes our primary observations in this device. Overall, we find that transport in this structure closely resembles the graphene/CrI_3 devices. We observe an ordinary Hall effect even very near the Dirac point (shown in Fig. 3.21), indicating the absence of the AHE in this system.

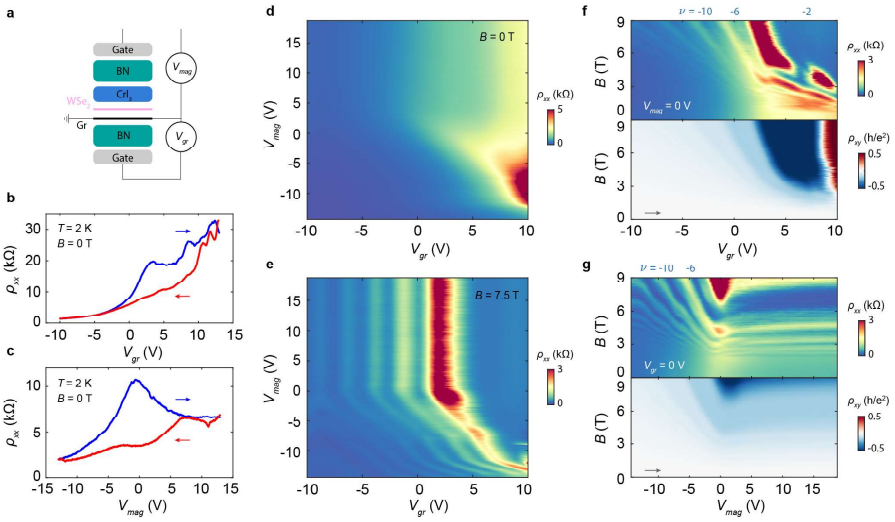

Figure 3.20: **Transport measurements in 3 layer CrI_3/monolayer WSe_2/graphene device (Device D). a**, Cartoon schematic of the device structure. **b**, ρ_{xx} as V_{gr} is swept back and forth with $V_{mag} = 0$ V. **c**, ρ_{xx} as V_{mag} is swept back and forth with $V_{gr} = 0$ V. **d-e**, Maps of ρ_{xx} acquired by sweeping both gates at $B = 0$ T (**d**) and $B = 7.5$ T (**e**), respectively. **f-g**, Landau fan diagrams acquired by sweeping V_{gr} (**f**) and V_{mag} (**g**), respectively, from negative to positive with the other gate held at ground.

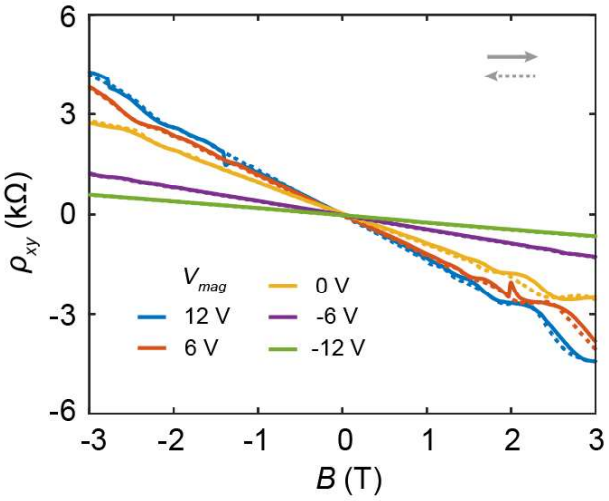

Figure 3.21: **Hall measurement in Device D.** ρ_{xy} measured as B is swept back and forth with $V_{gr} = 0$ V at different V_{mag}. Solid (dashed) lines denote the forward (backward) sweeping direction.

Chapter 4

Investigation of graphene-WTe_2 structures

Beyond graphene, tungsten ditelluride (WTe_2) is another well-known and intriguing layered semimetal, which features the topological properties and strong SOC effects. Combining these two materials into a heterostructure offers two potential advantages: first, the possibility of endowing graphene with a large proximity-induced SOC, and second, the possibility of controllably screening many-body interactions in WTe_2 by varying the doping of the proximate graphene sheet. The latter is crucial to study the mysterious nature of the correlated insulating state and superconductivity in WTe_2. In this work, we investigate the transport properties of graphene-WTe_2 heterostructures and study the correlated gap behavior of WTe_2 with the influence of an adjacent graphene.

4.1 Introduction to monolayer WTe_2

Monolayer 1T'-WTe_2 has emerged as a material of immense interest in the realm of condensed matter physics due to its diverse and intriguing physical properties. It features a range of exotic states that include quantum spin Hall states [13, 14, 15], gate-induced su-

perconductivity [12, 25], and the correlated insulator likely associated with the excitonic insulator [26, 27]. The quantum spin Hall effect features the helical edge states with the bulk insulating property. This effect in monolayer WTe_2 at the charge neutrality was examined by the transport measurement [13, 14], showing the nearly quantization of the two-terminal conductance. Microwave impedance microscopy (MIM) measurements directly image the edge state by probing the local conductivity [15]. When the monolayer WTe_2 is doped away from the neutrality point, a superconductivity can be induced with the critical temperature around 1K [12]. Unconventional quantum criticality are investigated by Nernst experiments to study the nature of the superconductivity [25]. Furthermore, the transport and thermodynamic measurements suggest the monolayer WTe_2 doesn't follow the trivial "band insulator" picture [26]. The V-shaped dependence on electrostatic doping with the gap forming at the neutrality implies the electron-hole pairs (excitons) in the equilibrium. The Hall anomaly associated with convergent σ_{yx} signal also violates the single-particle band insulator [27]. These results highlight the various correlated phases in monolayer WTe_2.

Understanding the details of the band structure and the correlated gap can give the insights into the mechanism of exotic phases in in monolayer WTe_2. However, there are large discrepancies about the band crossing from the early experiments and theoretical prediction. Angle-resolved photoemission spectroscopy (ARPES) [24, 158], STS [24] measurements and calculation [159] show that a gap opens with the size up to 50 meV at the charge neutrality while other calculation [160] and quasiparticle interference (QPI) measurements [161] suggest a overlapping band picture. One possible reason for the inconsistency might be arise from the material quality prepared by different methods, including the film growth and exfoliation. Although monolayer WTe_2 is now believed to possess a correlated gap, studying the evolution of electronic band structure in the same crystal through a tuning knob will give more insights into the nature of the correlated gap. It's known that the controlling the Coulomb screening effect can alter

the electron interaction to further modify the correlated gap [162]. By constructing the dual gated graphene-WTe_2 structure, we are able to investigate the gap nature at various graphene carrier densities related to different degrees of the screening effect, facilitating our understanding about the underlying relation among exotic phases in WTe_2 .

4.2 Experimental setup and methods

In this work, we present the results on two graphene-WTe_2 devices with two different configurations. All graphite and BN crystals are mechanically exfoliated onto a SiO_2/Si substrate at the ambience while the air-sensitive WTe_2 is exfoliated in a nitrogen-filled glovebox (O_2 and H_2O concentrations below 0.5 ppm). For the first graphene-WTe_2 device MW1, the whole structure is assembled using standard dry-transfer techniques with a polycarbonate/polydimethyl siloxane stamp and then deposited onto a Si/SiO_2 wafer. Standard electron-beam lithography, CHF_3/O_2 plasma etching, and metal deposition techniques (Cr/Au) were used to define the complete stack into a Hall bar geometry. For the second graphene-WTe_2 device MW2, it includes more steps in the device fabrication with an additional graphene sensor to directly probe the chemical potential. The bottom part of the whole structure is prepared by covering the bottom graphite with a BN flake using the dry-transfer. After removing the PC polymer in chloroform, the stack is cleaned by annealing at 400 ℃ for 2h. Thin Pt metal contacts for graphene/WTe_2 are evaporated on the BN and then are cleaned by AFM with the contact mode. Second transfer applied is to move the graphene/WTe_2/BN onto the first graphite/BN stack. The Pt contacts for the graphene sensor is deposited onto the second the BN surface and again cleaned by AFM. The last transfer is to bring the monolayer graphene (graphene sensor)/BN/graphite on the previous graphite/BN/graphene/WTe_2 stack. During the transfer, we need to carefully align the flakes to avoid the short among the two graphene sheets and two set of Pt metal contacts. Last, the Au metal contacts are evaporated to

complete the device.

4.3 Transport in monolayer graphene with 1L WTe_2 - MW1

MW1 device is to study the transport properties in graphene with a monolayer WTe_2, which is exfoliated by the crystal with the residual resistance ratio (RRR) of a few hundreds. Figure 4.1a-b show a schematic and an optical image of the device structure we fabricate. Interfaces of graphene and WTe_2 are encapsulated with BN and surrounded by two graphite gates. Due to the asymmetric geometry, these two gates can in principle have distinct impacts on the transport properties, like what we see in graphene/magnets in the previous section. The voltage applied on the top gate close to WTe_2 is denoted as V_W while the other is detonated as V_g.

Atypical gate dependence induced by charge transfer

The resistivity map acquired by sweeping both of the gates at a temperature of $T = 1.7$ K is shown in figure 4.1c. We see atypical features that are not consistent with the pristine graphene encapsulated only with BN and there are some similarities and differences compared to graphene/CrX_3. First, the transport behaved notably differently depending on which of the two gates is swept. The graphene charge neutrality point (CNP) moves from V_{gr}= 0 V to the large V_{gr} when V_W is kept at 0 V, implying the charge transfer between graphene and WTe_2. Figure 4.1d shows the schematics how the work function mismatch leads to the charger transfer. Both materials are charge neutral with different the work function before assembly. Due to the large work function in WTe_2, the electrons tend to populate into WTe_2 from graphene when they are in contact, resulting the hole-doped graphene and electron-doped WTe_2 in equilibrium at zero gate voltages. Although the graphene CNP is close to a linear feature in the resistivity map,

the trajectory does not evolve with the two gate voltages as anticipated from simple electrostatics. The nearly vertical slope in graphene CNP implies the insensitivity to V_W, which is likely from the screening by WTe_2. In addition to the graphene shift, we observe the kinks in the resistivity linecuts close to the $V_g = V_g = 0$ V and appears roughly along the diagonal line across the resistivity map in Fig. 4.1c. We attribute this feature to the neutrality point of WTe_2, which will be verified in the dual-gated maps at finite fields and Landau fan diagram later.

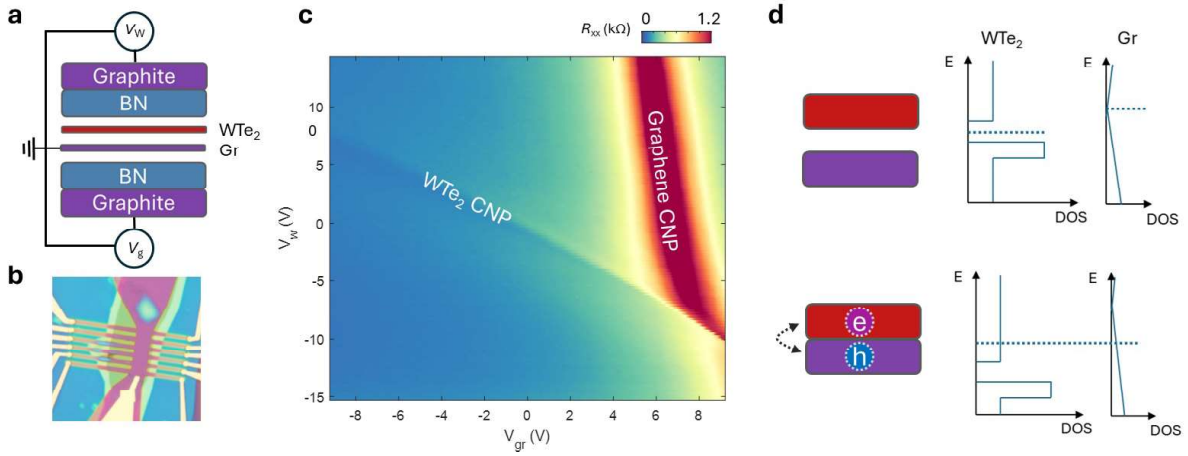

Figure 4.1: **Transport in graphene/WTe_2 MW1 device at zero magnetic field.** **a**, Schematic of the device structure. Monolayer graphene is interfaced with WTe_2 and encapsulated by BN. The voltage on the gate facing the graphene is V_g, and the voltage on the gate facing the WTe_2 is V_W. **b**, An optical image of MW1 device. **c**, Resistance map as a function of the V_g and V_W. The panel above (to the right of) the colour map shows cuts of R_{xx} and R_{xy} as V_g (V_W) is swept with $V_W = 0$ ($V_g = 0$). **d**, Schematics of band alignment and charge transfer between graphene and WTe_2. In their pristine form, they are both charge neutral, so no free carrier exists inside the materials. The chemical potential denoted by dashed line lies within the WTe_2 gap and at the Dirac point in graphene. The two chemical potentials are not at the same energy level due to the different work function. After the graphene is in contact with WTe_2, the charger transfer occurs to reach the equilibrium of the chemical potential, leading to the hole-doped graphene and electron-doped WTe_2. The red (purple) rectangle denote the WTe_2 (graphene).

Figures 4.2a-b show maps of the R_{xx} and R_{xy} acquired by sweeping both of the gates at $B = 0.5$ T. The magnetic field contributes to the formation of Landau levels in the

graphene, leading to the quantum oscillation. This map clearly shows the two regions separated by the diagonal line features, and within each region the quantum oscillations evolve with the similar slopes and indicates the insensitivity to the WTe_2 gate across the whole map. The sharp shifts of quantum oscillations and graphene CNP cross the diagonal line suggest that the chemical potential experiences an incompressible state, which is likely associated with the WTe_2 gap.

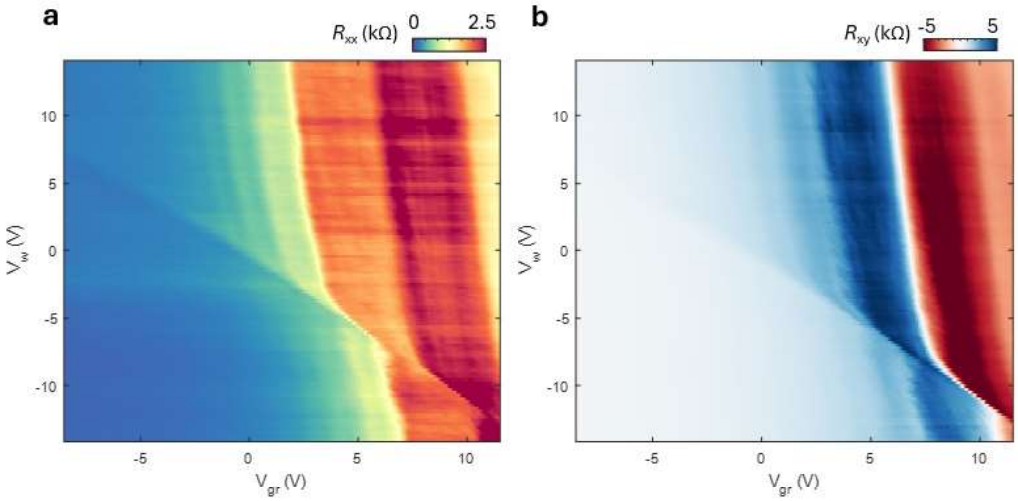

Figure 4.2: **Transport measurements of Device MW1 at $B = 0.5$ T a-b**, Maps of R_{xx} (**a**) and R_{xy} (**b**) acquired by sweeping both gates at $B = 0.5$ T. Quantum oscillation emerges on the whole map. The trajectories of quantum oscillations is close to be vertical due to the screening effect and the pronounced shift of quantum oscillations along diagonal line is possibly related to the WTe_2 gap.

Atypical features in Landau fan diagrams

Transport measurements in the finite magnetic fields with sweeping the gate voltage help to reveal the origin of the intricate features. Figure 4.3a shows Landau fan diagrams of the longitudinal resistivity R_{xx} acquired by sweeping V_g from negative to positive bias with fixed values of $V_W = 0$ V. This Landau fan diagram exhibits a number of anomalous features. First, the extremely wide IQH plateaus fan out nonlinearly and not described by the Středa formula, resulting from the screening by the carriers residing in

the WTe_2. This behavior provides the evidence of the nonlinear relationship between the gate voltage and the charge carrier density in the graphene originating from the charge transfer with the WTe_2, consistent with the bent trajectory of the Dirac point in Fig 4.1c and Figs 4.2a-b. The similar feature is reported in several graphene-based structure, including graphene-SiC [142, 143], graphene-CrX_3, and graphene-CrOCl [55]. Second, the absence of quantized R_{xy} and zero R_{xx} implies that carrier in WTe_2 contribute to transport to some degree. When WTe_2 is doped, it becomes a metal or even a superconductor at the lower temperature. The conducting WTe_2 can directly modify the transport results in this hybrid structure where two materials conduct in parallel or conducting WTe_2 might break topological protection in graphene. Either effect can cause the the failure of the quantum Hall effect. Last, we observe the clear jumps of Landau fans marked by the black dashed lines, also shown in Figure 4.3b. The similar effect was reported in twisted trilayer graphene (tTLG) [163], where the low-energy band can be described by the superposition of a flat band and a Dirac cone. The jump of Landau fan occurs when the Landau levels from Dirac cone move across the correlated gap in tTLG. In contrast, the Landau level likely experiences the gap in WTe_2 in our case. Figure 4.3c shows the schematics about the band alignment between WTe_2 and graphene Landau level. The point A (B) labeled in Fig. 4.3b corresponds to the configuration where the valence (conduction) band matches the graphene $N = 1$ Landau level. The regions where the jump occurs is consistent with diagonal line in the resistivity map at the zero and finite fields, confirming those kinks in resistance is related to WTe_2 gap. In principle, we are able to study the gap evolution versus graphene densities from Landau fan diagrams acquired by different V_W by knowing the knowing information about the Landau level cyclotron energy, the electric field from V_g on WTe_2 and the screening effect from graphene carriers on WTe_2. However, there are some uncertainties in the model. One assumption in the model is that the gap is not dependent on the magnetic field and electric field. From the current results the field dependence of the gap remains unclear.

Furthermore, there are free parameters, separation between graphene and WTe_2 and the relative permittivity of WTe_2, greatly affecting the extracted gap values ranging from tens of 10 meV up to 100 meV. Therefore, the extraction of the accurate gap size in WTe_2 from the current results remains challenging.

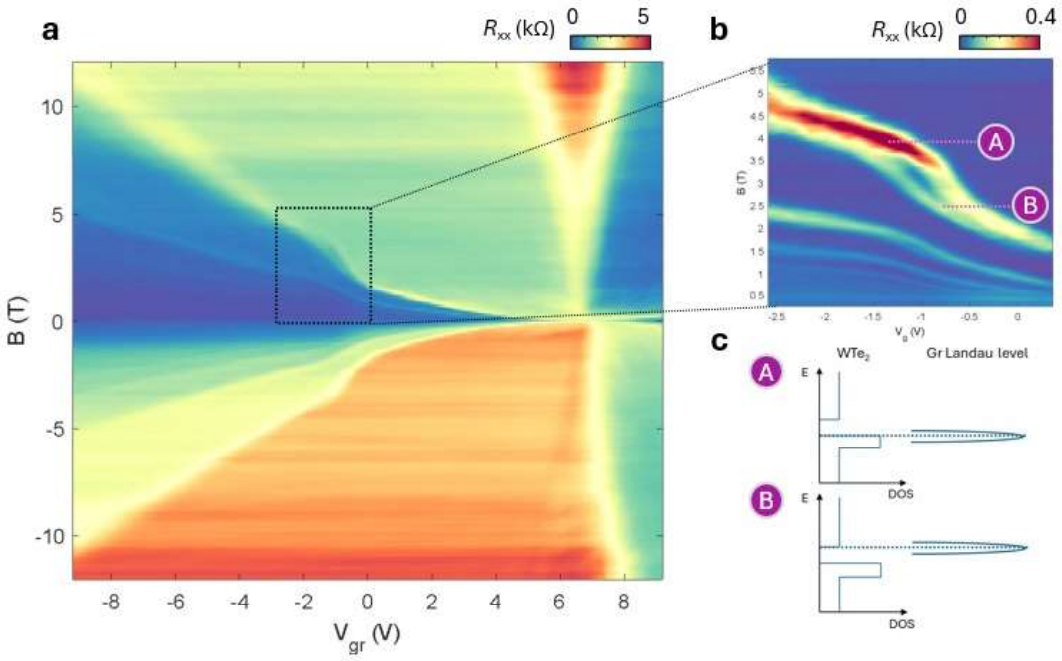

Figure 4.3: **Atypical Landau fan diagrams of graphene/WTe_2.** **a**, Longitudinal resistance R_{xx} of Device MW1 acquired by sweeping V_{gr} from negative to positive values with $V_W = 0$ V. Wide and not well-defined quantum Hall plateaus in graphene are detected due to the conducting WTe_2. **b**, A zoom-in figure from the region enclosed by the black dashed line in Figures 4.3a. Point A and B are to denote the location where the trajectory slope changes. **c**, Schematics of the band alignment between WTe_2 and graphene $N = 1$ Landau level. Point A (B) corresponds to the configuration when the $N = 1$ graphene Landau level is across the WTe_2 valence (conduction) band edge.

Absence of the resistance hump above 120 K

The nature of the WTe_2 gap is believed to be related to the exciton condensation. It was reported that below 100 K the collective excitonic insulator state probably forms at the neutrality point and they coexist with free carriers even above 100 K [26]. Figures 4.4a show maps of the R_{xx} acquired by sweeping both of the gates at $T = 5$, 80

and 120 K. The diagonal line feature remains robust until $T = 80$ K and disappears at $T = 120$ K. Figure 4.4b shows the R_{xx} as a function of V_g at $V_W = 0$ V at several temperatures. Again the kink in the resistance around $V_g = 0$ V is pronounced up to 80 K and gradually fades away above the 120 K, which is consistent with the reported observation. The results obtained from the MW1 device demonstrates that the kinks in the resistance maps and Landau fans are intimately related to the correlated gap in V_W and hence we should be able to further investigate the gap nature using the different approaches in other devices.

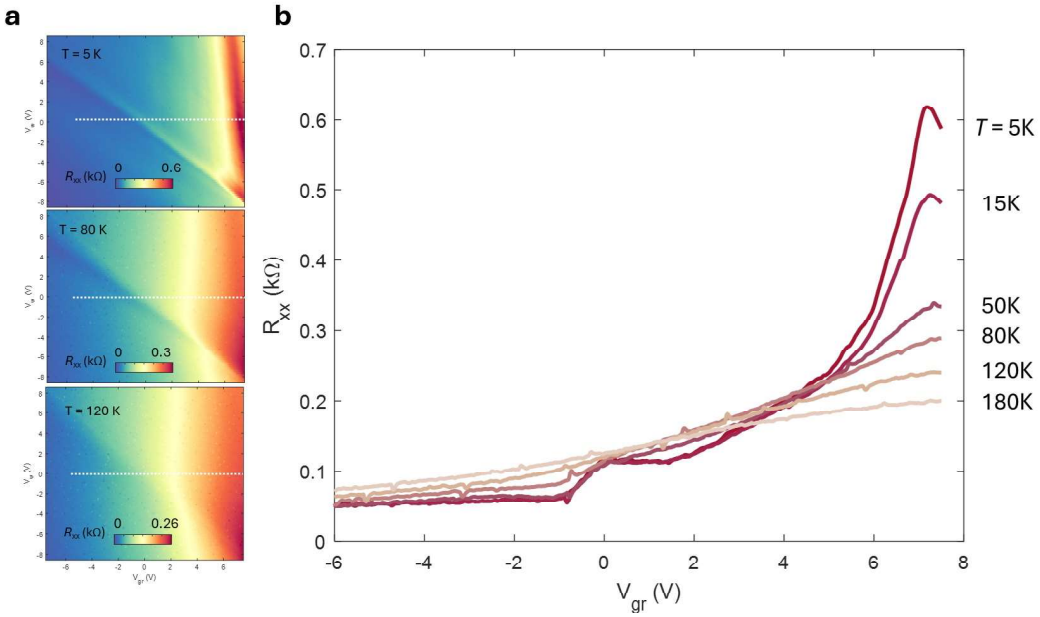

Figure 4.4: **Temperature dependence of the resistance in Device MW1. a**, Zero-field maps of R_{xx} acquired by sweeping both gates at $T = 5$ K (top), $T = 80$ K (middle) and $T = 120$ K (bottom). The resistance hump features gradually fades out as the temperature increases and survives at least up to 80 K. **b**, R_{xx} as V_g is swept (denoted by white dashed lines in Fig. 4.4a) with $V_W = 0$ V at multiple temperatures. These linecuts again demonstrate the hump feature smeared out above 120 K.

4.4 Transport in monolayer graphene with 1L WTe_2 - MW2

MW2 device is to study the transport properties in graphene with a monolayer WTe_2, which is exfoliated by the crystal with the RRR larger than 3000. The larger RRR usually indicates better crystal quality. Therefore, it will be important the compare the results between MW1 and MW2 device to obtain the insights about the WTe_2 properties from different crystals. Figures 4.5a-b show a schematic and an optical image of the device structure we fabricate. There is an additional monolayer graphene sensor to directly probe the chemical potential for the hybrid graphene-WTe_2 structure. The discussion about the chemical potential measurement will be reported elsewhere. Four Pt metal contacts are deposited for probing the transport for hybrid graphene-WTe_2 structure, in which two gates are capable of independently controlling the electric field and carrier density.

Atypical gate dependence induced by charge transfer

Figure 4.5c shows a map of the device resistivity acquired by sweeping both of the gates and the resistivity measured as V_g (V_W) swept back and forth with the other gate grounded at a temperature of $T = 1.7$ K in the top (right) part. The whole resistance map resembles the map measured in MW1. First, the charge transfer due to the work function mismatch between graphene and WTe_2 results in shift of the graphene CNP. Second, the charge residing in WTe_2 can largely screen the field effect by V_W, leading to a nearly vertical slope of the graphene CNP trajectory in the resistance map. Third, the resistance hump emerges along the diagonal line and we attribute this feature to the WTe_2 gap in the previous section. The wider and pronounced resistance hump observed in MW2 is likely related to the more robust incompressible state in WTe_2 exfoliated from the different crystals. Figure 4.5d summarizes the schematics of the band alignment

models between graphene and WTe_2 with the different gate voltage configurations. By controlling the V_W and V_g, we are able to investigate the distinct regimes where the chemical potential is across the graphene and WTe_2 bands with different combinations.

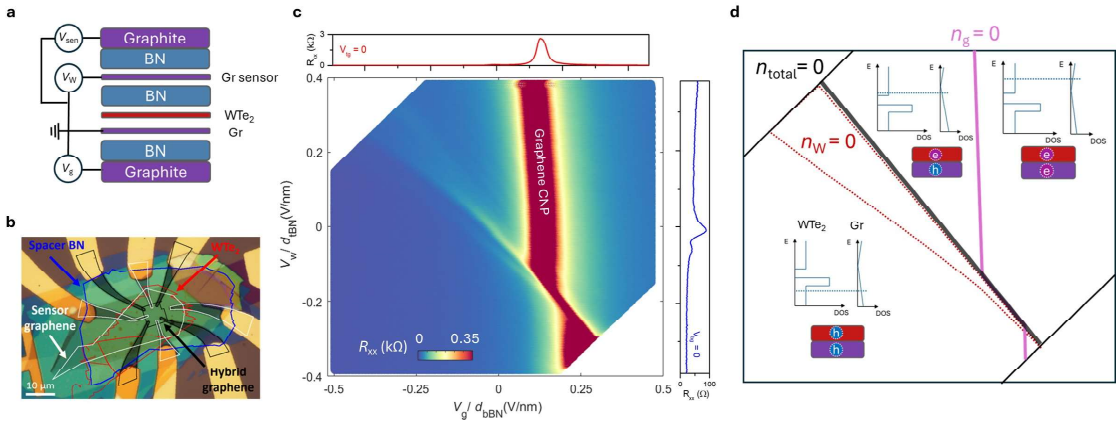

Figure 4.5: **Transport in graphene/WTe_2 MW2 device at zero magnetic field.** **a**, Schematic of the device structure. Monolayer graphene is interfaced with WTe_2 and encapsulated by BN with a additional graphene sensor. The voltage on the graphene sensor is V_W, and the voltage on the gate facing the graphene is V_g. There is the third gate on the top to make graphene sensor charge neutral for the chemical measurements. **b**, An optical image of MW2 device. Graphene sensor, WTe_2 and graphene in the hybrid structure are marked by the white, red and black lines, respectively. **c**, Resistance map as a function of the V_g and V_W. The panel above (to the right of) the colour map shows cuts of R_{xx} and R_{xy} as V_g (V_W) is swept with $V_W = 0$ ($V_g = 0$). Overall map looks like it in Device MW1, but the diagonal hump feature becomes more pronounced. **d**, Schematics of band alignment and charge transfer between graphene and WTe_2 across the resistance map. The graphene CNP is denoted by a pick line whereas the WTe_2 gap region is enclosed by the red dashed lines. The insulating WTe_2 region is accurately defined by the resistance map at the finite field discussed later. In their pristine form, they are both charge neutral, so no free carrier exists inside the materials. After the graphene is in contact with WTe_2, the charger transfer occurs to reach the equilibrium of the chemical potential. In the presence of V_W and V_g, the different configurations of the band alignment can be realized.

Emergence of well-defined graphene integer quantum Hall states

The integer quantum Hall effect from the graphene in the presence of the magnetic field can reveal more features to understand the transport properties. Figures 4.6a-b

show maps of the R_{xx} acquired by sweeping both of the gates at $B = 4$ and 9 T. The formation of quantum oscillations occurs from the Landau levels when the magnetic field is applied, which is similar to what is seen in MW1 in Figs 4.2. However, there is a striking difference in the maps between these two devices. A clear zero R_{xx} region shows up along the diagonal line and is consistent with the WTe_2 insulating region marked in Fig. 4.5d. The near vertical quantum oscillations at the top right and bottom left parts of the map are interpreted as being induced by the screening from the conducting WTe_2 whereas the slope of quantum oscillations within the diagonal region is rather close to the trajectory predicted in monolayer graphene sandwiched by two insulating BN flakes from the electrostatic model, suggesting the insulting WTe_2. Figures 4.6c,e show the resistance measured as a function of V_g with the $V_W = 0$ V at $B = 4$ and 9 T. Within the yellow region corresponding to the WTe_2 insulating region, we observe the well-defined quantum Hall effect with the zero R_{xx} and quantized R_{xy} related to the conventional monolayer graphene's filling factors with four-fold degeneracy. Outside the yellow region, the WTe_2 is either electron-doped or hole-doped and becomes conducting to participate in the transport. Figure 4.6d shows the schematic to describe the transport in the hybrid structure when WTe_2 is insulating or conducting. When the chemical potential lies within the WTe_2 gap, the transport is only dominated by quantum Hall states in graphene at the finite fields. In contrast, when the chemical potential goes into the conduction or valance band, the conducting WTe_2 can contribute to the transport and interfere with the edge states in graphene, causing the destruction of the quantum Hall effect. This robust WTe_2 insulating region in MW2 potentially originates from less in-gap states or a larger band gap in the new crystals.

The well-developed quantum Hall effect in graphene allows us to define the precise WTe_2 insulating region enclosed by the points with the change in slope of the quantum oscillations happen when the chemical potential touches the WTe_2 band edges. Resistance map at $B = 2$ T is selected to define the WTe_2 gap region since sufficient

well-developed Landau levels emerge across the whole map at this field. Figure 4.7a shows the resistance map measured as a function of nominal graphene carrier density n_g and nominal displacement field D_n at $B = 2$ T with the cyan dashed lines to mark the WTe_2 gap region. n_g and D_n reflect the real carrier density and displacement field induced in graphene within the WTe_2 gap region while n_g and D_n are not meaningful to graphene in other region since the carrier can also move into WTe_2 and screen the displacement field. For the rest of the discussion, we'll focus on this WTe_2 gap region and investigate its properties. One question raised in the previous question is how the magnetic field affects the WTe_2. We could first address this question by observing the gap regions at different magnetic fields. Figures 4.8a-c show the resistance map measured as a function of nominal graphene carrier density n_g and nominal displacement field D_n at $B = 0$, 1, 6 T with the cyan dashed lines defined at $B = 2$ T from Fig. 4.7a. We see the cyan dashed lines enclose the hump features in the resistance map at $B = 0$ T and nicely cross over the points where the change in the slope of the quantum oscillation trajectory occurs at the finite fields, suggesting the WTe_2 is possibly not sensitive to the magnetic field.

Extraction of WTe_2 gap size by Landau level cyclotron energy at finite fields

The WTe_2 gap size can be extracted quantitatively by the Landau level cyclotron energy $E_{cyc} = \pm v_F\sqrt{N\hbar eB}$, where $v_F = 10^6$ m/s is the Fermi velocity of graphene, $\hbar$ is Planck's reduced constant , N is the Landau level index and +(-) is used for the electron (hole) carrier in graphene. The numbers marked in Fig. 4.7a corresponds to Landau level indices and the red (blue) colors denotes the Landau levels on the dashed line matching the WTe_2 valence (conduction) band edge shown in the schematics of Figure. 4.7b. The energy of each Landau level across WTe_2 band edges as a function of D_n is plotted in Fig. 4.7b. We fit two sets of points into two polynomial functions and the energy difference between these two functions is the gap size in WTe_2. The same method can

be applied to extract the gap size at different fields, but it can be unreliable at the high fields since there are much less Landau levels and it causes the large uncertainty for the fitting process. Figure. 4.7c shows the extracted WTe_2 gap size as a function of n_g at the several magnetic fields up to 6 T. The extracted gap values obtained from different magnetic fields are quite similar and hence this quantitative result again confirms that the gap less likely depends on the magnetic field. The gap value approaches 46 meV around the graphene CNP in our hybrid structure consistent with reported 40-50 meV in the WTe_2, validating the gap extraction method. We observe that the gap ranges from 38 to 49 meV and decreases monotonically versus n_g. A simple interpretation is that the Coulomb screening from the graphene carrier controls the electron correlation and causes the reduction of the WTe_2 gap value. However, the electric field is another potential tuning knob that might play a role in modifying the WTe_2 gap, though the electric field dependence of the gap still remains unclear from the previous work. Moreover, we do observe the gap behaves with a concave feature only at the 1 T, which is difficult to explain solely by the screening effect of which the strength is monotonically related to n_g. Therefore, it's crucial to investigate the gap at 0 T by different approaches to explore the mechanism for the gap modification.

Extraction of WTe_2 gap size from graphene chemical potential and electrostatics at zero field

The Fermi energy in monolayer graphene at 0 T is given by $E_{F,mg} = \pm\hbar v_F\sqrt{\pi n}$, where $v_F = 10^6$ m/s is the Fermi velocity of graphene, $\hbar$ is Planck's reduced constant , n is the carrier density and +(-) is used for the electron (hole) carrier in graphene. The left schematic in Figure. 4.9a show the concept of the gap extraction method we introduce early. For a given D_n, the WTe_2 conduction and valence band edges corresponds to the two distinct carrier density values in graphene, respectively. We can repeat the exactly same gap extraction process but using $E_{F,mg}$ instead at 0 T.

The electrostatic model can be applied to extract the gap size at 0 T, illustrated in

the right schematic in Fig. 4.9. The displacement can control the the relative position between graphene and WTe_2 bands. Therefore, for a fixed n_g, the D difference at the WTe_2 band edges can provide the information about the WTe_2 gap. Figure. 4.9b shows the schematics of band alignment in the entire hybrid structure. It is worth noting that only the electric field across WTe_2 (E_W) can affect the relative shift between its and graphene bands. Therefore, the gap size can be determined to be E_W difference multiplied by the spacing between WTe_2 and graphene d_{w-g}. However, the derivation of E_W is not straightforward since the voltage drop across WTe_2 is not clear. Fortunately, by Gauss's law we know $n_g = \frac{\left(\varepsilon_{r,W}\varepsilon_0 E_W - \varepsilon_{r,BN}\varepsilon_0 E_{bBN}\right)}{e}$, where ϵ_0 is vacuum permittivity, $\epsilon_{r,W(BN)}$ is WTe_2 (BN) dielectric constant, E_{bBN} is the electric field across the bottom BN and e is the electron charge. Therefore, the E_W can be derived by the relation $\frac{\left(en_g + \varepsilon_{r,BN}\varepsilon_0 E_{bBN}\right)}{\varepsilon_{r,W}\varepsilon_0}$. Most parameters are known constants or can be obtained from the experiments, while only two unknown parameters $\epsilon_{r,W}$ and d_{w-g} are present. We will assume $\epsilon_{r,W} = 3$ and d_{w-g}= 0.28 nm for the following analysis.

Discussion

Figure. 4.9c summarizes the extracted WTe_2 gap size as a function of n_g from different methods. The distinct extraction methods at 0 T both give the pronounced concave features of the gap with the maximum appearing at the finite hole doping of graphene. In addition, these gap size seems to be asymmetric to their maximums - the gap size decreases faster on the right side of the peak compared to the gap on the left side. These observations both suggest the origin of the gap change less likely results solely from Coulomb screening effect, which is monotonically associated with n_g.

It's reported that the WTe_2 gap size can potentially be altered by breaking the spin degeneracy in the presence of the electric field [27, 164]. In our hybrid structure, the electric field possibly can separate electron and hole carriers into graphene and WTe_2 to break the original pairing. Both mechanisms indicate that the electric field leads to the modification of WTe_2 gap size. In order to examine the electric field effect on the gap

magnitude, we use the relation of E_W introduced early to identity the $E_W = 0$ region in Figs. 4.9c denoted by green region. We observe the peaks of the gap appear in the vicinity of the $E_W = 0$ region. Although there are two free parameters determining the magnitude of E_W, the $E_W = 0$ region remains the same regardless of different values chosen for the $\epsilon_{r,W}$ and d_{w-g}. (since the condition for $E_W = 0$ is only determined by other known parameters) Our results suggest the electric field plays an role in the WTe_2 gap modification.

Combining the all observations, Coulomb screening and electric field effects together are likely able to change the WTe_2 gap in our hybrid structure. Based on the maximized gap value close to the $E_W = 0$ region, the gap size potentially decreases in the presence of the electric field. Also, according to the asymmetric gap feature with respect to n_g, Coulomb screening effect can have opposite effect on WTe_2 gap compared to the electric field effect - the gap increases when screening is stronger with larger n_g. Our results demonstrate the nontrivial gap nature in WTe_2, and we call for theoretical interpretation to explain the our experimental observation of the gap evolution and the underlying mechanism for the absence of the concave gap feature at the higher fields..

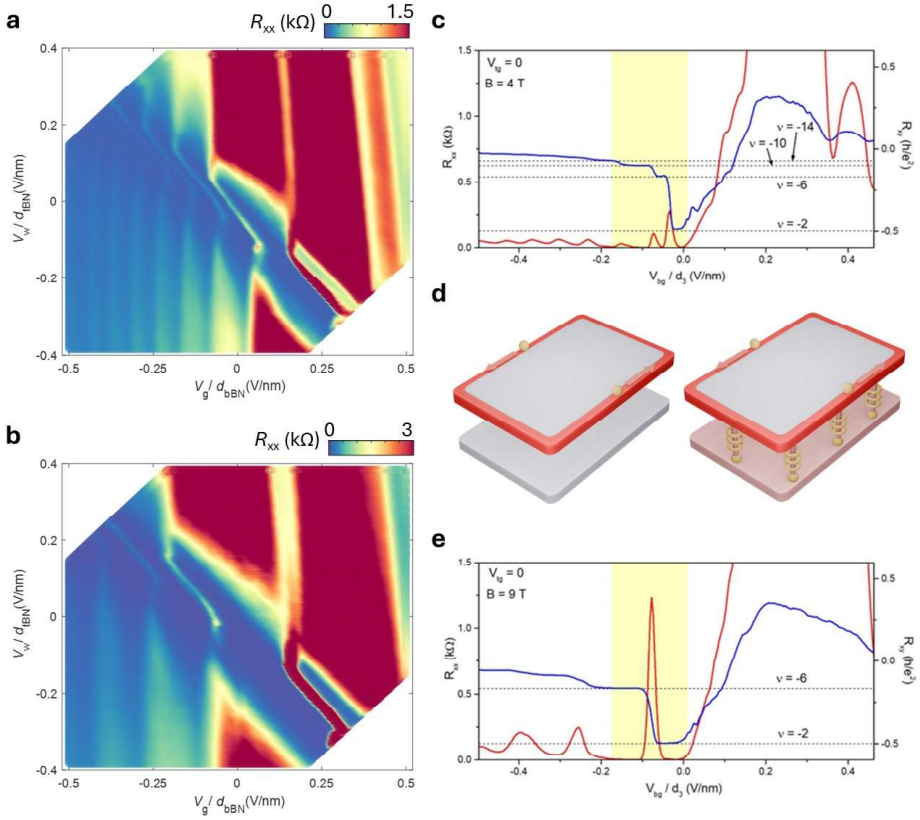

Figure 4.6: **Robust WTe_2 gap region revealed in resistance maps at 4 and 9 T. a-b**, Maps of R_{xx} acquired by sweeping both gates at $B = 4$ T (**a**) and $B = 9$ T (**b**). The zero R_{xx} occurs on the diagonal insulating WTe_2 region. **c,e**, R_{xx} and R_{xy} as a function of V_g with $V_W = 0$ at at $B = 4$ T (**c**) and $B = 9$ T (**e**). The yellow regions denote the WTe_2 gap region, where the well-defined quantum Hall effect in graphene is observed with zero R_{xx} and quantized R_{xy}. From the quantized R_{xy}, the filling factors of $\nu = -2, -6, -10, ...$ are extracted, consistent with the usual sequence of states arising from spin- and valley-degenerate monolayer graphene Landau levels. **d**, Schematic of quantum Hall states in graphene with a insulating and conducting WTe_2. When WTe_2 is insulating, the transport is only dominated by graphene and then exhibits well-defined quantum Hall effect at finite fields. In contrast, when WTe_2 is doped to become conducting, the carrier can interfere with graphene edge states and contribute to transport in parallel, resulting in the deviation from quantum Hall effect.

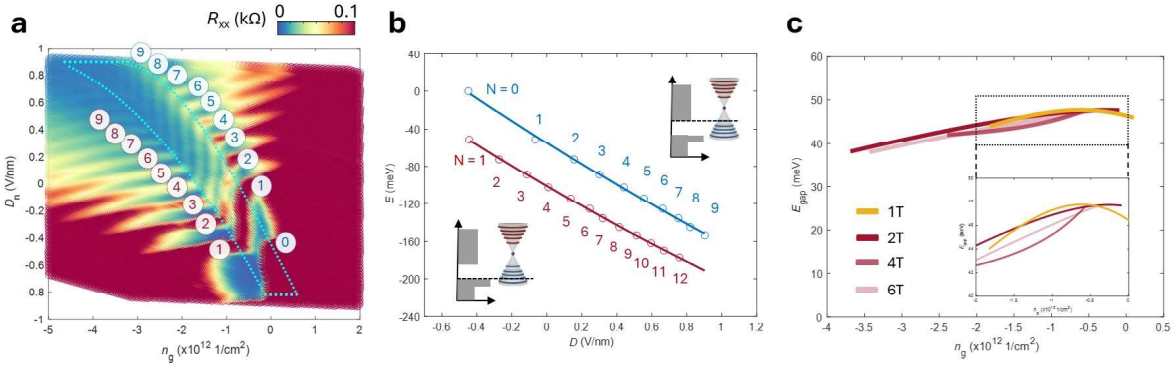

Figure 4.7: **WTe_2 gap extraction from the graphene Landau level cyclotron energy at finite fields.** **a**, Maps of R_{xx} as a function of nominal displacement D_n and graphene density n_g at $B = 2$ T. The D_n and n_g are physically meaningful in graphene within the insulating WTe_2 region enclosed by cyan dashed lines which are defined by the points where the oscillation slope changes. The numbers corresponds to Landau level indices and the red (blue) colors denotes the Landau levels on the dashed line matching the WTe_2 valence (conduction) band edge (**b**). **b**, Graphene Landau level cyclotron energy as a function of D_n from (**a**). The blue (red) points are fitted into a blue (red) polynomial functions. The gap can be extracted by calculating the difference from these two polynomials for a given D_n. **c**, Extracted WTe_2 gap from Landau levels at multiple fields. The extracted gaps are similar at different fields, suggesting the gap doesn't have the obvious dependence on the magnetic field. For most of the range, the gap exhibits the monotonic relation with n_g. However, the gap shows a concave feature in the inset, which proves difficult to explain sole by the screening effect.

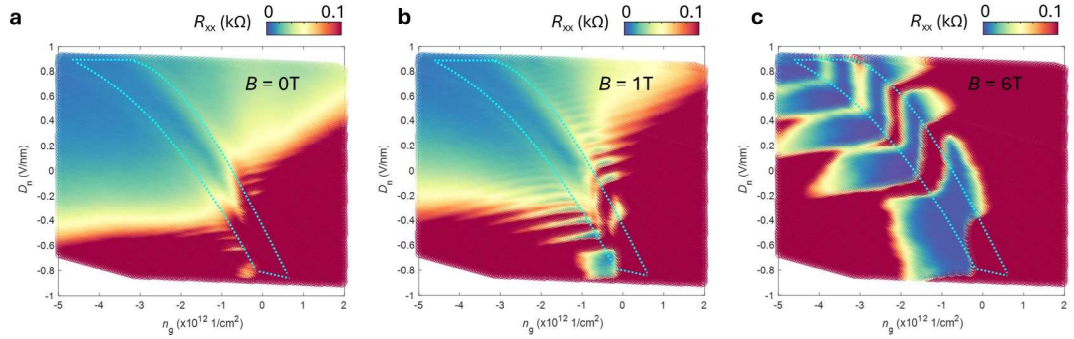

Figure 4.8: **Transport measurements of Device MW2 at multiple fields.** **a-c**, Maps of R_{xx} acquired by sweeping both gates at $B = 0$ T (**a**), $B = 1$ T (**b**) and $B = 6$ T(**c**). Quantum oscillation emerges on the whole map. The trajectories of quantum oscillations is close to be vertical due to the screening effect and the pronounced shift of quantum oscillations along diagonal line is possibly related to the WTe_2 gap. The cyan dashed lines defined from the resistance map at $B = 2$ T indicate the WTe_2 gap region. The WTe_2 gap regions are consistent in the maps at different magnetic fields, implying the gap is not sensitive to the field.

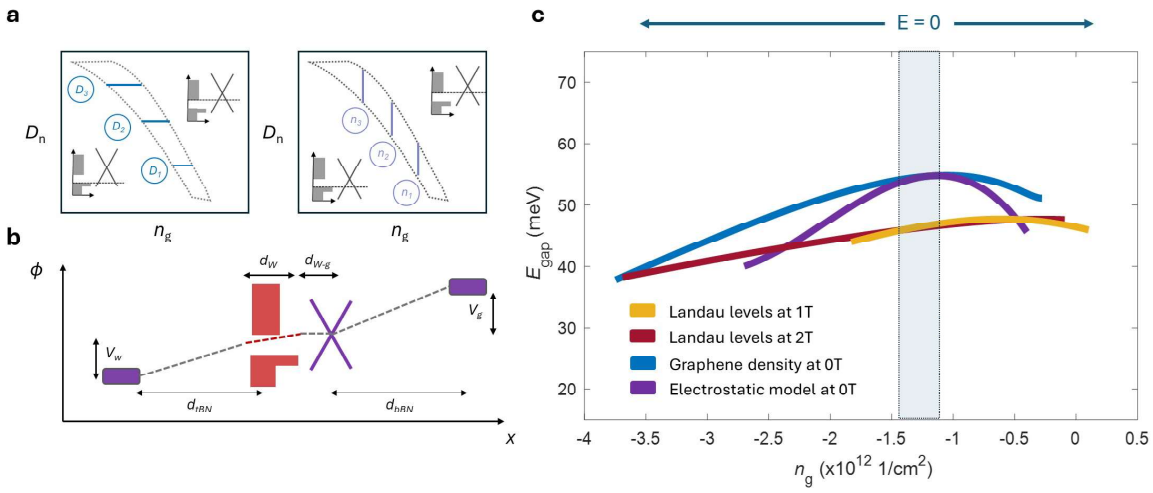

Figure 4.9: **WTe_2 gap extraction at zero field.** **a**, Schematic diagram to illustrate the gap extraction method 1. The WTe_2 insulating region is first defined in Fig. 4.7a and enclosed by the dashed line. The right (left) part of the dashed line correspond to the configuration when the chemical potential touches WTe_2 conduction (valence) band edge. Since the D_n and n_g are physically meaning in graphene within the region, the gap can be extracted by the Fermi energy difference in monolayer graphene at 0 T with different carrier densities for a given D_n. **b**, Schematic diagram to illustrate the gap extraction method 2. For a given n_g, the electric field induced V_g and V_W can move the specific energy level in graphene to pass over the WTe_2 band edges. The difference of induced electric field provides the information about the gap size in WTe_2. **c**, Schematic diagram of the electric potential inside the hybrid structure. **d**, Extracted WTe_2 gap from different extraction methods. The extracted gaps from two distinct methods at 0 T give the pronounced concave feature. Their peaks occur around the zero electric field across WTe_2 with the asymmetric response, suggesting electric field and Coulomb screening might together play a role in controlling the nontrivial gap in WTe_2.

Chapter 5

Investigation of non-magic-angle tBLG

In the chapter 2, the interlayer coupling controlled by the twist angle is capable of engineering the band structure of graphene. When the twist approaches the magic angles, the flat band can be generated accompanied with strong electron interaction to host numerous intriguing phases. For twist angles away from the magic angle, tBLG can exhibit an unanticipated ground state due to the varying degrees of band flattening and electron correlation effects. In this chapter, we investigate the transport properties of two non-magic-angle tBLG devices and report the unexpected AHE signals at half-filling on electron and hole sides.

5.1 Non-magic-angle tBLG

While the magic angle has garnered significant attention due to the discovery of superconductivity and correlated insulating states, exploring other twist angles reveals a broader spectrum of electronic phenomena and phase transitions that are equally intriguing and important for the comprehensive understanding of tBLG's rich electronic properties. The first magic angle is 1.05° and corresponds to the maximized Coulomb interaction, which is usually related to the robust correlated insulating state and super-

conducting state in tBLG [28, 29]. These correlated states emerge at the twist angles ranging from 0.9° to 1.2° approximately [162, 165]. Within this twist angle range, the overall phase diagrams are similar with the different electron interaction strength depending on the twist angle - the farther away from the magic angle, the less electron correlation effect in general.

Previously, the non-magic-angle tBLG is used to study the relation between the correlated states and the superconducting states at half-filling by controlling the Coulomb interaction [162]. It is reported that superconductivity can appear far away from the correlated insulating states, suggesting a 'competing phases' picture where insulators and superconductivity originate from different mechanisms. In addition, combining non-magic-angle tBLG with the WSe_2 can recover the superconducting states in the absence of correlated insulator [45]. Fundamentally, WSe_2 can affect the electronic band structure through modifications of interlayer coupling, induced SOI and renormalization of Fermi velocity, which is potentially essential for stabilizing superconductivity.

Constructing the model describing the electronic bands non-magic-angle tBLG can be challenging due to the several issues, including commensurability, lattice relaxation, twist angle imhomogeneity and strain. Therefore, the more experimental investigation can facilitate theoretical modelling of tBLG phase diagram. In this work, we report the striking observation of AHE signals at half-filling on electron and hole sides in two non-magic-angle tBLG devices, respectively. For MA-tBLG sandwiched by BN flakes, the AHE signals are only observed at odd fillings, where the flat Chern states are first generated by breaking C_2 symmetry and then the spin-valley-polarized ground state gives rise to the magnetism with the finite Berry curvature. Due to the intervalley Hund's coupling, the valley-polarized states are not the ground state at half-filling in general and hence magnetic states are energetically unfavoreds [127, 166, 167]. The magnetic states at half-filling can be stabilized by inducing the SOC to MA-tBLG, where Ising and Rashba SOCs are dominant over the intervalley Hund's coupling to lead to a valley-

polarized ground state. Therefore, investigation of the ground state associated with the magnetism in our non-magic-angle tBLG devices with the weak intrinsic SOC is crucial to understand the tBLG's phase diagram and relation among correlated phases.

5.2 Experimental setup and methods

The tBLG devices were fabricated using the cut-and-stack method, in which exfoliated graphene flakes are isolated using an atomic force microscope tip, and then stacked on top of one another at the desired twist angle. Samples were assembled using standard dry-transfer techniques with a polycarbonate/polydimethyl siloxane stamp. Both tBLG devices are encapsulated in flakes of BN with a graphite bottom gate, and then transferred onto a Si/SiO_2 wafer. Device D2 additionally has a graphite top gate. The temperature was kept below 180 °C during device fabrication to preserve the intended twist angle. Standard electron-beam lithography, CHF_3/O_2 plasma etching, and metal deposition techniques (Cr/Au) were used to define the complete stack into a Hall bar geometry. Device D2 was measured while mounted onto a piezo-based apparatus capable of applying uniaxial strain to the device. All results, here, were acquired without any bias applied to the piezos, which corresponds closely to zero external strain.

5.3 Results on anomalous Hall effect in tBLG

Observation of AHE at half-filling in two tBLG devices

Figures 5.1a-b show Landau fan diagrams for our two devices (D1 with $\theta = 0.96^\circ$ and D2 with $\theta = 1.20^\circ$, respectively). Below each, we plot the device resistivity within the flat band ($-4 \leq \nu \leq +4$) acquired in the absence of a magnetic field and at our nominal base temperature of $T \leq 100$ mK. We observe many features typical of magic-angle tBLG at high field, including a cascade of correlated Chern insulator states and associated

fans of quantum oscillations projecting to various integer ν [28, 29, 30, 31, 168, 124]. However, we do not observe robust zero-field insulating states for any integer ν, most likely indicating that the samples are in a moderately correlated regime.

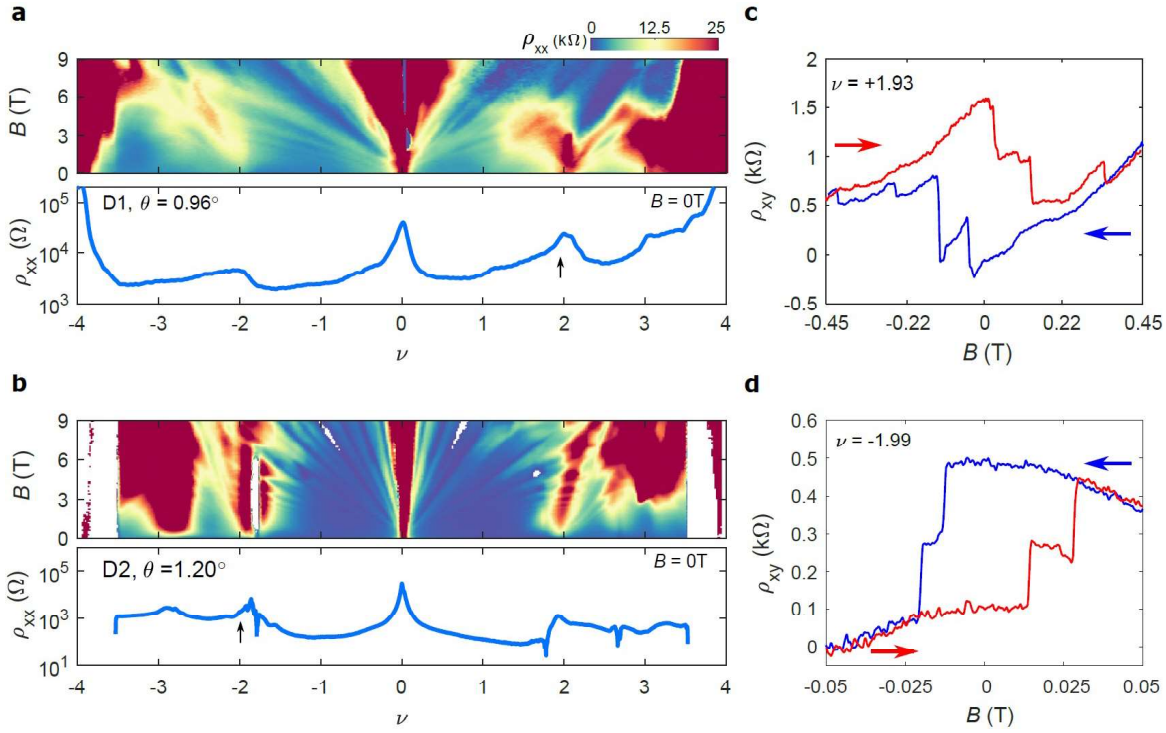

Figure 5.1: **Anomalous Hall effect at half filling in tBLG. a-b**, (top) Landau fan diagram of the longitudinal resistivity, ρ_{xx}, for Device D1 ($\theta = 0.96°$) and D2 ($\theta = 1.20°$), respectively. (bottom) ρ_{xx} measured at $B = 0$. Regions of white in the Landau fan in **(b)** correspond to artifacts of negative measured resistance. Similar artifacts manifest as abrupt dips in ρ_{xx} at $B = 0$. **c**, Hall resistance, ρ_{xy}, in Device D1 measured as the magnetic field is swept back and forth at $\nu = +1.93$ (position of the black arrow in **a**). **d**, Similar measurement of ρ_{xy} in Device D2 at $\nu = -1.99$ (position of the black arrow in **b**). The data for Device D1 (D2) is acquired at a nominal base temperature of 20 (100) mK.

Our primary result is the observation of the AHE within a small region of doping around half filling. Figure 5.1c (d) shows a representative measurement of the Hall resistance, ρ_{xy}, in Device D1 (D2) as the magnetic field, B, is swept back and forth at $\nu = +1.93$ (-1.99). We observe hysteresis and Barkhausen jumps indicating the presence of magnetism in these states. Figure 5.2a shows the temperature dependence of the AHE

in Device D1 at $\nu = +1.93$, acquired by taking the average difference of ρ_{xy} between the two field sweeping directions, $\Delta\rho_{xy}/2 = (\rho_{xy}^{B\downarrow} - \rho_{xy}^{B\uparrow})/2$. Figure 5.2b plots $\Delta\rho_{xy}/2$ at $B = 0$ as a function of temperature. Although the Curie temperature is ~ 5.5 K, the amplitude of the AHE grows slowly as the device is cooled to base temperature, and saturates to a value of less than 1 kΩ. Taken at face value, these observations imply that the ground state at $\nu = +2$ is an ungapped symmetry-broken metal, since the AHE amplitude is far from the quantized value of $h/2e^2$ anticipated at half-filling. However, twist-angle disorder arising due to unintentional strain in the device may instead play a role in obscuring a small intrinsic gap at $\nu = +2$. In either case, our observations sharply contrast the behavior of the trivial correlated insulating states that are conventionally observed in devices closer to the magic angle, which exhibit insulating longitudinal and Hall resistance without associated hysteresis [28, 29, 30, 31].

Figure 5.3a shows a zoomed-in field-symmetrized Landau fan diagram of ρ_{xx} for Device D1. At high field, we observe a fan of two-fold degenerate quantum oscillations that project to $\nu = +2$ at $B = 0$ and disperse towards larger filling factor, away from the charge neutrality point (CNP, $\nu = 0$). These indicate the formation of a new Fermi surface with reduced size compared with the isospin-unpolarized phase nearer the CNP, as has been observed regularly in magic-angle tBLG owing to a doping-dependent symmetry-breaking cascade [168, 124]. Figure 5.3b shows the corresponding field-antisymmetrized measurement of the Hall resistance, ρ_{xy}. At slight underdoping of $\nu = +2$, we see a region in which the Hall effect reverses sign, corresponding to a weakly-developed quantum oscillation with an apparent Chern number of $C = -4$ projecting towards smaller filling factor. This state is eventually interrupted at high field by the formation of a $C = +3$ correlated Chern insulator projecting to $\nu = 1$ at $B = 0$. Figure 5.3c summarizes the most robust gapped states we observe, with trivial insulators denoted in red, correlated Chern insulators in blue, and additional quantum oscillations in gray and green. The ρ_{xy} sign reversal and the associated $C = -4$ state depicted by

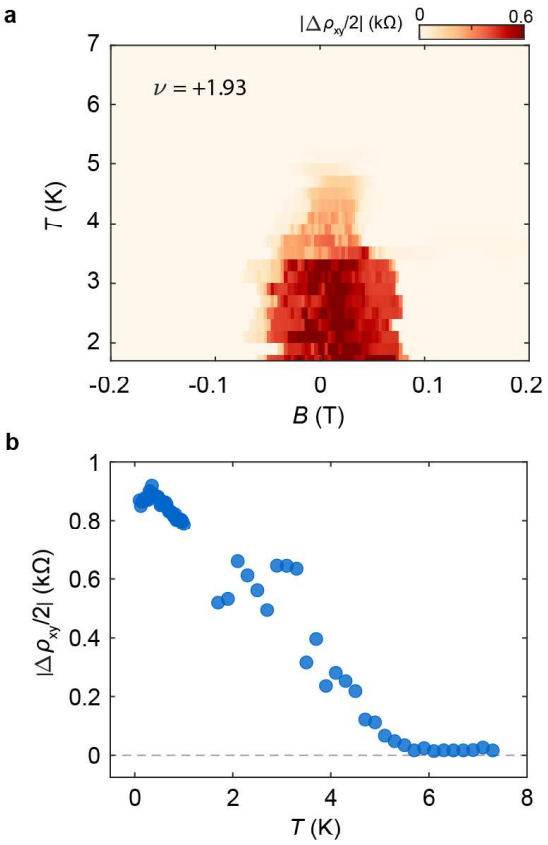

Figure 5.2: **Temperature dependence of the AHE in Device D1. a**, AHE amplitude, $\Delta\rho_{xy}/2 = (\rho_{xy}^{B\downarrow} - \rho_{xy}^{B\uparrow})/2$, measured at $\nu = +1.93$ as B is swept back and forth at various temperatures. **b**, $\Delta\rho_{xy}/2$ at $B = 0$ versus temperature.

the green line in Fig. 5.3c contrast the typical behavior of magic-angle tBLG devices, in which the cascade of symmetry-breaking transitions arise only very near each integer filling and result in fans of quantum oscillations that disperse exclusively towards larger band filling [28, 29, 30, 31]. The precise details of these isospin Stoner transitions depend sensitively on the value of U/W [124], potentially accounting for the difference in the behavior of the quantum oscillations we observe in this device.

Symmetry-breaking and electrical switching of the magnetic state

Although the ρ_{xy} sign reversal persists to $B = 0$, careful measurements of the AHE suggest that its origin is different below and above the coercive field, B_c. For $B > B_c$, the sign change arises owing to the $C = -4$ state discussed earlier. For $B < B_c$, the

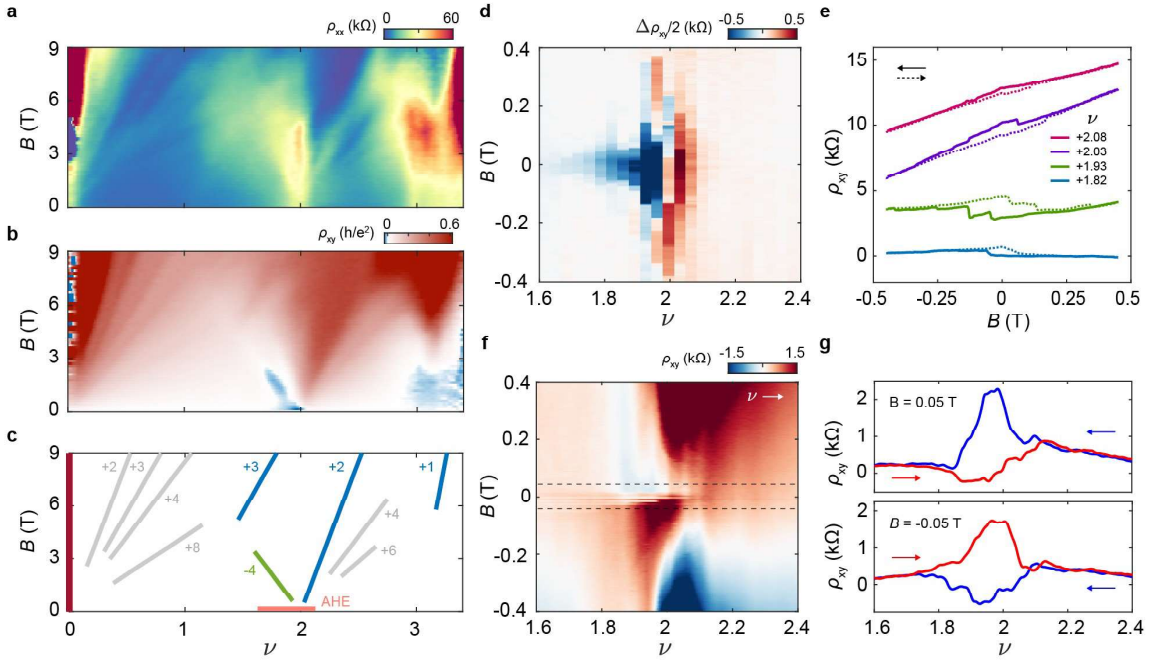

Figure 5.3: **Symmetry-breaking at half filling and electrical switching of the magnetic state.** **a**, Field-symmetrized Landau fan diagram of the longitudinal resistivity, ρ_{xx}, of Device D1. **b**, Field-antisymmetrized Landau fan diagram of the Hall resistance, ρ_{xy}. **c**, Schematic diagram denoting the most robust gapped states observed in the Landau fan. Trivial insulators are denoted in red, correlated Chern insulators in blue, and additional quantum oscillations in gray and green. The horizontal orange line denotes the range of doping over with the AHE is observed. **d**, $\Delta\rho_{xy}/2$ acquired by sweeping B back and forth at fixed ν. **e**, Selected ρ_{xy} traces from (**d**). Curves are offset vertically for clarity. **f**, ρ_{xy} acquired by sweeping ν from small to large values at fixed B. **g**, ρ_{xy} traces at $B = \pm 50$ mT acquired for both sweeping directions of ν, as indicated by the gray dashed lines in (**f**). The data is acquired at $T = 20$ mK in all measurements.

sign change instead arises as a consequence of a reversal of the orbital magnetic state upon doping. We perform two distinct measurements in order to clearly identify the latter effect. First, in Fig. 5.3d we plot $\Delta\rho_{xy}/2$ acquired by sweeping B back and forth at fixed ν, and observe an abrupt sign change precisely at $\nu = +2$. Figure 5.3e shows ρ_{xy} traces at selected values of ν, in which we see that the sense of the AHE flips upon doping across half filling. Second, in Fig. 5.3f we plot ρ_{xy} acquired by sweeping ν from positive to negative at fixed B. Figure 5.3g shows corresponding traces at $B = \pm 50$ mT

acquired for both sweeping directions of ν. For a given sign of B, the magnetic state is determined purely by the gate sweeping direction.

Similar electric-field-reversal effects have been reported previously at $\nu = +1$ and $+3$ in tBLG [169, 170] and at $\nu = +3$ in twisted monolayer-bilayer graphene [169], all of which exhibit a nearly-quantized AHE. Such an effect can arise from the interplay between the bulk orbital magnetic moment and that of the chiral edge mode [171, 169, 170]. If the sign of the magnetization (i.e., the sum of the bulk and edge contributions) changes as the chemical potential crosses integer ν, it can become favorable for the system to undergo a first-order phase transition in which carriers recondense into the opposite valley in order to maintain the alignment of the total magnetization with the external field. Similar effects are also feasible even if the state is not completely gapped, as may be the case in our sample.

Prior measurements of the magnetism underlying the AHE in tBLG indicate that it is driven primarily or exclusively by orbital magnetic moments [172, 173, 170]. Owing to the extraordinarily weak SOC in graphene, the AHE we observe here is almost certainly also driven by orbital magnetism. Consequently, a correlated ground state at half filling with a spontaneous valley polarization is the most natural mechanism consistent with all of our observations described above. Such a state spontaneously breaks time-reversal symmetry, resulting in an AHE due to the large Berry curvature concentrated at the band extrema. Breaking the combined C_2T symmetry (C_2 is a two-fold rotation and T is time reversal) is the most straightforward mechanism for achieving valley imbalance at half filling. In the absence of C_2 symmetry, the tBLG bands acquire a staggered sublattice potential mass that opens a gap at the Dirac point, separating the eight flat bands into two distinct groups of four. Each moiré subband carries a valley Chern number of either $+1$ or -1, with subbands in opposite valleys carrying opposite signs of the valley Chern number owing to their time-reversed relationship [63, 64]. Both of our devices exhibit a base temperature resistivity above 25 kΩ, nearly an order of magnitude

larger than typical tBLG devices [28, 29, 30, 31], likely indicating weak C_2-symmetry breaking from close (but not exact) rotational alignment with the encapsulating boron nitride.

Possible alignment with the encapsulating boron nitride

In principle, C_2-symmetry can break spontaneously, however it is typically observed when the tBLG is within a few degrees of rotational alignment with one of the encapsulating boron nitride (BN) crystals. A large AHE approaching quantization to h/e^2 was observed at $\nu = +3$ in previous tBLG devices with BN misalignment of less than 1°, most simply understood as arising from a complete spin and valley polarization [32, 33]. Our observations contrast these results, however, as we instead observe a metallic AHE only at $\nu = +2$ or -2.

Although we do not have a direct measure of the twist angle of either encapsulating BN crystal with the tBLG, we do not observe any signatures of additional superlattice minibands indicative of near-0° alignment. Nevertheless, we do see an unusually large CNP resistivity in our devices (shown in Figs. 1a-b and Figure 5.4), as well as a weak thermal activation behavior in Device D1 (we did not measure this carefully in Device D2). Additionally, careful inspection of the crystalline edges of the graphene and BN flakes provides additional evidence of their close angular alignment in Figure 5.5. Previous measurements of BN-encapsulated monolayer graphene have revealed the formation of meV-scale gaps at the graphene CNP even in devices in which the rotational misalignment of the BN approaches 5° [60] — well beyond the ability to reach full filling of the resulting moiré miniband with gating. We therefore speculate that both of our devices are likely somewhat (but not precisely) aligned to at least one of the encapsulating BN crystals, providing a natural mechanism for C_2-symmetry breaking. The orbital magnetism may depend sensitively on the precise alignment and near commensurabilities of the twisted graphene and graphene/BN moiré superlattices [174, 175], and the local fluctuations of the atomic registries may provide an additional source of magnetic

disorder in the form of a rapid spatial fluctuation in the sign of the local mass gap [170].

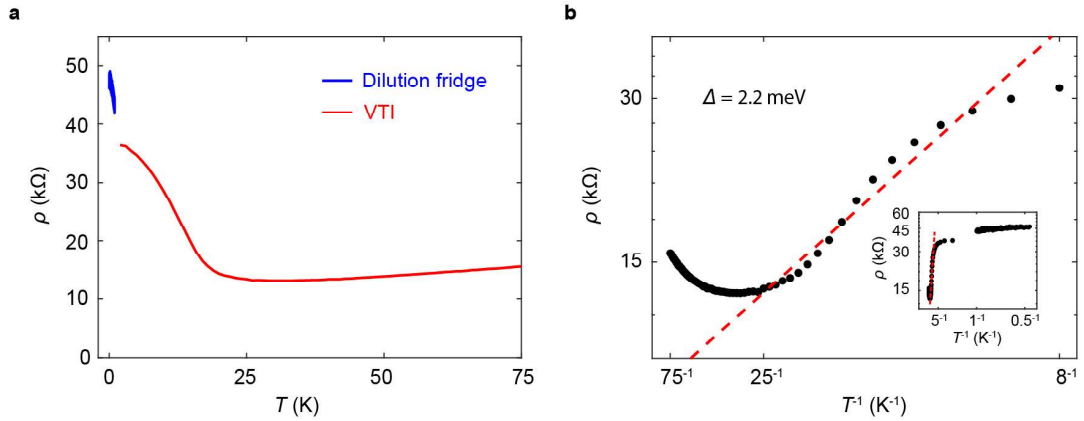

Figure 5.4: **Thermal activation of the CNP in Device D1. a**, Resistivity of Device D1 at the CNP ($\nu = 0$) measured as a function of temperature, exhibiting insulating behavior below approximately 25 K. The red curve is measured in a VTI down to 1.5 K, and the blue curve is measured in a dilution fridge down to 20 mK. **b**, The same data shown on an Arrhenius plot. The CNP exhibits a small region of (approximately) activated behavior. We extract the band gap, $\Delta = 2.2$ meV, from the slope of the linear fit (red dashed line) using $\rho \propto e^{\frac{\Delta}{2kT}}$, where k is the Boltzmann constant.

Candidate ground states

At $\nu = -2$ $(+2)$, two of the eight moiré subbands are (un-)occupied. In this case, there are a handful of nearly degenerate ground states predicted by Hartree-Fock calculations in the absence of C_2 symmetry, including: (i) a valley-polarized, spin-unpolarized quantum anomalous Hall (VP-QAH) state in which both (un-)occupied bands have the same valley index but are spin unpolarized (illustrated schematically at $\nu = +2$ in Fig. 5.6a), (ii) a spin-polarized, valley-unpolarized state in which both (un-)occupied bands have the same spin index but are valley unpolarized, (iii) a valley Hall (VH) state in which the two (un-)occupied bands carry both opposite spin and valley index, and (iv) a sublattice-valley-locked state in which the two (un-)occupied bands carry both opposite sublattice and valley index. Although a disordered and/or small-gap $C = 2$ VP-QAH state is consistent with our observation of a metallic AHE, it is energetically disfavored compared with the VH state due to an intervalley Hund's coupling [62, 176, 167, 177].

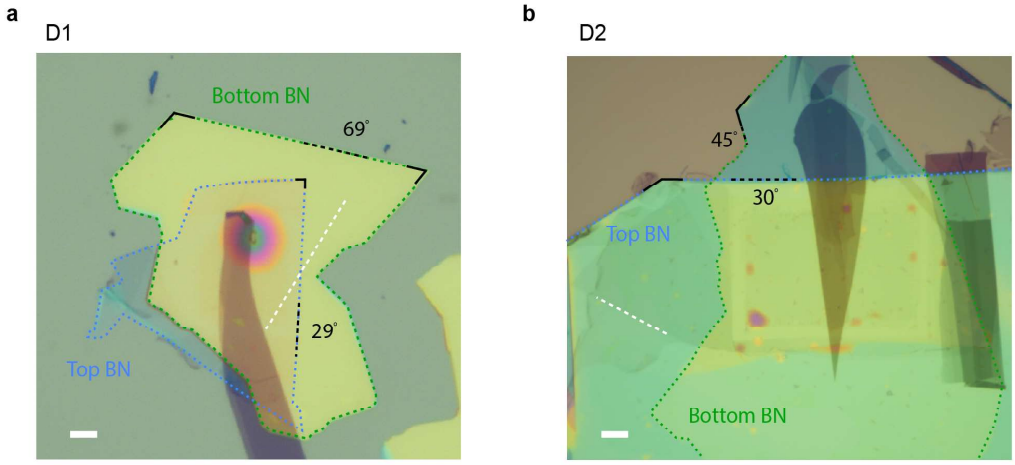

Figure 5.5: **Possible alignment of tBLG and BN.** Optical micrographs of the completed heterostructures of **a**, Device D1 and **b**, Device D2 prior to device fabrication. The top and bottom BN flakes are outlined in green and blue dashed lines, respectively. Angular alignment between the tBLG and BN is estimated by comparing the orientation of the straight crystallographic edges of each. A representative graphene edge is denoted by the white dashed line, and the angular offset with a selected BN edge is denoted next to the corresponding black dashed lines. A few selected BN corners with modulo-30 angles are denoted by the solid black lines, establishing that these are likely zigzag or armchair edges. In both devices, the top BN and tBLG appear to have a $29 - 30°$ angular offset. This indicates a high likelihood of few-degree or smaller alignment of the graphene and top BN crystals, although there is inherent uncertainty in identifying perfect crystalline edges of graphene. The scale bars are 5 µm.

The sublattice-valley-locked state also supports the AHE, however, there has been no specific prediction of this state for physically reasonable tBLG parameters. Although these and other ordered states closely compete, with the ground state ultimately determined by the magnitudes of various small anisotropies that are not precisely known, it is at present not clear what specific conditions would result in the selection of a ground state supporting the AHE as we observe experimentally.

Correlated ground states beyond those considered above have also been identified in Hartree-Fock calculations upon reducing U/W in tBLG with broken C_2 symmetry. For instance, Ref. [64] finds a first-order phase transition to a partially valley-polarized (PVP) state below a critical value of U/W, in which all of the isospin subbands are par-

tially occupied but are filled unevenly owing to a Stoner transition (illustrated schematically at $\nu = +2$ in Fig. 5.6b). The PVP state is inherently metallic, but supports a finite orbital magnetic moment due to the spontaneous imbalancing of the valley occupation. However, there are also competing partial VH and partially spin-polarized states that do not support the AHE, and it is not currently clear which ground state should be favored. Understanding our unexpected observation of the AHE at half filling thus requires a more rigorous theoretical treatment of tBLG, very likely taking into account the role of the increased band dispersion away from the magic-angle (i.e., towards the intermediately-coupled regime) and symmetry-breaking substrate potential terms from the encapsulating BN.

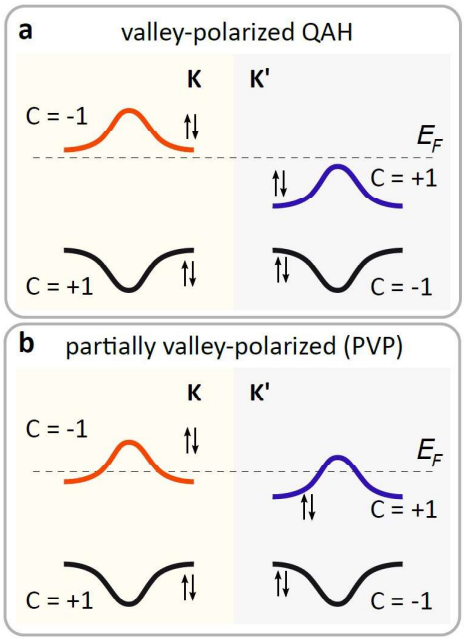

Figure 5.6: **Schematic illustration of candidate ground states with AHE at half filling.** **a**, The valley-polarized QAH state at $\nu = +2$ has two unoccupied bands from the same valley (depicted as valley K here). The state is gapped with a Chern number of +2. **b**, The partially valley-polarized (PVP) state is ungapped at half filling, but features an imbalanced occupation of the moiré valley subbands. Although there is no quantized Chern number describing the state, there is an overall net Berry curvature that supports a metallic AHE.

Discussion

Finally, we discuss some of the implications of our findings in the context of other recent observations in tBLG. The AHE has been reported at $\nu = +2$ in a magic-angle tBLG device assembled on a monolayer of WSe_2 [177]. However, in this case the proximity-induced SOC in the tBLG couples the spin and valley degrees of freedom, and a generalized Hund's term explicitly favors the VP-QAH state at $\nu = 2$. A separate report of a gate-tunable Josephson junction tBLG device (without WSe_2) revealed evidence for some form of magnetic ordering at $\nu = -2$ [178]. However, the AHE was not reported, and the usual trivial correlated insulator was observed instead. The origin and nature of the magnetic order underlying the AHE in our devices is therefore likely to be different from these prior reports in tBLG. Orbital magnetism has been observed at $\nu = -2$ in a magic-angle tBLG device with strong dielectric screening of the Coulomb interactions, and may be of similar nature to that found here, but required the assistance of a perpendicular magnetic field to emerge over a competing zero-field ground state [179]. Lastly, we note that we do not observe any signatures of superconductivity in our devices (shown in Figs. 5.1a-b), despite it having been seen previously in devices with similar twist angles [180, 162, 165]. Although it is impossible to rule out moiré disorder as the cause of its absence, a more likely possibility is that the valley-imbalanced ground state order we observe at half filling is incompatible with pairing. Our results highlight the need for further measurements of devices slightly away from the magic angle to help disentangle the potential interplay of various forms of symmetry-breaking and superconductivity.

tBLG devices with similar twist angles to those we study here have previously been found to exhibit superconducting states surround half filling at low temperature [180, 162, 165]. In contrast, our devices do not exhibit any obviously signatures of superconductivity. Most notably, the device resistivity surrounding half filling at base temperature is typically is on the order of kiloohms (see the bottom panels of Figs.5-1a-b). We cannot rule out trivial explanations, including critical temperatures much lower than our base temperature, or the complete suppression of superconductivity due

to severe local structural inhomogeneities in the sample. However, the proximity to the putative valley-polarized states at half-filling motivates a more substantive explanation for its absence. Cooper pairs typically form with zero center of mass momentum, and as a consequence electrons in tBLG are most likely to form intervalley pairs. Partial or full lifting of the valley degeneracy therefore disfavors superconductivity, as the center of mass momentum of the Cooper pairs becomes nonzero for weak valley polarization, and saturates to values of approximately the momentum of the K/K' corners of the graphene Brillouin zone when valley is fully polarized (intravalley Cooper pairing becomes necessary in this limit). Although circumstantial, our observations are consistent with the anticipated antagonistic relationship between the AHE at half filling and superconductivity at nearby doping. Although superconductivity and the AHE have been previously reported at disjoint band fillings in a single tBLG device [181], so far they have never been seen proximate to one another.

Chapter 6

Future outlook

This thesis characterizes three distinct graphene-based heterostructures and reveals atypical transport features of graphene under the influence of an adjacent material, including CrX_3, WTe_2 and the second graphene with a small twist. In Chapter 3, we observe the charger transfer happening between graphene and CrX_3 due to the work function mismatch. Charges populating into CrX_3 contribute to a variety of unusual characteristics, such as wide IQH plateaus, the negative compressibility and magnetic-field-dependent doping modulation in graphene. However, we are unable to detect sufficiently large exchange field or exchange coupling in our graphene-CrX_3 devices as predicted, which can be associated with disorder in the CrX_3. In chapter 4, the similar charger transfer process occurs in graphene-WTe_2 hybrid structure as well and gate screening effect originating from the carriers residing in WTe_2 resemble what we see in graphene-CrX_3 devices. Well-defined graphene IQH states can be realized in the presence of the insulating WTe_2 and hence we can use the Landau level cyclotron energy to study the gap in WTe_2. Furthermore, we employ different approaches the extract the WTe_2 gap size independently and investigate its nontrivial nature under the effects of the magnetic field, electric field and Coulomb screening. In chapter 5, we report unanticipated AHE signals at half-filling in two non-magic-angle tBLG device. We examine the AHE prop-

erties and symmetry breaking at half-filling, and then discuss the potential ground state candidates. We suggest that two factors—the increased band dispersion and substrate potentials—probably play critical roles in stabilizing a valley-polarized ground state at half-filling.

Below provides several future directions for studying the intriguing characteristics in graphene-based heterostructures through the proximity effects or twist engineering.

Examination of the properties of graphene in contact with other vdW magnets

In chapter 3, we have introduced the our AFM lithography approach to prevent the degradation of air-sensitive CrX_3 during the fabrication. However, the modest mobility of graphene is characterized to be ~ 5000 cm^2/Vs, which is likely associated with defects in the magnets. Hence, this disorder effect can lead to the reduction in the strength of proximity-induced exchange coupling in the graphene. One goal is to grow the bulk crystal with the better quality and re-examine the proximity effects in graphene-CrX_3 heterostructures. In addition, the exploration of other vdW magnets is crucial to the study on the proximity effects for providing more possibilities of inducing stronger couplings and various magnetic ordering, and searching for the air-stable magnet particularly can largely simplify the whole fabrication for future study or application [53, 55].

Hydrostatic pressure study on enhanced magnetic proximity effects

Hydrostatic pressure is a well-known tuning knob to reduce the layer spacing and further enhance the interlayer coupling in a heterostructure. Hence, applying the vertical pressure to graphene-magnet structures in principle is able to amplify the magnetic proximity effects. It has been shown by DFT calculation [117, 116] that the exchange splitting in graphene-CrX_3 structures becomes greatly enlarged as the interlayer spacing decreases, and the splitting of 150 meV can be achieved when the spacing is reduced by 1 Å. In such a compressed structure, the stronger exchange coupling in combination with Rashba splitting leads to topologically nontrivial gap with Chern number $C = 2$

around the K and K points. This topological gap size is predicted to be larger than 10 meV, contributing to QAHE above 100 K much higher than other QAHE systems. Therefore, it will be intriguing to investigate the compressed graphene-CrX_3 structures under the pressure and examine the properties.

Study on the nontrivial WTe_2 gap by the chemical potential measurement

In chapter 4, we have shown that the WTe_2 gap is potentially modified by the electric field and the Coulomb screening effects. Having another independent method to directly probe the chemical potential and gap size in the graphene-WTe_2 system can validate our methods and benefit our understanding of WTe_2. Adding a monolayer graphene sensor to the structure is a common approach to measure the chemical potential of the target system. Previously, this method has been employed to study the correlated gap at CNP of a pure monolayer WTe_2 [26] and the flavour symmetry breaking at integer fillings of tBLG [121]. In a graphene sensor device, the quantitative gap evolution with respect to the electric field and the Coulomb screening can be obtained to further study the intricate gap nature of WTe_2. In addition, the negative compressibility possibly emerges in graphene-WTe_2 structure arising from the strong electron correlation [121, 36, 107] and the overlapping bands [144] of graphene and WTe_2. This characteristic can be explicitly probed by the chemical potential measurement.

SOC proximity effects in graphene interfaced with WTe_2

WTe_2 features strong SOC and hence is able to introduce exotic phenomena in graphene via the proximity effects in a hybrid structure. Weak (anti-)localization signatures needs to be investigated to estimate the SOC magnitude [93, 94]. In addition, charge-to-spin conversion experiments performed by transport [96] and MOKE [182] measurements or anisotropic spin relaxation experiment [101, 102] are able to further reveal the nature of SOC. Moreover, introduction of SOC into graphene can give rise to inverted band structure [42] and potential topological states [90]. These features should be also carefully examined in the future work.

Magnetic proximity effects in tBLG interfaced with vdW magnets

The topology and ground states at each filling in tBLG have been extensively studied to understand the mechanism for the emergent correlated states [62, 63, 64, 125, 126, 120, 127], including the unconventional superconductivity and Chern insulating states. A new ground state can emerge in tBLG under the influence of an adjacent material. For example, breaking the C_2 symmetry by the BN substrate potential [33, 32] or inducing SOC from a TMD [45] in tBLG has been reported to host QAHE and stabilize the superconductivity, respectively. However, so far no one has reported the properties of tBLG in contact with a vdW magnet to examine the magnetic proximity effects, likely due to the air-sensitive feature of most vdW magnet and the negligible induced exchange coupling to graphene as discussed in chapter 3. Studying tBLG-vdW magnet structures offers several important advantages. The proximitized exchange coupling can induce the long-range magnetic ordering in graphene and break the time-reversal symmetry, opening the gaps and generating the flat topological bands in the moiré Brillouin zone where the mini conduction (valence) bands carry the same Chern number at K and K' points. Therefore, the QAHE states are expected to be realized at each filling in tBLG-vdW structures instead of the only odd filling seen in tBLG under C_2 symmetry breaking [33, 32]. In addition, introducing the magnetism can modify the ground state and an important question is how the unconventional superconductivity in tBLG evolves with respect to the emergence of magnetism and new ground states accordingly. Investigation of this structure is able to further unveil the nature of superconductivity and the phase diagram in tBLG.

References

[1] K. S. Novoselov, A. K. Geim, S. V. Morozov, D. Jiang, S. V. Dubonos, and *et al.* Electric field effect in atomically thin carbon films. *Science*, 206:666–669, 2004.

[2] C. Lee and *et al.* Measurement of the elastic properties and intrinsic strength of monolayer graphene. *Science*, 321:385–388, 2008.

[3] W. Cai and *et al.* Thermal transport in suspended and supported monolayer graphene grown by chemical vapor deposition. *Nano Letters*, 10:1645–1651, 2010.

[4] A. K. Geim and K. S. Novoselov. The rise of graphene. *Nature Materials*, 6:183–191, 2007.

[5] Y. Zhang, Y.-W. Yan, H. Stormer, and P. Kim. Unconventional quantum hall effect and berry's phase of 2 in bilayer graphene. *Nature*, 438:201–204, 2005.

[6] K. S. Novoselov, E. McCann, S. Morozov, V. I. Fal'ko, M. I. Katsnelson, and *et al.* Unconventional quantum hall effect and berry's phase of 2 in bilayer graphene. *Nature Physics*, 2:177–180, 2006.

[7] A. Young and P. Kim. Quantum interference and klein tunnelling in graphene heterojunctions. *Nature Physics*, 5:222–226, 2009.

[8] C. R. Dean, A. F. Young, I. Meric, C. Lee, L. Wang, S. Sorgenfrei, K. Watanabe, T. Taniguchi, P. Kim, K. L. Shepard, and J. Hone. Boron nitride substrates for high-quality graphene electronics. *Nature Nanotechnology*, 5:722–726, 2010.

[9] A. Splendiani, L. Sun, Y. Zhang, J. Li, T. Kim, and *et al.* Emerging photoluminescence in monolayer mos2. *Nano Letters*, 10:1271–1275, 2010.

[10] K. Mak, C. Lee, J. Hone, J. Shan, and T. Heinz. Atomically thin mos2: A new direct-gap semiconductor. *Physical Review Letters*, 105:136805, 2010.

[11] D. Xiao, G.-B. Liu, W. Feng, X. Xu, and W. Yao. Coupled spin and valley physics in monolayers of mos2 and other group-vi dichalcogenides. *Physical Review Letters*, 108:196802, 2012.

[12] E. Sajadi, T. Palomak, Z. Fei, W. Zhao, P. Bement, C. Olsen, S. Luescher, X. Xu, J. Folk, and D. Cobden. Gate-induced superconductivity in a monolayer topological insulator. *Science*, 362:922–925, 2018.

[13] Z. Fei, T. Palomaki, S. Wu, W. Zhao, X. Cai, B. Sun, Nguyen. P., J. Finney, X. Xu, and D. Cobden. Edge conduction in monolayer wte2. *Nature Physics*, 13:677–682, 2017.

[14] S. Wu, V. Fatemi, Q. Gibson, K. Watanabe, T. Taniguchi, R. Cava, and P. Jarillo-Herrero. Observation of the quantum spin hall effect up to 100 kelvin in a monolayer crystal. *Science*, 359:76–79, 2018.

[15] Y. Shi, J. Kahn, B. Niu, Z. Fei, B. Sun, X. Cai, B. Franscisco, Di Wu, Z. Shen, X. Xu, D. Cobden, and Y. Cui. Imaging quantum spin hall edges in monolayer wte2. *Science Advances*, 5:eaat8799, 2019.

[16] Z. Fei, W. Zhao, T. Palomaki, B. Sun, M. Miller, and *et al.* Ferroelectric switching of a two-dimensional metal. *Nature*, 560:336–339, 2018.

[17] B. Huang, G. Clark, E. Navarro-Moratalla, D. Klein, R. Cheng, and *et al.* Layer-dependent ferromagnetism in a van der waals crystal down to the monolayer limit. *Nature*, 546:270–273, 2017.

[18] C. Gong, L. Li, Z. Li, H. Ji, A. Stern, and *et al.* Discovery of intrinsic ferromagnetism in two-dimensional van der waals crystals. *Nature*, 546:265–269, 2017.

[19] T. Huang, L. Zhang, and T. Ma. Antiferromagnetically ordered mott insulator and $d+id$ superconductivity in twisted bilayer graphene: A quantum monte carlo study. *arXiv:1804.06096*, 2018.

[20] S. Jiang, L. Li, Z. Wang, K. Mak, and J. Shan. Controlling magnetism in 2d cri3 by electrostatic doping. *Nature Nanotechnology*, 13:549–553, 2018.

[21] T. Song, X. Cai, M. W.-Y. Tu, X. Zhang, B. Huang, N. P. Wilson, K. L. Seyler, L. Zhu, T. Taniguchi, K. Watanabe, M. A. McGuire, D. H. Cobden, D. Xiao, W. Yao, and X. Xu. Giant tunneling magnetoresistancein spin-filter van der Waals heterostructures. *Science*, 360:1214–1218, 2018.

[22] L. Wang, I. Meric, P. Y. Huang, Q. Gao, Y. Gao, H. Tran, T. Taniguchi, K. Watanabe, L. M. Campos, D. A. Muller, J. Guo, P. Kim, J. Hone, K. L. Shepard, and C. R. Dean. One-dimensional electrical contact to a two-dimensional material. *Science*, 342:614–617, 2013.

[23] C. R. Dean, L. Wang, P. Maher, C. Forsythe, F. Ghahari, Y. Gao, J. Katoch, M. Ishigami, P. Moon, M. Koshino, T. Taniguchi, K. Watanabe, K. L. Shepard, J. Hone, and P. Kim. Hofstadter's butterfly and the fractal quantum hall effect in moire superlattices. *Nature*, 497:598–602, 2013.

[24] S. Tang, C. Zhang, D. Wong, Z. Pegramrazi, H.-Z. Tsai, and *et al.* Quantum spin hall state in monolayer 1t'-wte2. *Nature Physics*, 13:683–687, 2017.

[25] T. Song, Y. Jia, G. Yu, Y. Tang, P. Wang, R. Singha, X. Gui, A. Uzan-Narovlansky, M Onyszczak, K. Watanabe, T. Taniguchi, R. Cava, L. Schoop, N. P. Ong, and S. Wu. Unconventional superconducting quantum criticality in monolayer wte2. *Nature Physics*, 20:269–274, 2024.

[26] B. Sun, W. Zhao, T. Palomaki, Z. Fei, E. Runburg, and *et al.* Evidence for equilibrium exciton condensation in monolayer wte2. *Nature Physics*, 18:94–99, 2022.

[27] Y. Jia, P. Wang, C.-L. Chiu, Song Z., Guo Yu, and *et al.* Evidence for a monolayer excitonic insulator. *Nature Physics*, 18:87–93, 2022.

[28] Y. Cao, V. Fatemi, A. Demir, S. Fang, S. L. Tomarken, J. Y. Luo, J. D. Sanchez-Yamagishi, K. Watanabe, T. Taniguchi, E. Kaxiras, R. C. Ashoori, and P. Jarillo-Herrero. Correlated insulator behaviour at half-filling in magic-angle graphene superlattices. *Nature*, 556:80–84, 2018.

[29] Y. Cao, V. Fatemi, S. Fang, K. Watanabe, T. Taniguchi, E. Kaxiras, and P. Jarillo-Herrero. Unconventional superconductivity in magic-angle graphene superlattices. *Nature*, 556:43–50, 2018.

[30] M. Yankowitz, S. Chen, H. Polshyn, Y. Zhang, K. Watanabe, T. Taniguchi, D. Graf, A. F. Young, and C. R. Dean. Tuning superconductivity in twisted bilayer graphene. *Science*, 363:1059–1064, 2019.

[31] X. Lu, P. Stepanov, W. Yang, M. Xie, M. A. Aamir, I. Das, C. Urgell, K. Watanabe, T. Taniguchi, G. Zhang, A. Bachtold, A. H. MacDonald, and D. K. Efetov. Superconductors, orbital magnets, and correlated states in magic angle bilayer graphene. *Nature*, 574:653–657, 2019.

[32] A. L. Sharpe, E. J. Fox, A. W. Barnard, J. Finney, K. Watanabe, T. Taniguchi, M. A. Kastner, and D. Goldhaber-Gordon. Emergent ferromagnetism near three-quarters filling in twisted bilayer graphene. *Science*, 365:605–608, 2019.

[33] M. Serlin, C. L. Tschirhart, H. Polshyn, Y. Zhang, J. Zhu, K. Watanabe, T. Taniguchi, L. Balents, and A. F. Young. Intrinsic quantized anomalous hall effect in a moiré heterostructure. *Science*, 367:900–903, 2020.

[34] L. Balents, C. R Dean, D. K. Efetov, and A. F. Young. Superconductivity and strong correlations in moiré flat bands. *Nature Physics*, 16:725–733, 2020.

[35] E. Y. Andrei and A. H. MacDonald. Graphene bilayers with a twist. *Nature Materials*, 19:1265–1275, 2020.

[36] H. Zhou, T. Xie, A. Ghazaryan, T. Holder, J. Ehrets, and *et al.* Half- and quarter-metals in rhombohedral trilayer graphene. *Science*, 598:429–433, 2021.

[37] T. Han, Z. Lu, G. Scuri, J. Sung, J. Wang, and *et al.* Correlated insulator and chern insulators in pentalayer rhombohedral-stacked graphene. *Nature Nanotechnology*, 19:181–187, 2024.

[38] K. Liu, J. Zheng, Y. Sha, B. Lyu, F. Li, and *et al.* Spontaneous broken-symmetry insulator and metals in tetralayer rhombohedral graphene. *Nature Nanotechnology*, 19:188–195, 2024.

[39] T. Li, S. Jiang, B. Shen, Y. Zhang, Li. L., and *et al.* Quantum anomalous hall effect from intertwined moiré bands. *Nature*, 600:641–646, 2021.

[40] J. Cai, E. Anderson, C. Wang, X. Zhang, X. Liu, and *et al.* Signatures of fractional quantum anomalous hall states in twisted mote2. *Nature*, 622:63–68, 2023.

[41] H. Park, J. Cai, E. Anderson, Y. Zhang, J. Zhu, and *et al.* Observation of fractionally quantized anomalous hall effect. *Nature*, 622:74–79, 2023.

[42] J. O. Island, X. Cui, C. Lewandowski, J. Y. Khoo, E. M. Spanton, H. Zhou, D. Rhodes, J. C. Hone, T. Taniguchi, K. Watanabe, L. S. Levitov, M. P. Zaletel, and A. F. Young. Spin-–orbit-driven band inversion in bilayer graphene by the van der waals proximity effect. *Nature*, 571:85–89, 2019.

[43] Y. Zhang, R. Polski, A. Thomson, E. Lantagne-Hurtubise, C. Lewandowski, and *et al.* Enhanced superconductivity in spin–orbit proximitized bilayer graphene. *Nature*, 613:268–273, 2023.

[44] L Holleis, C. Patterson, Y. Zhang, Y. Vituri, H. Yoo, and *et al.* Nematicity and orbital depairing in superconducting bernal bilayer graphene with strong spin orbit coupling. *arXiv:2303.00742*, 2023.

[45] H. Arora, R. Polski, Y. Zhang, A. Thomson, Y. Choi, and *et al.* Superconductivity in metallic twisted bilayer graphene stabilized by wse2. *Nature*, 583:379–384, 2020.

[46] R. Su, M. Kuiri, K. Watanabe, T. Taniguchi, and J. Folk. Superconductivity in twisted double bilayer graphene stabilized by wse2. *Nature Materials*, 22:1332–1337, 2023.

[47] Z. Wang, C. Tang, R. Sachs, Y. Barlas, and J. Shi. Proximity-induced ferromagnetism in graphene revealed by the anomalous Hall effect. *Physical Review Letters*, 114:016603, 2015.

[48] C. Tang, B. Cheng, M. Aldosary, Z. Wang, Z. Jiang, K. Watanabe, T. Taniguchi, M. Bockrath, and J. Shi. Approaching quantum anomalous Hall effect in proximity-coupled YIG/graphene/h-BN sandwich structure. *APL Materials*, 6:026401, 2018.

[49] P. Wei, S. Lee, F. Lemaitre, L. Pinel, D. Cutaia, W. Cha, F. Katmis, Y. Zhu, D. Heiman, J. Hone, Moodera J. S., and C.-T Chen. Strong interfacial exchange field in the graphene/EuS heterostructure. *Nature Materials*, 15:711–716, 2016.

[50] Y. Wu, H. Song, L. Zhang, X. Yang, Z. Ren, and *et al.* Magnetic proximity effect in graphene coupled to a bifeo3 nanoplate. *Physical Review B*, 95:195426, 2017.

[51] C. Tang, Z. Zhang, S. Lai, Q. Tan, and W.-B. Gao. Magnetic proximity effect in graphene/$CrBr_3$ van der Waals heterostructures. *Advanced Materials*, 32:1908498, 2020.

[52] Y. Wu, Q. Cui, M. Zhu, X. Liu, Y. Wang, and *et al.* Magnetic exchange field modulation of quantum hall ferromagnetism in 2d van der waals crcl3/graphene heterostructures. *ACS Applied Materials Interfaces*, 13:10656–10663, 2021.

[53] T. S. Ghiasi, A. A. Kaverzin, A. H. Dismukes, D. K. de Wal, X. Roy, and B. J. van Wees. Electrical and thermal generation of spin currents by magnetic bilayer graphene. *Nature Nanotechnology*, 16:788–794, 2021.

[54] Y. Wu, G. Yin, L. Pan, A. J. Grutter, Q. Pan, A. Lee, D. A. Gilbert, J. A. Borchers, W. Ratcliff II, A. Li, X.-D. Han, and K. L. Wang. Large exchange splitting in monolayer graphene magnetized by an antiferromagnet. *Nature Electronics*, 3:604–611, 2020.

[55] Y. Wang, X. Gao, K. Yang, P. Gu, B. Dong, Y. Jiang, Watanabe K., T. Taniguchi, J. Kang, W. Lou, J. Mao, Y. Ye, Z. V. Han, K. Chang, J. Zhang, and Z. Zhang. Flavoured quantum hall phase in graphene/CrOCl heterostructures. *arXiv:2110.02899*, arxiv.org/abs/2110.0289:Sept 15, 2022, 2021.

[56] x. Xu, W. Yao, D. Xiao, and T. Heinz. Spin and pseudospins in layered transition metal dichalcogenides. *Nature Physics*, 10:343–350, 2014.

[57] K. L. Zhong, D. Seyler, X. Linpeng, R. Cheng, N. Sivadas, B. Huang, E. Schmidgall, T. Taniguchi, K. Watanabe, M. A. McGuire, W. Yao, D. Xiao, K.-M. C. Fu, and X. Xu. Van der Waals engineering of ferromagnetic semiconductor heterostructures for spin and valleytronics. *Science Advances*, 3:e1603113, 2017.

[58] D. Zhong, K. L. Seyler, X. Linpeng, N. P. Wilson, T. Taniguchi, K. Watanabe, M. A. McGuire, K.-M. C. Fu, D. Xiao, W. Yao, and X. Xu. Layer-resolved magnetic proximity effect in van der Waals heterostructures. *Nature Nanotechnology*, 15:187–191, 2020.

[59] Matthew Yankowitz, Jiamin Xue, Daniel Cormode, Javier D. Sanchez-Yamagishi, K. Watanabe, T. Taniguchi, Pablo Jarillo-Herrero, Philippe Jacquod, and Brian J. LeRoy. Emergence of superlattice dirac points in graphene on hexagonal boron nitride. *Nat. Phys.*, 8:382–386, 2012.

[60] B. Hunt, J. D. Sanchez-Yamagishi, A. F. Young, M. Yankowitz, B. J. LeRoy, K. Watanabe, T. Taniguchi, P. Moon, M. Koshino, P. Jarillo-Herrero, and R. C. Ashoori. Massive dirac fermions and hofstadter butterfly in a van der waals heterostructure. *Science*, 340:1427–1430, 2013.

[61] R. Bistritzer and A. H. MacDonald. Moiré bands in twisted double-layer graphene. *Proceedings of the National Academy of Sciences*, 108:12233–12237, 2011.

[62] Y.-A. Zhang, D. Mao, Y. Cao, P. Jarillo-Herrero, and T. Senthil. Nearly flat chern bands in moiré superlattices. *Physical Review B*, 99:075127, 2019.

[63] Y.-H. Zhang, D. Mao, and T. Senthil. Twisted bilayer graphene aligned with hexagonal boron nitride: Anomalous hall effect and a lattice model. *Physical Review Research*, 1:033126, 2019.

[64] N. Bultinck, S. Chatterjee, and M. P. Zaletel. Mechanism for anomalous hall ferromagnetism in twisted bilayer graphene. *Physical Review Letters*, 124:166601, 2020.

[65] T. Song, Q.-C. Sun, E. Anderson, C. Wang, J. Qian, and *et al.* Direct visualization of magnetic domains and moiré magnetism in twisted 2d magnets. *Science*, 374:1140–1144, 2021.

[66] Y. Xu, A. Ray, Y.-T. Shao, S. Jiang, K. Lee, and *et al.* Coexisting ferromagnetic–antiferromagnetic state in twisted bilayer cri3. *Nature Nanotechnology*, 17:143–147, 2022.

[67] K. L. Seyler, P. Rivera, H. Yu, N. P. Wilson, E. L. Ray, D. G. Mandrus, J. Yan, W. Yao, and X. Xu. Signatures of moiré-trapped valley excitons in $mose_2/wse_2$ heterobilayers. *Nature*, 567:66–70, 2019.

[68] C. Jin, E. C. Regan, A. Yan, M. I. B. Utama, D. Wang, S. Zhao, Y. Qin, S. Yang, Z. Zheng, S. Shi, K. Watanabe, T. Taniguchi, S. Tongay, A. Zettl, and F. Wang. Observation of moiré excitons in wse_2/ws_2 heterostructure superlattices. *Nature*, 567:76–80, 2019.

[69] K. Tran, G. Moody, F. Wu, X. Lu, J. Choi, K. Kim, A. Rai, D. A. Sanchez, J. Quan, A. Singh, J. Embley, A. Zepeda, M. Campbell, T. Autry, T. Taniguchi, K. Watanabe, N. Lu, S. K. Banerjee, K. L. Silverman, S. Kim, E. Tutuc, L. Yang, A. MacDonald, and X. Li. Evidence for moiré excitons in van der waals heterostructures. *Nature*, 567:71–75, 2019.

[70] Y. Xu, S. Liu, D. Rhodes, K. Watanabe, T. Taniguchi, and *et al.* Correlated insulating states at fractional fillings of moiré superlattices. *Nature*, 582:214–218, 2020.

[71] E. C. Regan, D. Wang, C. Jin, M. I. B. Utama, B. Gao, X. Wei, S. Zhao, W. Zhao, K. Yumigeta, M. Blei, J. Carlstroem, K. Watanabe, T. Taniguchi, S. Tongay, M. Crommie, A. Zettl, and F. Wang. Mott and generalized wigner crystal states in wse_2/ws_2 moiré superlattices. *Nature*, 579:359–363, 2020.

[72] X. Huang, T. Wang, S. Miao, C. Wang, Z. Li, and *et al.* Correlated insulating states at fractional fillings of the ws2/wse2 moiré lattice. *Nature Physics*, 17:715–719, 2021.

[73] K. Kang, B. Shen, Y. Qiu, Y. Zeng, Z. Xia, and *et al.* Evidence of the fractional quantum spin hall effect in moiré mote2. *Nature*, 628:522–526, 2024.

[74] K. Kang, Y. Qiu, K. Watanabe, T. Taniguchi, J. Shan, and Mak. K. Observation of the double quantum spin hall phase in moiré wse2. *arXiv:2402.04196*, 2024.

[75] Y. Zeng, Z. Xia, K. Kang, J. Zhu, P. Knüppel, and *et al.* Thermodynamic evidence of fractional chern insulator in moiré mote2. *Nature*, 622:69–73, 2023.

[76] F. Xu, Z. Sun, T. Jia, C. Liu, C. Xu, and *et al.* Observation of integer and fractional quantum anomalous hall effects in twisted bilayer mote2. *Physical Review X*, 13:031037, 2023.

[77] Y. Guo, J. Pack, J. Swann, L. Holtzman, M. Cothrine, and *et al.* Superconductivity in twisted bilayer wse2. *arXiv:2406.03418*, 2024.

[78] Y. Xia, Z. Han, K. Watanabe, T. Taniguchi, J. Shan, and Mak. K. Unconventional superconductivity in twisted bilayer wse2. *arXiv:2405.14784*, 2024.

[79] M. Yankowitz, J. Jung, E. Laksono, N. Leconte, B. L. Chittari, K. Watanabe, T. Taniguchi, S. Adam, D. Graf, and C. R. Dean. Dynamic band-structure tuning of graphene moiré superlattices with pressure. *Nature*, 557:404–408, 2018.

[80] T. Song, Z. Fei, M. Yankowitz, Z. Lin, Q. Jiang, K. Hwangbo, Q. Zhang, B. Sun, T. Taniguchi, K. Watanabe, M. A. McGuire, D. Graf, T. Cao, J.-H. Chu, D. H. Cobden, C. R. Dean, D. Xiao, and X. Xu. Switching 2d magnetic states via pressure tuning of layer stacking. *Nature Materials*, 18:1298–1302, 2019.

[81] T. Li, S. Jiang, H. Sivadas, Z. Wang, Y. Xu, D. Weber, J. E. Goldberger, K. Watanabe, T. Taniguchi, C. J. Finnie, K. F. Mak, and J. Shan. Pressure-controlled interlayer magnetism in atomically thin cri_3. *Nature Materials*, 18:1303–1308, 2019.

[82] J. Chu and *et al.* In-plane resistivity anisotropy in an underdoped iron arsenide superconductor. *Science*, 329:824–826, 2010.

[83] Z. Peng and *et al.* Strain engineering of 2d semiconductors and graphene: from strain fields to band-structure tuning and photonic applications. *Light: Science Applications*, 9:190, 2020.

[84] Y. Qi and *et al.* Recent progress in strain engineering on van der waals 2d materials: Tunable electrical, electrochemical, magnetic, and optical properties. *Advanced Materials*, 35:2205714, 2023.

[85] D. Rizzo, B. Jessen, F. Sun, Z. adn Ruta, J. Zhang, and *et al.* Charge-transfer plasmon polaritons at graphene/-rucl3 interfaces. *Nano Letters*, 20:8438–8445, 2020.

[86] J. Pack, Y. Guo, Z. Liu, B. Jessen, L. Holtzman, and *et al.* Charge-transfer contacts for the measurement of correlated states in high-mobility wse2. *Nature Nanotechnology*, 19:948–954, 2024.

[87] M. Kavitha and M. Jaiswal. Graphene: A review of optical properties and photonic applications. *Asian Journal of Physics*, 25:809–831, 2016.

[88] J Sierra, J. Fabian, and *et al.* Van der waals heterostructures for spintronics and opto-spintronics. *Nature Nanotechnology*, 16:856–868, 2021.

[89] M. Gmitra and *et al.* Trivial and inverted dirac bands and the emergence of quantum spin hall states in graphene on transition-metal dichalcogenides. *Physical Review B*, 93:155104, 2016.

[90] C. Kane and Mele. E. Quantum spin hall effect in graphene. *Physical Review Letters*, 95:226801, 2005.

[91] Wang Z. and *et al.* Strong interface-induced spin–orbit interaction in graphene on ws2. *Nature Communications*, 6:8339, 2015.

[92] B. Yang, M.-F. Tu, J. Kim, Y. Wu, H. Wang, J. Alicea, R. Wu, M. Bockrath, and J. Shi. Tunable spin–orbit coupling and symmetry-protected edge states in graphene/ws2. *2D Materials*, 3:031012, 2016.

[93] Z. Wang and *et al.* Origin and magnitude of 'designer' spin-orbit interaction in graphene on semiconducting transition metal dichalcogenides. *Physical Review X*, 6:041020, 2016.

[94] Völkl. T. and *et al.* Magnetotransport in heterostructures of transition metal dichalcogenides and graphene. *Physical Review B*, 96:125405, 2017.

[95] Z. Zihlmann and *et al.* Large spin relaxation anisotropy and valley-zeeman spin-orbit coupling in wse2/graphene/h-bn heterostructures. *Physical Review B*, 97:075434, 2018.

[96] S. Lee and *et al.* Charge-to-spin conversion in twisted graphene/wse2 heterostructures. *Physical Review B*, 106:165420, 2022.

[97] L. Benítez and *et al.* Tunable room-temperature spin galvanic and spin hall effects in van der waals heterostructures. *Nature Materials*, 19:170–175, 2020.

[98] S. Ghiasi and *et al.* Charge-to-spin conversion by the rashba–edelstein effect in two-dimensional van der waals heterostructures up to room temperature. *Nano Letters*, 19:5959–5966, 2019.

[99] D. Safeer and *et al.* Room-temperature spin hall effect in graphene/mos2 van der waals heterostructures. *Nano Letters*, 19:10741082, 2019.

[100] J. Garcia and *et al.* Spin hall effect and weak antilocalization in graphene/transition metal dichalcogenide heterostructures. *Nano Letters*, 17:5078–5083, 2017.

[101] L. Benítez and *et al.* Strongly anisotropic spin relaxation in graphene–transition metal dichalcogenide heterostructures at room temperature. *Nature Physics*, 14:303–308, 2018.

[102] L. Benítez and *et al.* Investigating the spin-orbit interaction in van der waals heterostructures by means of the spin relaxation anisotropy. *APL Materials*, 7:120701, 2019.

[103] Y. Li and *et al.* Twist-angle dependence of the proximity spin-orbit coupling in graphene on transition-metal dichalcogenides. *Physical Review B*, 99:075438, 2019.

[104] A. David and *et al.* Induced spin-orbit coupling in twisted graphene–transition metal dichalcogenide heterobilayers: twistronics meets spintronics. *Physical Review B*, 100:085412, 2019.

[105] T. Ghiasi and *et al.* Large proximity-induced spin lifetime anisotropy in transition-metal dichalcogenide/graphene heterostructures. *Nano Letters*, 17:7528–7532, 2017.

[106] P. Tiwari, S. Srivastav, and *et al.* Observation of time-reversal invariant helical edge-modes in bilayer graphene/wse2 heterostructure. *ACS Nano*, 15:916922, 2020.

[107] H. Zhou, L. Holleis, Y. Saito, L. Cohen, W. Huynh, and *et al.* Isospin magnetism and spin-polarizedsuperconductivity in bernal bilayer graphene. *Science*, 375:774–778, 2022.

[108] K. Zollner and *et al.* Scattering-induced and highly tunable by gate damping-like spin-orbit torque in graphene doubly proximitized by two-dimensional magnet cr2ge2te6 and monolayer wse2. *Physical Review B*, 2:043057, 2020.

[109] P. Högl and *et al.* Quantum anomalous hall effects in graphene from proximity-induced uniform and staggered spin-orbit and exchange coupling. *Physical Review Letters*, 124:136403, 2020.

[110] P. U. Asshoff and *et al.* Magnetoresistance of vertical co-graphene-nife junctions controlled by charge transfer and proximity-induced spin splitting in graphene. *2D Materials*, 4:031004, 2017.

[111] S. Pandey and *et al.* Room-temperature anomalous hall effect in graphene in interfacial magnetic proximity to euo grown by topotactic reduction. *Physical Review B*, 108:144423, 2023.

[112] Z. Qiao, S. A. Yang, W. Feng, W.-K. Tse, J. Ding, Y. Yao, J. Wang, and Q. Niu. Quantum anomalous Hall effect in graphene from Rashba and exchange effects. *Physical Review B*, 82:161414, 2010.

[113] Z. Qiao, W. Ren, H. Chen, L. Bellaiche, Z. Zhang, A. H. MacDonald, and Q. Niu. Quantum anomalous Hall effect in graphene proximity coupled to an antiferromagnetic insulator. *Physical Review Letters*, 112:116404, 2014.

[114] J. Zhang, B. Zhao, Y. Yao, and Z. Yang. Robust quantum anomalous Hall effect in graphene-based van der Waals heterostructures. *Physical Review B*, 92:165418, 2015.

[115] P. Hög, T. Frank, K. Zollner, D. Kochan, M. Gmitra, and J. Fabian. Quantum anomalous Hall effects in graphene from proximity-induced uniform and staggered spin-orbit and exchange coupling. *Physical Review B*, 124:136403, 2020.

[116] H. Zhang, Y. Ning, W. Yang, and *et al.* Possible realization of the high-temperature and multichannel quantum anomalous hall effect in graphene/crbr3 heterostructures under pressure. *Physical Chemistry Chemical Physics*, 21:17087–17095, 2019.

[117] J. Zhang, B. Zhao, T. Zhou, Y. Xue, C. Ma, and Z. Yang. Strong magnetization and Chern insulators in compressed graphene/CrI_3 van der Waals heterostructures. *Physical Review B*, 97:085401, 2018.

[118] Z. Xu. Fundamental properties of graphene. *Graphene Fabrication, Characterizations, Properties and Applications*, pages 73–102, 2018.

[119] A. H. Castro Neto and *et al.* The electronic properties of graphene. *Reivew of modern physics*, 81:109, 2009.

[120] N. Bultinck, E. Khalaf, S. Liu, S. Chatterjee, A. Vishwanath, and M. P. Zaletel. Ground state and hidden symmetry of magic-angle graphene at even integer filling. *Physical Review X*, 10:031034, 2020.

[121] J. M. Park, Y. Cao, K. Watanabe, T. Taniguchi, and P. Jarillo-Herrero. Flavour hund's coupling, chern gaps and charge diffusivity in moiré graphene. *Nature*, 592:43–48, 2021.

[122] A. Kerelsky, L. J. McGilly, D. M. Kennes, L. Xian, M. Yankowitz, S. Chen, K. Watanabe, T. Taniguchi, J. Hone, C. Dean, A. Rubio, and A. N. Pasupathy. Maximized electron interactions at the magic angle in twisted bilayer graphene. *Nature*, 572:95–100, 2019.

[123] Y. Xie, B. Lian, B. Jäck, X. Liu, C.-L. Chiu, K. Watanabe, T. Taniguchi, B. A. Bernevig, and A. Yazdani. Spectroscopic signatures of many-body correlations in magic-angle twisted bilayer graphene. *Nature*, 572:101–105, 2019.

[124] U. Zondiner, A. Rozen, D. Rodan-Legrain, Y. Cao, R. Queiroz, T. Taniguchi, K. Watanabe, Y. Oreg, F. von Oppen, A. Stern, E. Berg, P. Jarillo-Herrero, and S. Ilani. Cascade of phase transitions and dirac revivals in magic-angle graphene. *Nature*, 582:203–208, 2020.

[125] J. Liu and X. Dai. Theories for the correlated insulating states and quantum anomalous hall effect phenomena in twisted bilayer graphene. *Physical Review B*, 103:035427, 2021.

[126] H. C. Po, L. Zou, A. Vishwanath, and T. Senthil. Origin of mott insulating behavior and superconductivity in twisted bilayer graphene. *Physical Review X*, 8:031089, 2018.

[127] B. Lian, Z.-D. Song, N. Regnault, D. K. Efetov, A. Yazdani, and B. A. Bernevig. Twisted bilayer graphene. iv. exact insulator ground states and phase diagram. *Physical Review B*, 103:205414, 2021.

[128] Y. Saito and *et al.* Hofstadter subband ferromagnetism and symmetry-broken chern insulators in twisted bilayer graphene. *Nature physics*, 17:478–481, 2021.

[129] S. Wu and *et al.* Chern insulators, van hove singularities and topological flat bands in magic-angle twisted bilayer graphene. *Nature Materials*, 20:488–494, 2021.

[130] K. Nuckolls and *et al.* Strongly correlated chern insulators in magic-angle twisted bilayer graphene. *Nature*, 588:610–615, 2020.

[131] Y. Xie and *et al.* Fractional chern insulators in magic-angle twisted bilayer graphene. *Nature*, 600:439–443, 2021.

[132] K. P. Nuckolls, M. Oh, D. Wong, B. Lian, K. Watanabe, T. Taniguchi, B. A. Bernevig, and Yazdani A. Strongly correlated chern insulators in magic-angle twisted bilayer graphene. *Nature*, 588:610–615,]2020.

[133] N. D. Mermin and H. Wagner. Absence of ferromagnetism or antiferromagnetism in one- or two-dimensional isotropic heisenberg models. *Physical Review Letters*, 17:1133, 1966.

[134] B. I. Halperin. On the hohenberg–mermin–wagner theorem and its limitations. *Journal of Statistical Physics*, 175:521–529, 2019.

[135] X. Wang and *et al.* Raman spectroscopy of atomically thin two-dimensional magnetic iron phosphorus trisulfide (feps3) crystals. *2D Materials*, 3:031009, 2016.

[136] B. Huang, G. Clark, E. Navrro-Moratalla, D. R. Klein, R. Cheng, K. L. Seyler, D. Zhong, E. Schmidgall, M. A. McGuire, D. H. Cobden, W. Yao, D. Xiao, P. Jarillo-Herrero, and X. Xu. Layer-dependent ferromagnetism in a van der Waals crystal down to the monolayer limit. *Nature*, 546:270–273, 2017.

[137] J. Cenker and *et al.* Reversible strain-induced magnetic phase transition in a van der waals magnet. *Nature Nanotechnology*, 17:256–261, 2022.

[138] T. Song, X. Cai, M. Tu, X. Zhang, B. Huang, and *et al.* Giant tunneling magnetoresistance in spin-filter van der waals heterostructures. *Science*, 360:1214–1218, 2018.

[139] T. Song, M. W.-Y. Tu, C. Carnahan, X. Cai, T. Taniguchi, K. Watanabe, M. A. McGuire, D. H. Cobden, D. Xiao, W. Yao, and X. Xu. Voltage control of a van der Waals spin-filter magnetic tunnel junction. *Nano Letters*, 19:915–920, 2019.

[140] H. Li, Z. Ying, B. Lyu, A. Deng, L. Wang, T. Taniguchi, K. Watanabe, and Z. Shi. Electrode-free anodic oxidation nanolithography of low-dimensional materials. *Nano Letters*, 18:8011–8015, 2018.

[141] P. Streda. Quantised hall effect in a two-dimensional periodic potential. *Journal of Physics C: Solid State Physics*, 15:L1299, 1982.

[142] F. Lafont, R. Ribeiro-Palau, D. Kazazis, A. Michon, O. Couturaud, C. Consejo, T. Chassagne, M. Zielinski, M. Portail, B. Jouault, F. Schopfer, and Poirier W. Quantum hall resistance standards from graphene grown by chemical vapour deposition on silicon carbide. *Nature Communications*, 6:6806, 2015.

[143] J. A. Alexander-Webber, J. Huang, D. K. Maude, T. J. B. Janssen, A. Tzalenchuk, V. Antonov, T. Yager, S. Lara-Avila, R. Yakimova, and R. J. Nicholas. Giant quantum Hall plateaus generated by charge transfer in epitaxial graphene. *Scientific Reports*, 6:30296, 2016.

[144] S. Larentis, J. R. Tolsma, B. Fallahazad, D. C. Dillen, K. Kim, A. H. MacDonald, and E. Tutuc. Band offset and negative compressibility in graphene-mos2 heterostructures. *Nano Letters*, 14:2039–2045, 2014.

[145] A. M. Holmes, S. Pakniyat, S. A. H. Gangaraj, F. Monticone, Weinert M., and G. W. Hanson. Exchange splitting and exchange-induced nonreciprocal photonic behavior of graphene in CrI_3-graphene van der Waals heterostructures. *Physical Review B*, 102:075435, 2020.

[146] M. U. Farooq and J. Hong. Switchable valley splitting by external electric field effect in graphene/CrI_3 heterostructures. *npj 2D Materials and Applications*, 3:33, 2019.

[147] J. Zhang, B. Zhao, T. Zhou, Y. Xue, C. Ma, and Z. Yang. Strong magnetization and Chern insulators in compressed graphene/CrI_3 van der Waals heterostructures. *Physical Review B*, 97:085401, 2018.

[148] H. H. Kim, B. Yang, T. Patel, F. Sfigakis, C. Li, S. Tian, H. Lei, and A. W. Tsen. One million percent tunnel magnetoresistance in a magnetic van der Waals heterostructure. *Nano Letters*, 18:4885–4890, 2018.

[149] Z. Wang, I. Gutiérrez-Lezama, N. Ubrig, M. Kroner, M. Gibertini, T. Taniguchi, K. Watanabe, A. Imamoğlu, E. Giannini, and A. F. Morpurgo. Very large tunneling magnetoresistance in layered magnetic semiconductor CrI_3. *Nature Communications*, 9:2516, 2018.

[150] H. H. Kim, B. Yang, S. Li, S. Jiang, C. Jin, Z. Tao, G. Nichols, F. Sfigakis, S. Zhong, C. Li, S. Tian, D. G. Cory, G.-X. Miao, J. Shan, K. F. Mak, H. Lei, K. Sun, and A. W. Zhao, L.and Tsen. Evolution of interlayer and intralayer magnetism in three atomically thin chromium trihalides. *The Proceedings of the National Academy of Sciences*, 116:11131–11136, 2019.

[151] S. K. Behera, M. Bora, S. S. P. Chowdhury, and P. Deb. Proximity effects in graphene and ferromagnetic $CrBr_3$ van der Waals heterostructures. *Physical Chemistry Chemical Physics*, 21:25788–25796, 2019.

[152] M. A. McGuire, G. Clark, S. KC, W. M. Chance, G. E. Jellison, V. R. Cooper, X. Xu, and B. C. Sales. Magnetic behavior and spin-lattice coupling in cleavable van der waals layered $crcl_3$ crystals. *Physical Review Materials*, 1:014001, 2017.

[153] B. Huang, M. A. McGuire, A. F. May, D. Xiao, P. Jarillo-Herrero, and X. Xu. Emergent phenomena and proximity effects in two-dimensional magnets and heterostructures. *Nature Materials*, 19:1276–1289, 2020.

[154] B. Zhou, J. Balgley, P. Lampen-Kelley, J.-Q. Yan, D. G. Mandrus, and E. A. Henriksen. Evidence for charge transfer and proximate magnetism in graphene–$\alpha RuCl_3$ heterostructures. *Physical Review B*, 100:165426, 2019.

[155] A. Avsar, J. Y. Tan, T. Taychatanapat, J. Balakrishnan, G. K. W. Koon, Y. Yeo, J. Lahiri, A. Carvalho, A. S. Rodin, E. C. T. O'Farrell, G. Eda, A. H. Castro Neto, and B. Özyilmaz. Spin–orbit proximity effect in graphene. *Nature Communications*, 5:4875, 2014.

[156] Z. Wang, D.-K. Ki, H. Chen, H. Berger, A. H. MacDonald, and A. F. Morpurgo. Strong interface-induced spin–orbit interaction in graphene on WS_2. *Nature Communications*, 6:8339, 2015.

[157] Z. Wang, D.-K. Ki, J. Y. Khoo, D. Mauro, H. Berger, Levitov L. S., and A. F. Morpurgo. Origin and magnitude of 'designer' spin-orbit interaction in graphene on semiconducting transition metal dichalcogenides. *Physical Review X*, 6:041020, 2016.

[158] I. Cucchi and *et al.* Microfocus laser-angle-resolved photoemission on encapsulated mono-, bi- and few-layer 1t-wte2. *Nano Letters*, 19:554–560, 2019.

[159] S. Tang and *et al.* Quantum spin hall state in monolayer 1t-wte2. *Nature Physics*, 13:683–687, 2017.

[160] X. Qian and *et al.* Quantum spin hall effect in two-dimensional transition metal dichalcogenides. *Science*, 346:1344–134, 2014.

[161] Y.-H. Song and *et al.* Observation of coulomb gap in the quantum spin hall candidate single-layer 1t-wte2. *Nature Communications*, 9:4071, 2018.

[162] Yu Saito, Jingyuan Ge, Kenji Watanabe, Takashi Taniguchi, and Andrea F. Young. Independent superconductors and correlated insulators in twisted bilayer graphene. *Nature Physics*, 16:926–930, 2020.

[163] C. Shen and *et al.* Dirac spectroscopy of strongly correlated phases in twisted trilayer graphene. *Nature Materials*, 22:316–321, 2023.

[164] Y. Maximenko and *et al.* Nanoscale studies of electric field effects on monolayer 1t-wte2. *npj Quantum Materials*, 7:29, 2022.

[165] Y. Cao, D. Rodan-Legrain, J. M. Park, N. F. Q. Yuan, K. Watanabe, T. Taniguchi, R. M. Fernandes, L. Fu, and P. Jarillo-Herrero. Nematicity and competing orders in superconducting magic-angle graphene. *Science*, 372:264–271, 2021.

[166] Y. H. Kwan, G. Wagner, T. Soejima, M. P. Zaletel, S. H. Simon, S. A. Parameswaran, and N. Bultinck. Kekulé spiral order at all nonzero integer fillings in twisted bilayer graphene. *Physical Review X*, 11:041063, 2021.

[167] G. Wagner, Y. H. Kwan, N. Bultinck, S. H. Simon, and S. A. Parameswaran. Global phase diagram of the normal state of twisted bilayer graphene. *Physical Review Letters*, 128:156401, 2022.

[168] D. Wong, K. P. Nuckolls, M. Oh, B. Lian, Y. Xie, S. Jeon, K. Watanabe, T. Taniguchi, B. A. Bernevig, and A. Yazdani. Cascade of electronic transitions in magic-angle twisted bilayer graphene. *Nature*, 582:198–202, 2020.

[169] H. Polshyn, J. Zhu, M. A. Kumar, Y. Zhang, F. Yang, C. L. Tschirhart, M. Serlin, K. Watanabe, T. Taniguchi, A. H. MacDonald, and A. F. Young. Electrical switching of magnetic order in an orbital chern insulator. *Nature*, 588:66–70, 2020.

[170] S. Grover, M. Bocarsly, A. Uri, P. Stepanov, G. Di Battista, I. Roy, J. Xiao, A. Y. Meltzer, Y. Myasoedov, K. Pareek, K. Watanabe, T. Taniguchi, B. Yan, A. Stern,

E. Berg, D. K. Efetov, and E. Zeldov. Imaging chern mosaic and berry-curvature magnetism in magic-angle graphene. *arXiv:2201.06901*, 2022.

[171] J. Zhu, J.-J. Su, and A. H. MacDonald. Voltage-controlled magnetic reversal in orbital chern insulators. *Physical Review Letters*, 125:227702, 2020.

[172] C. L. Tschirhart, M. Serlin, H. Polshyn, A. Shragai, Z. Xia, J. Zhu, Y. Zhang, K. Watanabe, T. Taniguchi, M. E. Huber, and A. F. Young. Imaging orbital ferromagnetism in a moiré chern insulator. *Science*, 372:1323–1327, 2021.

[173] A. L. Sharpe, E. J. Fox, A. W. Barnard, J. Finney, K. Watanabe, T. Taniguchi, M. A. Kastner, and D. Goldhaber-Gordon. Evidence of orbital ferromagnetism in twisted bilayer graphene aligned to hexagonal boron nitride. *Nano Letters*, 21:4299–4303, 2021.

[174] J. Shi, J. Zhu, and A. H. MacDonald. Moiré commensurability and the quantum anomalous hall effect in twisted bilayer graphene on hexagonal boron nitride. *Physical Review B*, 103:075122, 2021.

[175] D. Mao and T. Senthil. Quasiperiodicity, band topology, and moiré graphene. *Physical Review B*, 103:115110, 2021.

[176] E. Khalaf, P. Ledwith, and A. Vishwanath. Symmetry constraints on superconductivity in twisted bilayer graphene: Fractional vortices, $4e$ condensates or non-unitary pairing. *arXiv:2012.05915*, 2020.

[177] J.-X. Lin, Y.-H. Zhang, E. Morissette, Z. Wang, S. Liu, D. Rhodes, K. Watanabe, T. Taniguchi, J. Hone, and J. I. A. Li. Spin-orbit–driven ferromagnetism at half moiré filling in magic-angle twisted bilayer graphene. *Science*, 375:437–441, 2022.

[178] J. Diez-Merida, A. Diez-Carlon, S. Y. Yang, Y.-M. Xie, X.-J. Gao, K. Watanabe, T. Taniguchi, X. Lu, K. T. Law, and D. K. Efetov. Magnetic josephson

junctions and superconducting diodes in magic angle twisted bilayer graphene. *arXiv:2110.01067*, 2021.

[179] P. Stepanov, I. Das, X. Lu, A. Fahimniya, K. Watanabe, T. Taniguchi, F. H. L. Koppens, J. Lischner, L. Levitov, and Efetov D. K. Untying the insulating and superconducting orders in magic-angle graphene. *Nature*, 583:375–378, 2020.

[180] E. Codecido, Q. Wang, R. Koester, S. Che, H. Tian, R. Lv, S. Tran, K. Watanabe, F. Taniguchi, T.a nd Zhang, M. Bockrath, and C. N. Lau. Correlated insulating and superconducting states in twisted bilayer graphene below the magic angle. *Science Advances*, 5:eaaw9770, 2019.

[181] P. Stepanov, M. Xie, T. Taniguchi, K. Watanabe, X. Lu, A. H. MacDonald, B. A. Bernevig, and Efetov D. K. Competing zero-field chern insulators in superconducting twisted bilayer graphene. *Physical Review Letters*, 127:197701, 2021.

[182] L. Powalla and *et al.* Berry curvature-induced local spin polarisation in gated graphene/wte2 heterostructures. *Nature Communications*, 13:3152, 2022.